Manifestations of Spin–Orbit Coupling in Molecular Systems

Can Liao

A dissertation
submitted in partial fulfillment of the
requirements for the degree of

Doctor of Philosophy

University of Washington

2025

Reading Committee:
Xiaosong Li, Chair
Anne McCoy
Cody Schelnker

Program Authorized to Offer Degree:
Chemistry

University of Washington

Abstract

Manifestations of Spin–Orbit Coupling in Molecular Systems

Can Liao

Chair of the Supervisory Committee:
Xiaosong Li
Department of Chemistry

Quantum chemistry traditionally focuses on solving the non-relativistic Schrödinger equation to model chemical systems. Although the Schrödinger equation can be quite accurate for systems composed of light atoms, special relativity must be considered in the presence of heavy elements where electrons approach the speed of light or in spin-driven processes. While many-body methods developed for the Schrödinger equation have been adapted for the Dirac equation, solving the latter is more computationally demanding. To mitigate this challenge, approximations have been introduced to reduce the complexity of the Dirac problem. Additionally, Dirac-derived perturbative corrections to the Schrödinger equation have been developed to selectively account for key relativistic effects. This Thesis explores the motivations behind different approximations to the many-body Dirac equation. In particular, the state interaction method for approximating vector relativity is examined within configuration interaction and linear response time-dependent density functional theory. A benchmark study comparing state interaction and fully variational treatments of vector relativity is also presented. Beyond exploring the theoretical foundations and performance of these methods, this Thesis highlights the chemical relevance of relativistic effects. Specifically, it presents the application of relativistic methods to elucidate the UV-vis spectra of Au_{25} nanoparticles. Additionally, it investigates the intersystem crossing mechanism of an organic photosensitizer, underscoring the necessity of special relativity even for light elements.

TABLE OF CONTENTS

LIST OF FIGURES

LIST OF TABLES

ABBREVIATIONS

AO: atomic orbitals

AMEW: auxiliary many electron wave function

AREP: averaged relativistic effective core potential

A-TSQ: aniline thiosquarine

CAS: complete active space

CASCI: complete active space configuration interaction

CASSCF: complete active space self-consistent field

CASSCF-SO: complete active space self-consistent field with state interaction spin–orbit coupling in OpenMolcas

CI: configuration interaction

CIS: configuration interaction - singles

CISD: configuration interaction - singles and doubles

CSF: configuration state function

DAS: distributed active space

DASCI: distributed active space configuration interaction

DASSCF: distributed active space self-consistent field

DBA-TSQ: 2-(4-(Dibutylamino)phenyl)-4-(4-(dibutyliminio)cyclohexa-2,5 dien-1-ylidene)-3-thioxocyclo-but-1-enethiolate (dibutylaniline thiosquarine)

DFT: density functional theory

DKHn: nth-order Douglas–Kroll–Hess

ECP: effective core potential

FLOP: floating-point operation

HOMO: highest occupied molecular orbital

ISC: intersystem crossing

LCAO: linear combination of atomic orbitals

LMCO: ligand metal charge transfer

LUMO: lowest unoccupied molecular orbital

MCSCF: multi-configurational self-consistent field

MECP: minimal energy crossing point

MO: molecular orbitals

RAS: restricted active space

RASCI: restricted active space configuration interaction

RASSCF: restricted active space self-consistent field

SCF: self-consistent field

SNSO: screened-nuclear spin–orbit

SOC: spin–orbit coupling

SML: staple motif layer

TA: transient absorption

TDA: linear response time-dependent density functional theory under the Tamm-Dancoff approximation

TDDFT: linear response time-dependent density functional theory

2c-TDDFT: two-component linear response time-dependent density functional theory

TDDFT-SO: linear response time-dependent density functional theory with state interaction spin–orbit coupliong

X2C: exact two-component

srX2C: scalar-relativistic exact two-component

ACKNOWLEDGMENTS TO PREVIOUSLY PUBLISHED WORK

Parts of Sections 3.1.1 and 3.1.2 are adapted from published work with permission from Can Liao, Chad E. Hoyer, Rahoul Banerjee Ghosh, Andrew J. Jenkins, Stefan Knecht, Michael J. Frisch, and Xiaosong Li. "Comparison of Variational and Perturbative Spin–Orbit Coupling within Two-Component CASSCF". The Journal of Physical Chemistry A. 2024 128 (12), 2498-2506. DOI: 10.1021/acs.jpca.3c08031 Copyright 2024 American Chemical Society.

Parts of Section 3.1.3 is adapted from published work with permission from Chad E. Hoyer, Can Liao, Kirill D. Shumilov, Tianyuan Zhang, and Xiaosong Li. "State Interaction for Relativistic Four-Component Methods: Choose the Right Zeroth-Order Hamiltonian for Late-Row Elements". Journal of Chemical Theory and Computation. 2024 20 (18), 7969-7978. DOI: 10.1021/acs.jctc.4c00797. Copyright 2024 American Chemical Society.

Parts of Sections 3.2 and 4.1.4 are adapted from published work with permission from Can Liao, Joseph M Kasper, Andrew J Jenkins, Ping Yang, Enrique R Batista, Michael J Frisch, Xiaosong Li. "State Interaction Linear Response Time-Dependent Density Functional Theory with Perturbative Spin–Orbit Coupling: Benchmark and Perspectives". JACS Au. 2023 3 (2). 358-367. DOI: 10.1021/jacsau.2c00659. Copyright 2023 American Chemical Society.

Parts of Section 4.1 is adapted from published work with permission from Can Liao, Manzhou Zhu, De-en Jiang, Xiaosong Li. ''Manifestation of the Interplay between Spin–Orbit and Jahn-–Teller Effects in Au_{25} Superatom UV-Vis Fingerprint Spectra". Chemical Science. 2023 14 (18). 4666-4671. DOI: 10.1039/d3sc00944k. Copyright 2023 Royal Society of Chemistry.

Parts of Section 4.2 is adaption from recentlky accepted work with permission from Can Liao, Cecily Rosenbaum, Alexis Glaudin, Maxwell Taub, Rahoul Banerjee Ghosh, Sarah Pristash, Cody Schlenker, and Xiaosong Li.

Dedicated to food stamps,

and government programs that promote the general welfare of the Nation.

ACKNOWLEDGMENTS

My success is not mine alone, but the result of the collective efforts of those around me. A person is shaped by their environment, and I am incredibly fortunate to have been surrounded by people and circumstances that have contributed to my achievements. First and foremost, I am grateful to the stochastic forces of the Universe for placing me on a path that has led to this moment.

I owe an immeasurable debt of gratitude to my parents, who made the courageous decision to uproot their lives and move to an unfamiliar country. For 25 years, they have worked tirelessly on near-minimum wages without taking a single day of vacation.

I am grateful that my parents chose to immigrate to the United States, a nation that aspires to a society where all individuals are equal under the law and have access to opportunities regardless of race, religion, country of origin, sexual orientation, or gender. I would not be where I am today without the support this country provided in times of need. Medicaid gave my parents peace of mind to work without fear of the next medical emergency. SNAP and the NSLP allowed me to dream bigger instead of worrying about my next meal. Federal student aid made it possible for me to turn those dreams into reality.

As a gesture of gratitude, I joined the US Army. However, even during my service, this country continues to give. I am thankful to the Army for shaping my transition into adulthood, teaching me the values of hard work and discipline, and providing me with the maturity and interpersonal skills needed to be an effective teammate in my research group and succeed in a PhD program.

I am deeply thankful to my research group for their time, patience, and guidance in helping me develop as a scientist. I began with little knowledge of electronic structure theory or computer programming, but through the mentorship and supportive environment of the group, I was able to make a contribution to the field and complete my PhD program. My PhD advisor, Xiaosong Li, deserves special thanks for recognizing my potential and giving me an opportunity despite my weak scientific background, as well as for providing the funding and resources for my success.

Lastly, I thank my wife, Shirlo Selvam, for supporting me through the past five years of graduate school. Without her being the primary breadwinner while taking on most of the housework, I would not have been able to focus on my PhD and grow into the scientist I am today. I am deeply grateful for her accompanying me on this journey and sharing the burden along the way. As this chapter of our lives comes to a close, together we will reap the fruits that await from the seeds we've sown over the past five years.

Chapter 1

OVERVIEW OF ELECTRONIC STRUCTURE METHODS

> *"The underlying physical laws necessary for the mathematical theory of a large part of physics and the whole of chemistry are thus completely known, and the difficulty is only that the exact application of these laws leads to equations much too complicated to be soluble. It therefore becomes desirable that approximate practical methods of applying quantum mechanics should be developed, which can lead to an explanation of the main features of complex atomic systems without too much computation."*
>
> – Paul Dirac

When asked about my profession, I say that I am a theoretical chemist specializing in quantum chemistry. The person asking typically gives one of two responses. One response is eye-widening fascination, envisioning a world of magician-scientists who develop multiverse teleportation devices and vibranium-powered super-armor that can deflect a nuclear warhead. The other response is an eye roll, seeing me as lost in the ivory tower, preoccupied with trivial and esoteric pursuits disconnected with the real world. The latter reaction usually comes from my family and experimentalists. In reality, quantum chemistry is simply applying quantum mechanics to solve chemical problems.

The development of quantum mechanics was driven by the pursuit of understanding spectroscopic phenomena and systems of atomic scale or smaller. It is only natural to apply quantum mechanics to chemistry as all chemical systems are essentially interacting electrons and nuclei. The governing equations for these systems have been known exactly for nearly a century. However, these equations are too complex to be solved exactly in an efficient and timely manner. Therefore, it is essential to seek approximations to extract meaning from these equations.

Quantum mechanics hinges on the Schrödinger equation

$$\hat{H}\Psi(t) = i\hbar\frac{\partial}{\partial t}\Psi(t) \tag{1.1}$$

where $\Psi(t)$ is the wave function of the system at time t and $\hat{H}$ is the Hamiltonian which describes the energy of the system. In its time-independent form, the Schrödinger equation is written as

$$\hat{H}\Psi = E\Psi \tag{1.2}$$

where E is the energy of the system at a state described by Ψ. There are infinite but countable possibilities of states Ψ for a Hamiltonian of a bound system. The ground state is described by the lowest energy wave function whereas other higher energy states are called excited states. The Hamiltonian for a general molecule is

$$\hat{H} = -\sum_{A}\frac{\hbar^2}{2m_A}\nabla^2_{\mathbf{R}_A} - \sum_{i}\frac{\hbar^2}{2m_e}\nabla^2_{\mathbf{r}_i} - \sum_{iA}\frac{Z_A}{4\pi\epsilon_0 r_{iA}} + \sum_{i<j}\frac{1}{4\pi\epsilon_0 r_{ij}} + \sum_{A<B}\frac{Z_A Z_B}{4\pi\epsilon_0 R_{AB}} \tag{1.3}$$

where m_A is the mass of nucleus A, m_e is the mass of the electron, Z_A is the charge of nucleus A, $\mathbf{R}_A$ is the position of nucleus A, $\mathbf{r}_{ij}$ is the distance between electrons i and j, r_{iA} is the distance between the electron i and nucleus A, and r_{AB} is the distance between atoms A and B. From here on, this Thesis will use atomic units ($\hbar = m_e = 4\pi\epsilon_0 = 1$). Because the nuclear mass is much larger than the electron mass, it is typically acceptable to invoke the Born-Oppenheimer approximation and solve the Hamiltonian in terms of electronic coordinates while fixing nuclear positions. This Hamiltonian is called the electronic Hamiltonian $\hat{H}_e$.

$$\hat{H}_e(\mathbf{r};\mathbf{R}) = -\sum_{i}\frac{1}{2}\nabla^2_{\mathbf{r}_i} - \sum_{iA}\frac{Z_A}{r_{iA}} + \sum_{i<j}\frac{1}{r_{ij}} + \sum_{A<B}\frac{Z_A Z_B}{R_{AB}} \tag{1.4}$$

The electronic problem can be solved at various nuclear positions to construct a potential energy surface $\hat{V}_N$ that can be used to solve the remaining nuclear portion of the Schrödinger equation.

$$\hat{H}_N(\mathbf{R}) = -\sum_A \frac{\hbar^2}{2m_A}\nabla^2_{\mathbf{R}_A} + \hat{V}_N(\mathbf{R}) \tag{1.5}$$

This Thesis mainly focuses on solving the electronic Schrödinger equation. The subscript indicating the electronic Hamiltonian is dropped for brevity. Because the nuclear-nuclear interaction term is a constant in the electronic Hamiltonian, it is omitted when solving the electronic Schrödinger equation as it only provides a constant shift to the electronic energies.

The equations governing a general molecule are exactly known. Even with the Born-Oppenheimer approximation, the Schrödinger equation does not have known analytical solutions for systems with more than one electron. Solving the Schrödinger equation on a numerical grid also becomes unfeasible as the dimensionality grows exponentially with the number of electrons. Any practical application of quantum chemistry relies on approximations. Over the years, a wealth of techniques have been developed to approximately solve the electronic Schrödinger equation. Each technique possesses its advantages and disadvantages and is chosen based on the characteristics of the system, desired accuracy, and properties of interest.

Most ground state techniques utilize the variational principle, which states that minimizing the energy expectation value of some function with respect to its parameters results in the closest approximation to the ground state wave function within that functional form. This function is also known as the trial wave function. Application of the variational principle manifests in a multitude of forms. In spectral methods, where the Hamiltonian is represented by a matrix within a finite basis, the trial wave function is a linear combination of basis functions where the linear combination coefficients are the variational parameters. Minimizing the energy with respect to these coefficients through the Lagrange undetermined multiplier method culminates in a generalized eigenvalue problem

$$\mathbf{HC} = \mathbf{SCE} \tag{1.6}$$

where **H** is the matrix representation of the Hamiltonian, **S** is the basis overlap matrix, **C** is the matrix of eigenvectors which represent solutions to the Schrödinger equation, and **E** is the diagonal matrix of eigenvalues corresponding to the energy of the states represented in **C**.

1.1 Hartree-Fock Approximation

The Hartree-Fock approximation reduces the many-body problem into an effective one-body problem by approximating the molecule as a system of non-interacting electrons where each electron only experiences an averaged potential from all other electrons. This approximate Hamiltonian is called the Fock operator

$$\hat{F} = \sum_i \hat{f}_i = -\sum_i \frac{1}{2}\nabla^2_{\mathbf{r}_i} - \sum_{iA} \frac{Z_A}{r_{iA}} + \sum_i \bar{V}_i = \sum_i \hat{h}_i + \sum_i \bar{V}_i \tag{1.7}$$

where $\bar{V}_i$ is the Hartree-Fock potential experienced by electron i. The operator $\hat{h}_i$ is called the core Hamiltonian, which encompasses the kinetic energy operator and all interactions apart from electron-electron interactions. The Fock operator does not have coupling terms between different electrons, allowing the Fock operator to be separated into a sum of one-electron Fock operators. The resulting one-electron Schrödinger equations, called one-electron Fock equations, can be solved independently, yielding one-electron wave functions called an orbital $\phi(\mathbf{x}_i)$ with a corresponding orbital energy ϵ_i. Though spin is not a parameter of the Hamiltonian, spin must be included *a posteriori* to satisfy the fermionic nature of the electron. Thus two spin orbitals $\{\chi^\alpha, \chi^\beta\}$ arise for each orbital solution to the one-electron Fock equation.

$$\{\phi(\mathbf{x}_i)\} \rightarrow \{\phi(\mathbf{x}_i)\alpha(i), \phi(\mathbf{x}_i)\beta(i)\} = \{\chi^\alpha(\mathbf{x}_i), \chi^\beta(\mathbf{x}_i)\} \tag{1.8}$$

Since each electron is indistinguishable, it suffices to only solve one of the one-electron Fock equations. The solution to the many-body Fock equation is an anti-symmetrized product of spin orbitals called a Slater determinant,

$$|\chi_1 \dots \chi_N\rangle = \begin{vmatrix} \chi_1(\mathbf{x}_1) & \dots & \chi_N(\mathbf{x}_1) \\ \vdots & & \vdots \\ \chi_1(\mathbf{x}_N) & \dots & \chi_N(\mathbf{x}_N) \end{vmatrix} \tag{1.9}$$

where N is the number of electrons. The orbitals included in the Slater determinant are said to be occupied. The Pauli exclusion principle only allows one electron to occupy each spin orbital. The ground state Slater determinant is constructed by occupying the N-lowest energy spin orbitals. The Slater determinant is an exact solution to the Fock Hamiltonian. Because the Fock Hamiltonian does not actually describe the system of interest and only used to obtain an approximate wave function, the Slater determinant expectation value of the actual Hamiltonian is defined as the Hartree-Fock ground state energy.

The one-electron Fock equation is solved using the spectral method within a basis representation.

$$\mathbf{FC} = \mathbf{SCE} \tag{1.10}$$

A popular choice of basis functions is a set of real-valued atom-centered functions that are products between a Gaussian and a solid harmonic. The basis functions are often referred to as the atomic orbitals (AOs). This basis is not necessarily orthonormal, resulting in a non-unity overlap.

$$S_{\mu\nu} = \langle \mu | \nu \rangle \tag{1.11}$$

Eigenstates of the Fock operator are called molecular orbitals (MOs) and are expressed as a linear combination of basis functions with the coefficients given by $\mathbf{C}$.

$$|p\rangle = \sum_{\mu} C_{p\mu} |\mu\rangle \tag{1.12}$$

The Fock matrix elements can be written as

$$F_{\mu\nu} = \langle\mu|\hat{h}|\nu\rangle + \sum_{\lambda\kappa} P_{\lambda\kappa}[(\mu\nu|\lambda\kappa) - (\mu\lambda|\kappa\nu)] \tag{1.13}$$

where $P_{\mu\nu}$ is the density matrix.

$$P_{\lambda\kappa} = \sum_{i=1}^{N} C_{i\lambda}C_{i\kappa} \tag{1.14}$$

Since the Fock matrix and MO coefficients are mutually dependent, Equation (1.10) is not a simple generalized eigenvalue problem. Instead, the Hartree-Fock problem is a non-linear eigenvalue problem in which the coefficients must be solved iteratively, with the Fock matrix updated at each iteration using the new coefficients, until self-consistency is achieved.[4,5]

The Hartree-Fock approximation seldomly models molecules well. Hartree-Fock theory predicts unphysical degeneracy breaking of Kramers pairs since the majority spin experiences greater stabilization from exchange. This can be avoided with a Kramers-restricted formalism but this approximation is still far from adequate for describing most open-shell systems. The energy missing from the inadequate treatment of electron correlation by the Hartree–Fock approximation is called the correlation energy.[4,5] Electron correlation can roughly be categorized as dynamic or static. Dynamic correlation arises from the dynamic interaction between electrons through the Coulomb interaction and the Pauli exclusion principle. Static correlation arises from deficiencies in the wave function *ansatz*. The Slater determinant *ansatz* is unable to treat mixing between different configurations arising from degenerate ground states and the presence of near-degenerate excited states. Such systems are said to be multi-reference, as opposed to single-reference. Both the missing dynamic and static correlation can be remedied by moving to an *ansatz* where the wave function is a linear combination of Slater determinants. If static correlation is not an issue, dynamic correlation can be treated by replacing some Hartree-Fock exchange with an empirically parameterized exchange-correlation functional V_{xc}. The resulting method is called Kohn-Sham density functional theory (DFT).[6] The Hartree-Fock approximation and Kohn-Sham DFT have very different theoretical underpinnings, but are practically more-or-less the same. Both methods reduce the many-body electronic Schrödinger equation to a one-body non-linear eigenvalue problem with a Slater determinant wave function *ansatz*, which is why both methods are referred to as self-consistent field (SCF) methods. Equation (1.13) can be rewritten to encompass both methods

$$F_{\mu\nu} = \langle \mu | \hat{h} | \nu \rangle + P_{\lambda\kappa}[(\mu\nu|\lambda\kappa) - \frac{1}{2}(1-x)(\mu\lambda|\kappa\nu)] + x\langle \mu | V_{xc} | \nu \rangle \tag{1.15}$$

where $x = 1$ if V_{xc} is a pure functional, $x \in (0, 1)$ if V_{xc} is a hybrid functional, or $x = 0$ for the Hartree-Fock approximation. Further discussion is required to fully encompass the complexities of DFT. However, the scope of the Thesis only demands an introduction to Kohn-Sham DFT and the exchange-correlation functional. Further discussions of DFT can be found in Koch and Holthausen.[6]

Both Hartree-Fock and Kohn-Sham DFT poorly captures excited states. In both methods, excited states are Slater determinants representing configurations other than the ground state configuration. Because the Hartree-Fock and Kohn-Sham potentials are constructed with respect to the ground state configuration, electrons in any other configuration still experience the same ground state-derived potential. This is problematic because each configuration manifests a different Hartree-Fock/Kohn-Sham potential.[4]

Despite these shortcomings, both methods serve as the gateway to better approximations to the electronic Schrödinger equation. As previously mentioned, electron correlation can be captured by taking linear combinations of Slater determinants. This simply arrives from seeking a spectral solution of the many-body Schrödinger equation in a Slater determinant basis.

1.2 Second Quantization

Second quantization is a convenient language to express many-body quantum mechanics. In this language, Slater determinants are mapped onto a Fock state, a vector of occupation numbers ordered by the orbital indexing,

$$|I\rangle = |n_1 \dots n_p \dots n_N\rangle \tag{1.16}$$

where n_p is the occupation number for orbital p. Slater determinants and their Fock states are written interchangeably as $|I\rangle$ with their interpretation inferred from context. The inner product between Fock states are defined as

$$\langle I|J\rangle = \prod_p \delta_{n_p^I n_p^J} \tag{1.17}$$

where n_p^I is the occupation number for orbital p in Slater determinant $|I\rangle$, assuming that the Slater determinants share the same underlying orbitals. The two cornerstones of second quantization are the creation $a_n^\dagger$ and annihilation a_n operators.

$$a_p^\dagger|n_1 \dots n_p \dots n_N\rangle = (-1)^{P_p}|n_1 \dots n_p + 1 \dots n_N\rangle\delta_{n_p 0} \tag{1.18}$$

$$a_p|n_1 \dots n_p \dots n_N\rangle = (-1)^{P_p}|n_1 \dots n_p - 1 \dots n_N\rangle\delta_{n_p 1} \tag{1.19}$$

$$P_p = \sum_{i=1}^{p-1} n_i \tag{1.20}$$

Creation and annihilation operators of the same orbital are adjoint to each other. They observe the anti-commutation relationships

$$a_p^\dagger a_q + a_q a_p^\dagger = \delta_{pq} \tag{1.21}$$

$$a_p^\dagger a_q^\dagger + a_q^\dagger a_p^\dagger = 0 \tag{1.22}$$

$$a_p a_q + a_q a_p = 0 \tag{1.23}$$

The language of second quantization establishes a link between the Slater determinant basis and the orbital basis. A many-body operator $\hat{\Omega}$ written a sum of one-body operators $\hat{O}_i$

acting on electrons i can be expressed as

$$\hat{\Omega}_1 = \sum_i \hat{O}_i = \sum_{pq} O_{pq} a_p^\dagger a_q \tag{1.24}$$

Similarly, a many-body operator $\hat{\Omega}$ written a sum of two-body operators $\hat{O}_{ij}$ acting on electron i and j can be expressed as

$$\hat{\Omega}_2 = \sum_{i<j} \hat{O}_{ij} = \sum_{pqrs} O_{pqrs} a_p^\dagger a_r^\dagger a_s a_q \tag{1.25}$$

A Slater determinant basis matrix element of a many-body operator of the forms shown in Equation (1.24) and Equation (1.25) can be written as

$$\langle I|\hat{\Omega}_1|J\rangle = \sum_{pq} O_{pq} \langle I|a_p^\dagger a_q|J\rangle \tag{1.26}$$

$$\langle I|\hat{\Omega}_2|J\rangle = \sum_{pqrs} O_{pqrs} \langle I|a_p^\dagger a_r^\dagger a_s a_q|J\rangle \tag{1.27}$$

Given that states Ψ_A and Ψ_B are linear combinations of Slater determinants,

$$|\Psi_A\rangle = \sum_I C_{AI}|I\rangle \tag{1.28}$$

$$|\Psi_B\rangle = \sum_J C_{BJ}|J\rangle \tag{1.29}$$

a matrix element between the two states is written as

$$\langle \Psi_A|\hat{\Omega}_1|\Psi_B\rangle = \sum_{pq} O_{pq}\gamma_{pq} = Tr(\mathbf{O}\boldsymbol{\gamma}) \tag{1.30}$$

$$\langle \Psi_A|\hat{\Omega}_2|\Psi_B\rangle = \sum_{pqrs} O_{pqrs}\Gamma_{pqrs} = Tr(\mathbf{O}\boldsymbol{\Gamma}) \tag{1.31}$$

where $\boldsymbol{\gamma}$ and $\boldsymbol{\Gamma}$ are the one-particle and two-particle transition density matrices (TDM) if $A \neq B$ and particle density matrices (PDM) if $A = B$.

$$\gamma_{pq} = \sum_{IJ} \langle I | a_p^\dagger a_q | J \rangle \tag{1.32}$$

$$\gamma_{pqrs} = \sum_{IJ} \langle I | a_p^\dagger a_r^\dagger a_s a_q | J \rangle \tag{1.33}$$

The density matrix that appears in the Hartree-Fock/Kohn-Sham equations, shown in Equation (1.14), is the 1PDM for the ground state Slater determinant in the AO basis.[5,7]

1.3 Configuration Interaction

Solving the many-body electronic Schrödinger equation using the spectral method in a Slater determinant basis is known as configuration interaction (CI). Some approaches to CI prefer to use a basis of configuration state function (CSFs), which are eigenstates of the squared spin angular momentum operator ($\hat{S}^2$) and the azimuthal spin angular momentum operator ($\hat{S}_z$). As long as the Slater determinants are constructed from the same set of orthonormal orbitals with respect to a metric, the Slater determinant, or CSF, basis is orthonormal with respect to a unity metric. The CI problem is a straightforward matrix eigenvalue problem.[4,5]

$$\mathbf{HC} = \mathbf{CE} \tag{1.34}$$

$$|\Psi\rangle = \sum_I C_I |I\rangle \tag{1.35}$$

The core equation of the CI problem may be simple, however, the complexity of CI arises from the exponential scaling of the matrix size. The total number of Slater determinants N_{det} is equal to

$$N_{det} = \binom{N_{orb}}{N_{occ}} \tag{1.36}$$

where N_{orb} is the total number of spin orbitals and N_{occ} is the total number of occupied spin orbitals. Even for a small basis, the full CI problem become unfeasible. For this reason, approximations have been devised to reduce the size of the problem. The truncated CI approximation only considers Slater determinants that arise from a certain number of orbital excitations. For example, CI singles and doubles (CISD) only considers the ground state, singly-excited, and doubly-excited determinants. The Slater determinant basis can also be truncated by defining sets of orbitals called active spaces and limiting excitations between the active spaces. Complete active space CI (CASCI) defines a single active space and only considers Slater determinants generated by excitations within the active space. Restricted active space CI (RASCI) defines three active spaces where only Slater determinants generated by excitations within or between the active spaces while abiding to certain restrictions are considered.[8] Generalizations of RASCI, such as generalized (GASCI)[9] and direct active space CI (DASCI),[10] have been developed to handle an arbitrary number of active spaces, each with its own restrictions.

Full CI is invariant to unitary transformations of the underlying orbitals that form the Slater determinant basis.[4,5] However, it may require a Slater determinant basis generated from a large number different orbital excitations and high-order excitations to span the states of interest, making it difficult to approximate using the previously discussed truncation methods. It is helpful to start with a set of orbitals that are somewhat optimized for the molecule of interest, such as Hartree-Fock or Kohn-Sham orbitals. Truncation of the Slater determinant basis is only feasible if there is a concise subspace spanned by a subset of Slater determinants that encompasses the states of interest. Hartree-Fock and Kohn-Sham orbitals frequently suffice for single-reference systems but not for multi-reference systems. The single-determinant *ansatz* biases the orbitals away from concisely spanning the multi-reference ground state. Capturing multi-reference character in a manageable basis size requires optimizing the orbitals for the states of interest while solving for the CI coefficients. This is usually done in conjunction with truncated CI and/or active space truncations leading to the CASSCF and RASSCF.[5,11,12] CI coefficients and orbitals can be optimized simultaneously or separately, with first-order or second-order optimization techniques. Nevertheless, unitary transformations are applied to the orbitals to follow an energy gradient downward. The energy gradient is

$$\frac{\partial E}{\partial x_{pq}} = 2(F_{pq} - F_{qp}) \tag{1.37}$$

where F_{pq} is the generalized Fock matrix element

$$F_{pq} = \sum_{r} \gamma_{pr} h_{qr} + \sum_{rst} \Gamma_{prst} g_{qrst} \tag{1.38}$$

and x_{pq} are the orbital parameters dictating the unitary transformation $\mathbf{U}$.

$$\mathbf{U} = \exp(\mathbf{x}) \tag{1.39}$$

The mutual dependence between the gradient, orbital parameters, and CI coefficients requires the problem to be solved iteratively. Whether the calculation converges or converges to the global minimum strongly depends on the choice of active space. The active space must contain orbitals that generate Slater determinants that span the states of interest. Unfortunately, active space selection is more of an art relying on chemical intuition, rather than a science. A well-defined active space selection technique is a topic of ongoing research.[13–16]

1.4 Linear Response Time-Dependent Hartree-Fock and DFT

For single-reference systems, CI is typically excessive as dynamic correlation is captured far more efficiently through an exchange-correlation functional. Nevertheless, Kohn–Sham DFT is only reliable for finding the ground state. Excited states can be obtained from truncated CI within an active space using Kohn–Sham orbitals, but this risks potentially double counting electron correlation.[17] Alternatively, excited state information can be obtained from the density response due to an external time-dependent perturbation. The density response can be written in terms of response functions ($\langle\langle\rho; V_{ext}(t)\rangle\rangle$, $\langle\langle\rho; V(\omega_1), V(\omega_2)\rangle\rangle$, $\ldots$)

$$\begin{aligned}\langle\rho(t)\rangle - \langle\Psi_0|\rho|\Psi_0\rangle = &\int_{-\infty}^{\infty} \exp\left(-i\omega_1 t\right)\langle\langle\rho; V_{ext}(t)\rangle\rangle d\omega_1 \\ &+ \frac{1}{2}\int_{-\infty}^{\infty} \exp -i(\omega_1+\omega_2)t\langle\langle\rho; V(\omega_1), V(\omega_2)\rangle\rangle d\omega_1 d\omega_2 + \ldots\end{aligned} \tag{1.40}$$

where ρ is the density operator. Linear response time-dependent DFT (TDDFT) truncates the response expansion at first order. The resonant frequencies of the density correspond to excitation energies and are identified as the poles of the response function in the frequency domain.[18–21] Applying this theory in the context of the Hartree–Fock approximation or Kohn–Sham DFT culminates in a non-Hermitian eigenvalue problem

$$\begin{pmatrix}\mathbf{A} & \mathbf{B} \\ \mathbf{B}^* & \mathbf{A}^*\end{pmatrix}\begin{pmatrix}\mathbf{X} \\ \mathbf{Y}\end{pmatrix} = \begin{pmatrix}\mathbf{1} & \mathbf{0} \\ \mathbf{0} & \mathbf{-1}\end{pmatrix}\begin{pmatrix}\mathbf{X} \\ \mathbf{Y}\end{pmatrix}\begin{pmatrix}\boldsymbol{\omega} & \\ & -\boldsymbol{\omega}\end{pmatrix} \tag{1.41}$$

where **X** are the excitation amplitudes, **Y** are the de-excitation amplitudes, the eigenvalues ω are the excitation energies. The non-Hermitian matrix is the energy Hessian with respect to the orbital parameters

$$A_{iajb} = \delta_{ij}\delta_{ab}(E_a - E_i) + (ia|bj) - x(ij|ab) + (1-x)(ia|V_{XC}|bj) \tag{1.42}$$

$$B_{iajb} = (ia|jb) - x(ib|aj) + (1-x)(ia|V_{XC}|jb) \tag{1.43}$$

where E_p is the orbital energy of MO p and x modulates the amount of exchange-correlation obtained from Hartree-Fock exchange or the exchange-correlation functional. Both **A** and **B** are Hermitian matrices of dimensions $N_{occ}N_{virt} \times N_{occ}N_{virt}$. Pairs of occupied and virtual indices are compounded into a single index. For an entirely real-valued Hessian, which is usually the case for a non-relativistic problem, the eigenvalue problem can be reduced to a halved-dimension form.

$$(\mathbf{A}-\mathbf{B})(\mathbf{A}+\mathbf{B})\mathbf{Z}=\mathbf{Z}\boldsymbol{\omega}^2 \tag{1.44}$$

$$\mathbf{Z}=\mathbf{X}+\mathbf{Y} \tag{1.45}$$

It has been shown that neglecting $\mathbf{B}$ and only solving for $\mathbf{X}$ is an appropriate approximation for many systems.[22,23] This approximation is known as the Tamm–Dancoff approximation (TDA),[21,24]

$$\mathbf{A}\mathbf{X}=\mathbf{X}\boldsymbol{\omega} \tag{1.46}$$

which lowers the computational cost by reducing the amount of terms to construct matrix and allowing the eigenvalue problem to be solved using Hermitian-optimized eigensolvers. This approximation also offers a convenient interpretation of the eigenvectors. The excitation amplitudes given by $X_{ia,I}$ is interpreted as the contribution to excited state I from the orbital excitation $i \to a$. In other words, the TDA solutions map neatly onto a CIS wave function.[21]

$$|I\rangle = \frac{1}{|\mathbf{X}|}\sum_{ia} X_{ia,I}|\Phi_i^a\rangle \tag{1.47}$$

Without TDA, TDDFT yields solutions with eigenvalues $\boldsymbol{\omega}$ and $-\boldsymbol{\omega}$. Solutions corresponding to $\boldsymbol{\omega}$ represent excited states and possess a small $\mathbf{Y}$ relative to $\mathbf{X}$. The complementary set of solutions are ignored as they also represent the same excited states but possess a small $\mathbf{X}$ relative to $\mathbf{Y}$. The presence of non-zero de-excitation amplitudes make the interpretation of the solutions ambiguous. The solutions of the halved-dimensioned TDDFT problem in Equation (1.45) may suggest the mapping

$$\mathbf{X}+\mathbf{Y} \mapsto \frac{1}{|\mathbf{X}+\mathbf{Y}|}\sum_{ia}(X_{ia,I}+Y_{ia,I})|\Phi_i^a\rangle \tag{1.48}$$

but another valid halved-dimension form can be written where the solutions are $\mathbf{X}-\mathbf{Y}$. In this Thesis, $Y_{ia,I}$ is interpreted as representing the same orbital excitation as $X_{ia,I}$, but from the perspective of a hole excitation rather than a particle excitation. This leads to the adoption of the Casida *ansatz* shown in Equation (1.48). These approximate CIS wave functions are called auxiliary many-electron wave functions (AMEW) and have been widely used to compute excited state properties.[25]

Chapter 2

RELATIVISTIC QUANTUM MECHANICS

The speed of light is the universal speed limit. Properties of a moving particle and spacetime itself change to ensure its speed does not exceed the speed of light. Some ways the universe enforces this speed limit include time dilation, space contraction, and increasing mass. In chemical systems, electrons approach the speed of light as nuclear charges increase. The radial speed of a $1s$ electron is[26]

$$\langle v_r \rangle \approx \frac{Zc}{137} \tag{2.1}$$

For perspective, a $1s$ electron in a Hg atom travels at 58% the speed of light, resulting in a 23% increase in mass, a 23% dilation in time, and a 19% contraction of length in the direction of travel in the particle frame of reference. These effects are consequential in chemistry, being responsible for the yellow color of metallic gold, the liquid phase of mercury at standard temperature and pressure, and 83% of the voltage in a lead-acid battery.[26–29] The Schrödinger equation does not recognize this speed limit. Accurate treatment of core electrons and systems containing heavy elements require the adoption of a relativistic quantum wave equation.

The relativistic quantum wave equation governing fermions is the Dirac equation,

$$(c\boldsymbol{\alpha} \cdot \hat{p} + \beta c^2 + V)\Psi = E\Psi \tag{2.2}$$

where $\boldsymbol{\alpha}$ and β are the Dirac matrices.

$$\boldsymbol{\alpha} = \left(\begin{pmatrix} \sigma_x & 0 \\ 0 & \sigma_x \end{pmatrix}, \begin{pmatrix} \sigma_y & 0 \\ 0 & \sigma_y \end{pmatrix}, \begin{pmatrix} \sigma_z & 0 \\ 0 & \sigma_z \end{pmatrix} \right) \tag{2.3}$$

$$\beta = \begin{pmatrix} 1 & 0 \\ 0 & -1 \end{pmatrix} \tag{2.4}$$

The energy and wave function are eigenpairs of the Dirac Hamiltonian. Unlike the Schrödinger equation, the wave functions are four-component spinors

$$\Psi = \begin{pmatrix} \Psi^{L\alpha} \\ \Psi^{L\beta} \\ \Psi^{S\alpha} \\ \Psi^{S\beta} \end{pmatrix} \tag{2.5}$$

where L and S are the "large" and "small" components, and α and β indicate the spin. Notice that spin arises naturally from the Dirac equation and solutions can possess non-collinear spin, that is, exist as a linear combination of α and β spin.[30,31]

It is sometimes convenient to expand Equation (2.2) explicitly in terms of the large and small components.

$$\begin{aligned} \hat{H}\Psi &= E\Psi \\ &= \begin{pmatrix} V & c(\sigma \cdot \hat{p}) \\ c(\sigma \cdot \hat{p}) & V - 2c^2 \end{pmatrix} \begin{pmatrix} \Psi^L \\ \Psi^S \end{pmatrix} = E \begin{pmatrix} \Psi^L \\ \Psi^S \end{pmatrix} \end{aligned} \tag{2.6}$$

Solutions to the Dirac equation for a free electron comes in a set of four four-spinor wave functions. The two large-dominant solutions correspond to electronic solutions. The other two solutions are small-dominant and correspond to positronic solutions. The energies of the electronic and positronic free-particle solutions are positive and negative-valued, respectively.

For this reason, the electronic and positronic solutions are also referred to as positive and negative energy solutions even though both electronic and positronic energies are negative-valued for bound states. Nevertheless, the electronic and positronic solutions are always separated by an energy gap of $2c^2$.[30,31]

At the non-relativistic limit, electrostatic interactions between particles are seen as instantaneous. As particles approach the speed of light, this assumption breaks down. According to quantum electrodynamics, electrostatic interactions are mediated by the exchange of virtual photons, causing a non-trivial delayed interaction when the particles are moving at similar speeds. A genuine relativistic potential must be constructed from these principles. In most chemical systems, electrons hardly approach speeds that experience significant delays. Constructing an electron-electron interaction potential from quantum electrodynamics at the low-delay limit still provides corrections to the Coulomb operator in the form of the Breit operator,

$$V_{ee} = \frac{1}{r_{ij}} - \frac{\boldsymbol{\alpha}_i \cdot \boldsymbol{\alpha}_j}{2r_{ij}} + \frac{(\boldsymbol{\alpha}_i \cdot \mathbf{r}_{ij})(\boldsymbol{\alpha}_j \cdot \mathbf{r}_{ij})}{2r_{ij}^3} = V_C + V_{Gaunt} + V_{Gauge} = V_C + V_B \tag{2.7}$$

where V_{Breit} is comprised of the V_{Gaunt} and V_{Gauge} terms. In the Born-Oppenheimer approximation, nuclei are treated as stationary classical particles, keeping the nuclear-electronic potential simply Coulombic.[30–32]

The electronic structure methods introduced in Chapter 1 have been adapted for the Dirac equation. At its purest form, eigenvalues of the Dirac Hamiltonian is unbounded from below due to the presence of positronic solutions. This pathological property of the Dirac equation is called the Brown–Ravenhall disease. The no-pair approximation avoids variational collapse by neglecting positronic contributions to the many-body wave function. In the language of second quantization, the no-pair approximation restricts creation and annihilation operators to only electronic indices. Albeit a straightforward concept, the no-pair Hamiltonians do not contain “no-pair terms” but is implicitly handled within the context of the algorithm. In Dirac-Hartree-Fock, the no-pair approximation is applied by only summing over electronic orbitals when constructing the density.[31]

Expanding Equation (2.2) into a system of two equations reveals that the L and S components must satisfy the kinetic balance condition to arrive at the correct non-relativistic limit.

$$\lim_{c \to \infty} 2c\Psi^S = (\sigma \cdot \hat{p})\Psi^L \tag{2.8}$$

Large and small component basis functions must satisfy the kinetic balance condition when applying spectral methods to the Dirac equation. There has not been extensive work on developing basis sets that satisfy kinetic balance. This is because it is possible to utilize the same basis set for both the large and small components by shifting the kinetic balance condition to the Hamiltonian while applying an approximate kinetic balance condition to the basis set.

$$|\mu^S\rangle = \frac{(\sigma \cdot \hat{p})}{2c}|\mu^{L'}\rangle \tag{2.9}$$

where $|\mu^{L'}\rangle$ is the pseudo-large basis function. The pseudo-large basis set is the same basis set as the large component, but must be distinguished as it describes the small component. Taking a matrix element between four-spinor basis functions arrives at a Hamiltonian that absorbs the burden of kinetic balance, allowing both large and small components to be expressed by the same basis set.

$$\begin{aligned}
\langle\mu|\hat{H}|\nu\rangle &= \begin{pmatrix}\langle\mu^L| & \langle\mu^S|\end{pmatrix} \begin{pmatrix} V & c(\sigma \cdot \hat{p}) \\ c(\sigma \cdot \hat{p}) & V - 2c^2 \end{pmatrix} \begin{pmatrix} |\nu^L\rangle \\ |\langle\nu^S\rangle \end{pmatrix} \\
&= \begin{pmatrix}\langle\mu^L| & \frac{1}{2c}\langle\mu^{L'}|(\sigma \cdot \hat{p})\end{pmatrix} \begin{pmatrix} V & c(\sigma \cdot \hat{p}) \\ c(\sigma \cdot \hat{p}) & V - 2c^2 \end{pmatrix} \begin{pmatrix} |\nu^L\rangle \\ \frac{1}{2c}(\sigma \cdot \hat{p})|\nu^{L'}\rangle \end{pmatrix} \\
&= \begin{pmatrix}\langle\mu^L| & \langle\mu^{L'}|\end{pmatrix} \begin{pmatrix} V & \hat{T} \\ \hat{T} & \hat{W} - \hat{T} \end{pmatrix} \begin{pmatrix} |\nu^L\rangle \\ |\nu^{L'}\rangle \end{pmatrix}
\end{aligned} \tag{2.10}$$

$$\hat{W} = \frac{1}{4c^2}(\sigma \cdot \hat{p})V(\sigma \cdot \hat{p}) \tag{2.11}$$

This kinetic-balance-infused Hamiltonian is called the modified Dirac Hamiltonian and is typically the Hamiltonian of choice in modern four-component relativistic quantum chemical calculations.[30–34]

$$\hat{H}_{mod} = \begin{pmatrix} V & \hat{T} \\ \hat{T} & \hat{W} - \hat{T} \end{pmatrix} \tag{2.12}$$

The operator $\hat{W}$ can be separated into two terms using the Dirac relation

$$\hat{W} = \hat{H}_{sr} + \hat{H}_{vr} = \frac{1}{4c^2}(\hat{p}V \cdot \hat{p} + i\sigma \cdot \hat{p}V \times \hat{p}) = \frac{1}{4c^2}(\hat{p}V \cdot \hat{p} + \sigma \cdot (\nabla V) \times \hat{p}) \tag{2.13}$$

where $\hat{H}_{sf}$ carries scalar relativistic effects and $\hat{H}_{vr}$ carries vector relativistic effects.[30,31,33,35] Wave functions retain their non-relativistic symmetries when only scalar relativity is introduced. The most prevalent example of scalar relativity is the change in orbital radial distribution. Vector relativistic effects are also known as angular momenta coupling (spin-orbit, spin-spin, orbit-orbit). The type of angular momenta coupling included depends on the interactions included in the potential. The nuclear-electronic potential gives rise to one-electron spin-same-orbit coupling, representing the interaction between the electron spin magnetic moment and the magnetic field generated by its own orbit. The Coulomb term is responsible for two-electron spin-same-orbit coupling, accounting for the correction to the orbital-generated magnetic field from deviations to one-electron orbit due to electron repulsion. The Gaunt term gives rise to two-electron spin-other-orbit coupling, representing the interaction between the electron spin magnetic moment and the magnetic field generated by another electron, as well as spin-spin coupling and some contribution to spin-same-orbit coupling. The Gauge term is responsible for orbit-orbit coupling.

For atomic systems under spin–orbit coupling, the angular momentum of N-electron wave functions cannot be described by N-electron spin and orbital angular momentum quantum numbers separately. Instead, N-electron angular momentum must be described by the N-electron total angular momentum quantum number. Molecules under spin–orbit coupling must incorporate $SU(2)$ symmetry into the symmetry group, leading to what is known as double group symmetry. Consequently, degenerate manifolds based on spin and spatial symmetry is broken into degenerate manifolds based on total angular momentum or double group irreducible representations.[30–32] This is discussed in greater detail in Section 2.3.

2.1 Decoupling Transformations

The Foldy-Wouthuysen transformation is a unitary transformation that block-diagonalizes the Dirac Hamiltonian

$$\hat{H}' = \hat{U}_{FW}\hat{H}\hat{U}_{FW}^{\dagger} = \begin{pmatrix} \hat{H}^{+} & 0 \\ 0 & \hat{H}^{-} \end{pmatrix} \tag{2.14}$$

where solutions to the electronic Hamiltonian $\hat{H}^{+}$ are only the electronic solutions and the solutions to the positronic Hamiltonian $\hat{H}^{-}$ are only the positronic solutions. In quantum chemistry, it is typically the electronic solutions that are of interest. The Foldy-Wouthuysen transformation isolates an electron-only Hamiltonian, halving the size of the problem. The transformation $\hat{U}_{FW}$ has the form

$$\hat{U}_{FW} = \begin{pmatrix} \frac{1}{\sqrt{1+\hat{X}^{\dagger}\hat{X}}} & \frac{1}{\sqrt{1+\hat{X}^{\dagger}\hat{X}}}\hat{X}^{\dagger} \\ -\frac{1}{\sqrt{1+\hat{X}\hat{X}^{\dagger}}}\hat{X} & \frac{1}{\sqrt{1+\hat{X}\hat{X}^{\dagger}}} \end{pmatrix} = \begin{pmatrix} \hat{R} & \hat{R}\hat{X}^{\dagger} \\ -\hat{R}_{S}\hat{X} & \hat{R}_{S} \end{pmatrix} \tag{2.15}$$

where $\hat{X}$ is called the decoupling operator and $\hat{R}$ is the renormalization operator. Since the transformation is unitary, it can also be generally parameterized as an exponentiation of a Hermitian operator $\hat{Y}$.[30,31]

$$\hat{U}_{FW} = \exp(-i\hat{Y}) \tag{2.16}$$

An exact transformation exists for a free-particle Hamiltonian

$$\hat{U}_{FPFW} = \hat{A}(1 + \beta\hat{R}) \tag{2.17}$$

where $\hat{A}$, $\hat{R}$, $\hat{E}_p$, and $\hat{D}$ are the kinematic factors.

$$\hat{A} = \sqrt{\frac{\hat{E}_p + c^2}{2\hat{E}_p}} \tag{2.18}$$

$$\hat{R} = \hat{D}c\boldsymbol{\alpha} \cdot \hat{p} \tag{2.19}$$

$$\hat{E}_p = \sqrt{\hat{p}^2 c^2 + c^4} \tag{2.20}$$

$$\hat{D} = \frac{1}{\hat{E}_p + c^2} \tag{2.21}$$

Under a potential, an exact transformation cannot be guaranteed. Nevertheless, an approximate transformation can still be found, and numerous decoupling schemes have been developed over the past decades.[30,31,36–47]

2.1.1 Pauli Hamiltonian

The exponential parametrization allows Equation (2.14) to be expanded in a Baker-Campbell-Hausdorff series.[30,31]

$$\hat{H}' = \hat{H} + i[\hat{Y}, \hat{H}] - \frac{1}{2}[\hat{Y}, [\hat{Y}, \hat{H}]] - \frac{i}{3!}[\hat{Y}, [\hat{Y}, [\hat{Y}, \hat{H}]]] + \dots \tag{2.22}$$

$\hat{Y}$ is chosen such that the commutators cancel off-diagonal blocks of the Dirac Hamiltonian at some order of an expansion parameter. A choice of $\hat{Y}$ is

$$\hat{Y} = -\frac{1}{2c}\beta(\boldsymbol{\alpha} \cdot \hat{p}) \tag{2.23}$$

where the expansion parameter is $\hat{p}/c$. Truncation at second-order arrives at the Pauli Hamiltonian.

$$\hat{H}_+^{(2)} = \beta\left(c^2 + \frac{1}{2}\hat{p}^2 - \frac{1}{8c^2}\hat{p}^4\right) + V + \frac{\nabla^2 V}{8c^2} + \frac{1}{4c^2}\sigma \cdot (\nabla V) \times \hat{p} \tag{2.24}$$

Because powers of the momentum operator greater than two are unbounded, the Pauli Hamiltonian faces variational collapse and can only be used as a perturbative correction.[30,31] Scalar relativity is represented by the first and third terms. The last term is equivalent to the vector relativistic term in Equation (2.13). The vector relativistic term with the Breit Hamiltonian inserted yields the Breit–Pauli Hamiltonian. Most quantum chemistry calculations typically only go as far as including the spin-orbit couplings as spin-spin and orbit-orbit couplings are minuscule for most systems. Thus, the Breit–Pauli Hamiltonian often refers to its truncation at the spin-orbit terms.[48–52] Equation (2.25) is the spin-orbit Breit–Pauli Hamiltonian

$$\hat{H}_{BP} = \frac{1}{2c^2}\left(\sum_{iA}\frac{Z_A}{r_{iA}^3}\hat{l}_i \cdot \hat{s}_i - \sum_{i}\sum_{j\neq i}\frac{1}{r_{ij}^3}\hat{l}_{ij} \cdot (\hat{s}_i + 2\hat{s}_j)\right) \tag{2.25}$$

where $\hat{l}_i$ is the angular momentum operator for electron i with respect to the nucleus, $\hat{l}_{ij}$ is the angular momentum operator for electron i with respect to electron j, and $\hat{s}_i$ is the spin angular momentum operator of electron i. The Breit–Pauli Hamiltonian also suffers from variational collapse as the $1/r^3$ terms are unbounded from below.[48,49] Notice that the vector relativistic term is equivalent to the vector relativistic term in the modified Dirac Hamiltonian in Equation (2.13), which does not include the no-pair approximation. The variational collapse suffered by Breit–Pauli Hamiltonian can be attributed to the Brown–Ravenhall disease.[48]

2.1.2 Douglas–Kroll–Hess Hamiltonian

To arrive at a decoupling transformation suitable for variational treatment, the expansion parameter must not contain $\hat{p}$. The Douglas–Kroll–Hess (DKH) transformation utilizes the potential energy V as the expansion parameter. This is achieved by applying successive unitary transformations to the Dirac Hamiltonian up to some order. The order is defined based on the number of unitary transformations and the order of expansion of the unitary transformations.[30–32,36,40,43,44,53]

$$\hat{H}_{DKHn} = \left(\prod_{m=0} \hat{U}_m\right)\hat{H}\left(\prod_{m=0} \hat{U}_m\right)^\dagger \tag{2.26}$$

The first-order DKH transformation is simply the free-particle Foldy-Wouthuysen transformation.

$$\hat{H}_{DKH1} = \hat{U}_0\hat{H}\hat{U}_0^\dagger = \hat{U}_{FPFW}\hat{H}\hat{U}_{FPFW}^\dagger \tag{2.27}$$

The first-order DKH electronic Hamiltonian is

$$\hat{H}^+_{DKH1} = \hat{E}_p + \hat{A}V\hat{A} + c^2\hat{A}\hat{D}[\hat{p}V \cdot \hat{p} + \sigma \cdot (\nabla V) \times \hat{p}]\hat{D}\hat{A} \tag{2.28}$$

The relativistic potential terms are now dampened by the kinematic factors, making the spin-orbit operator variationally stable.[48,54] The no-pair approximation is implicitly applied when isolating the electronic Hamiltonian while using the kinematic factors. Derivations of higher-order DKH Hamiltonians can be found in work by Nakajima and Hirao[40] as well as Wolf, Reiher, and Hess.[43]

2.1.3 Exact Two-Component Hamiltonian

In the presence of a general potential, Foldy-Wouthuysen transformations previously discussed have been approximate to some order with respect to an expansion parameter. Surprisingly, an exact Foldy-Wouthuysen transformation can be achieved for a general one-particle potential in a one-particle basis representation of the modified Dirac equation. This exact transformation is called the exact two-component (X2C) transformation.[46,47] Conveniently, the problem is already cast into a form suitable for the X2C transformation in the Dirac-Hartree-Fock approximation. Consider the basis representation of the Dirac-Hartree-

Fock equation,

$$\begin{pmatrix} \mathbf{V} & \mathbf{T} \\ \mathbf{T} & \mathbf{W}-\mathbf{T} \end{pmatrix} \begin{pmatrix} \mathbf{C}^{L+} & \mathbf{C}^{L-} \\ \mathbf{C}^{S+} & \mathbf{C}^{S-} \end{pmatrix} = \begin{pmatrix} \mathbf{S} & 0 \\ 0 & \frac{1}{2c^2}\mathbf{T} \end{pmatrix} \begin{pmatrix} \mathbf{C}^{L+} & \mathbf{C}^{L-} \\ \mathbf{C}^{S+} & \mathbf{C}^{S-} \end{pmatrix} \begin{pmatrix} \boldsymbol{\epsilon}^{+} & 0 \\ 0 & \boldsymbol{\epsilon}^{-} \end{pmatrix} \tag{2.29}$$

where $\mathbf{C}^{(L/S)(+/-)}$ are the large/small component basis coefficients for the electronic/positronic solutions. The Dirac-Fock operator is derived from the modified Dirac equation. The X2C transformation takes the form of Equation (2.15).

$$\mathbf{U}_{X2C} = \begin{pmatrix} \mathbf{R} & \mathbf{R}\mathbf{X}^{\dagger} \\ -\mathbf{R}_S\mathbf{X} & \mathbf{R}_S \end{pmatrix} \tag{2.30}$$

$\mathbf{X}$ must be chosen to completely block diagonalizes the Dirac-Fock operator while keeping $\mathbf{U}_{X2C}$ unitary.

$$\mathbf{U}_{X2C} \begin{pmatrix} \mathbf{V} & \mathbf{T} \\ \mathbf{T} & \mathbf{W}-\mathbf{T} \end{pmatrix} \mathbf{U}^{\dagger}_{X2C} = \begin{pmatrix} \mathbf{H}^{+}_{X2C} & 0 \\ 0 & \mathbf{H}^{-}_{X2C} \end{pmatrix} \tag{2.31}$$

One such choice of $\mathbf{X}$ and $\mathbf{R}$ is

$$\mathbf{X} = \mathbf{C}^{S+}(\mathbf{C}^{L+})^{-1} \tag{2.32}$$

$$\mathbf{R} = (\mathbf{1} + \mathbf{X}^{\dagger}\mathbf{X})^{-1/2} \tag{2.33}$$

The electronic X2C Hamiltonian is only dependent on $\mathbf{X}$ and $\mathbf{R}$.

$$\mathbf{H}^{+}_{X2C} = \mathbf{R}\mathbf{V}\mathbf{R}^{\dagger} + \mathbf{R}\mathbf{T}\mathbf{X}\mathbf{R}^{\dagger} + \mathbf{R}\mathbf{X}^{\dagger}\mathbf{T}\mathbf{R}^{\dagger} + \frac{1}{4c^2}\mathbf{R}\mathbf{X}^{\dagger}\mathbf{W}\mathbf{X}\mathbf{R}^{\dagger} - \mathbf{R}\mathbf{X}^{\dagger}\mathbf{T}\mathbf{X}\mathbf{R}^{\dagger} \tag{2.34}$$

Recall that the Hartree-Fock equation must be iteratively solved with the MO coefficients and the Hartree-Fock potential updated at each iteration. Because $\mathbf{X}$ depends on $\mathbf{C}$, the X2C transformation must be updated at each iteration, requiring the diagonalization of the four-component Dirac-Fock matrix. Since the four-component Dirac-Fock matrix is diagonalized anyways, there is no reason to pursue the X2C transformation as the cost of four-component

Dirac-Hartree-Fock is already paid. For this reason, the X2C transformation is only applied to the one-electron Fock matrix since it is constant throughout the calculation. Doing so yields a two-component relativistic one-electron Fock matrix, where the components correspond to α or β spin. The non-relativistic Hartree-Fock potential is added to the one-electron X2C electronic Hamiltonian to account for the electron-electron mean-field

$$\mathbf{H}^{+}_{X2C,1e} = \mathbf{R}\mathbf{V}_{1e}\mathbf{R}^{\dagger} + \mathbf{R}\mathbf{T}\mathbf{X}\mathbf{R}^{\dagger} + \mathbf{R}\mathbf{X}^{\dagger}\mathbf{T}\mathbf{R}^{\dagger} + \frac{1}{4c^2}\mathbf{R}\mathbf{X}^{\dagger}\mathbf{W}_{1e}\mathbf{X}\mathbf{R}^{\dagger} - \mathbf{R}\mathbf{X}^{\dagger}\mathbf{T}\mathbf{X}\mathbf{R}^{\dagger} + \mathbf{G} \tag{2.35}$$

where $\mathbf{G}$ is the non-relativistic Hartree-Fock potential. Because the two-electron interactions are treated non-relativistically, this approximation neglects two-electron angular momenta coupling. Spin-orbit interactions can be vastly overestimated without two-electron spin-orbit coupling. These effects can be accounted for using the screened-nuclear spin-orbit (SNSO) approximation which scales the one-electron spin-orbit integrals by a factor parameterized from Dirac-Hartree-Fock calculations.[55,56] The integrals are scaled in the AO basis based on orbital angular momentum, thus retaining the Hamiltonian symmetry. Similar to the DKH transformation, the no-spin approximation applied when applying the X2C transformation and isolating the electronic Hamiltonian.

2.2 Relativistic Effective Core Potentials

The valence interaction between atoms is the primary area of focus for much of the chemical sciences. As electrons move further from the nucleus, the nuclear-electronic potential weakens with distance and is further reduced by shielding from core electrons. The weakened potential reduces the speed of the electron, therefore weakening relativistic effects. Though the probability distribution of valence electrons mostly lie further from the nucleus, valence electrons still possess some probability density near the nucleus, experiencing stronger relativistic effects than expected. Furthermore, valence electrons are indirectly affected by relativistic effects due to the orthogonality condition and correlation with core electrons. Changes to core orbitals due to relativity must be met with changes to valence orbitals to

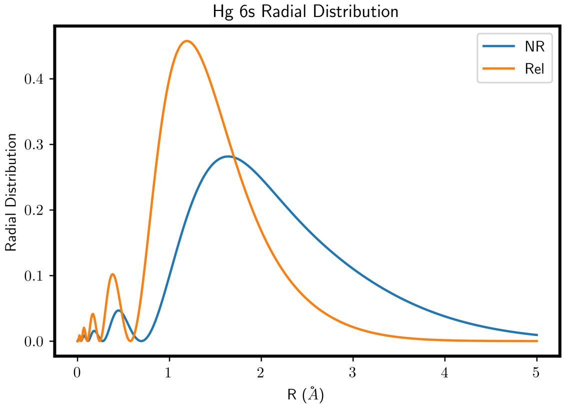

Figure 2.1: Radial distribution function of the Hg $6s$ orbital with (orange) and without scalar relativity (orange).

maintain orthogonality.[27] Figure 2.1 shows the radial distribution of the $6s$ electron computed with and without scalar relativity. A notable amount of electron density can be seen less than a Bohr radius away from the nucleus. More significantly, scalar relativity contracts the radial distribution of the $6s$ orbital by over 25%.

The strong electron correlation and large amount of electrons in late-row elements make simulations extremely expensive, especially in large system with many late-row atoms. The additional cost of indispensable relativistic effects adds further cost onto these simulations. Effective core potentials (ECPs) offer an efficient way to reduce computational cost by replacing localized core electrons with a potential. In the past several decades, numerous ECPs have been developed to include scalar relativistic effects. A few potentials even offer an additional term for spin–orbit coupling.

The Schrödinger equation suffices when including relativistic effects using ECPs. The ECP is simply an additional operator in the Hamiltonian. At the time of development, different families of ECPs may have different functional forms and parameters. Most software packages to adhere to a single ECP functional form. This Thesis will introduce the Kahn-type ECP[57] implemented in the Gaussian electronic structure software package. An electronic

Hamiltonian with an ECP is written as

$$\hat{H} = -\frac{1}{2}\sum_{i}^{N_{val}} \nabla_i^2 - \sum_{i}^{N_{val}}\sum_{A} \frac{Z_A - N_A^{core}}{r_{iA}} + \sum_{i<j}^{N_{val}} \frac{1}{r_{ij}} + \sum_{i}^{N_{val}} \hat{V}_{ECP}(r_i) \tag{2.36}$$

where N_{val} is the number of valence electrons, N_A^{core} is the number of core electrons on atom A, and $\hat{V}_{ECP}$ is the ECP operator. The one-electron Fock operator with an ECP is written as

$$\hat{f}_i = -\frac{1}{2}\nabla_i^2 - \sum_{A} \frac{Z_A - N_A^{core}}{r_{iA}} + \bar{V}_i + \hat{V}_{ECP}(r_i) \tag{2.37}$$

The Kahn-type ECPs were originally developed to be non-relativistic and were later adapted to include relativistic effects. Adaptation to scalar relativity only requires a refitting of the ECP parameter. However, spin–orbit coupling requires an entirely new operator.[58,59] Averaged relativistic ECPs (AREPs) opt for an averaged inclusion of spin–orbit coupling by fitting to an average between $j = l \pm 1/2$ orbital energies, providing some energy corrections from spin–orbit coupling without resolving fine-structure splitting. Some families of AREPs still offer parameters for the spin–orbit operator to resolve fine-structure splitting.[60,61]

The ECP operator is a one-electron operator consisting of two parts: the original Kahn-type ECP operator $\hat{V}^{Kahn}$ and the spin–orbit operator $\hat{H}_{SO}$.

$$\hat{V}_{ECP} = \hat{V}^{Kahn} + \hat{H}_{SO} \tag{2.38}$$

The Kahn-type ECP operator is written as

$$\hat{V}^{Kahn} = U_L^{Kahn} + \sum_{l=0}^{L} \sum_{m_l=-l}^{l} (U_l^{Kahn} - U_L^{Kahn})|lm_l\rangle\langle lm_l| \tag{2.39}$$

where U_l^{Kahn} is the l orbital angular momentum effective potential fitted to the form

$$U_l^{Kahn} = \frac{1}{r^2}\sum_{k} C_{lk} r^{n_{lk}} \exp\left(-\zeta_{lk} r^2\right) \tag{2.40}$$

with fitting parameters C_{lk}, n_{lk}, and ζ_{lk}.[57,60,61] The functional form of the potential is chosen to be a linear combination of Gaussian functions for efficient computation. The maximum orbital angular momentum of the ECP L must be at least one higher than the largest core orbital angular momentum.[57] Notice that U_l^{Kahn} is purely a radial operator, yet has orbital angular momentum as a descriptor. The operator only distinguishes orbital angular momentum through the projection operator, which is accompanied by a radial potential where U_L^{Kahn} is subtracted out. The potential $U_l^{Kahn} - U_L^{Kahn}$ represents core-valence interactions between orbitals with l orbital angular momentum and U_L^{Kahn} represents core-valence interactions across different orbital angular momenta. The parameters for $U_l^{Kahn} - U_L^{Kahn}$ are typically published instead of U_l^{Kahn} parameters for $l < L$.[60]

Though AREPs include an averaged spin–orbit coupling, it does not resolve fine-structure splitting. The ECP spin–orbit operator acts as a correction to the AREP operator to recover fine-structure splitting. The ECP spin–orbit operator is written as[58–61]

$$\hat{H}_{SO} = \hat{\mathbf{s}} \cdot \sum_{l=1}^{L} \frac{2}{l} U_l^{SO} \sum_{m_l=-l}^{l} \sum_{m_l'=-l}^{l} |lm_l\rangle\langle lm_l|\hat{\mathbf{l}}|lm_l'\rangle\langle lm_l'| \tag{2.41}$$

The spin–orbit potentials U_l^{SO} are fitted to the same form as Equation (2.40), typically sharing the same exponents. One must be cautious of different fitting conventions between families of ECPs. One notable difference is that the published coefficients for the CRENBL ECPs are consistent with Equation (2.41) while the $2/l$ factor is absorbed into the Stuttgart ECP coefficients.[60,61]

2.3 Spin–Orbit Coupling

The central term in spin–orbit operators is the coupling between spin and orbital angular momentum of an individual electron,

$$\hat{h}_{SO} = \lambda \hat{\mathbf{l}} \cdot \hat{\mathbf{s}} \tag{2.42}$$

where λ is a pre-factor that depends on the choice of spin–orbit Hamiltonian. This coupling term can be written as

$$\hat{\mathbf{l}} \cdot \hat{\mathbf{s}} = \frac{1}{2}(\hat{\mathbf{j}}^2 - \hat{\mathbf{l}}^2 - \hat{\mathbf{s}}^2) \tag{2.43}$$

where $\mathbf{j}$ is the total angular momentum operator.

$$\hat{\mathbf{j}} = \hat{\mathbf{l}} + \hat{\mathbf{s}} \tag{2.44}$$

In an N-electron system, the spin–orbit operator is a sum of one-electron spin–orbit operators.

$$\hat{H}_{SO} = \sum_i \lambda(\mathbf{x}_i)\hat{\mathbf{l}}(\mathbf{x}_i) \cdot \hat{\mathbf{s}}(\mathbf{x}_i) \tag{2.45}$$

Angular momentum operators can also be constructed for N-electron systems by summing the angular momenta over individual electrons.

$$\hat{\mathbf{L}} = \sum_i \hat{\mathbf{l}}(\mathbf{x}_i) \tag{2.46}$$

$$\hat{\mathbf{S}} = \sum_i \hat{\mathbf{s}}(\mathbf{x}_i) \tag{2.47}$$

$$\hat{\mathbf{J}} = \sum_i \hat{\mathbf{j}}(\mathbf{x}_i) \tag{2.48}$$

2.3.1 Spin–Orbit Coupling in Atoms – LS and jj-Coupling

In non-relativistic quantum mechanics, the one-electron atomic Hamiltonian commutes with $\hat{l}^2$ and $\hat{s}^2$, resulting in a shared set of eigenstates for these operators. As a result, atomic states are described by two quantum numbers: s, representing spin angular momentum, and l, representing orbital angular momentum. Extending this to an N-electron system, the atomic Hamiltonian commutes with the N-electron squared angular momentum operators $\hat{L}^2$ and $\hat{S}^2$. Each N-electron atomic state is described by a term symbol, ${}^{2S+1}L^p$, where S is the N-electron spin quantum number and L is the N-electron orbital quantum number.

The L quantum number is conventionally expressed using spectroscopic notation: $L = 0$ (S), $L = 1$ (P), $L = 2$ (D), and so on. The superscript denotes the parity of the wave function, with $p = o$ for an odd wave function and omitted for an even wave function.

The emergence of spin–orbit coupling in the one-electron atomic Hamiltonian gives rise to a new quantum number, j, corresponding to eigenstates of $\hat{j}^2$. Since the squared angular momentum operators commute with each other as well as the one-electron Hamiltonian, s, l, and j remain as good quantum numbers. However, in the N-electron case, only $\hat{J}^2$ commutes with the N-electron spin–orbit Hamiltonian, meaning that L and S are no longer good quantum numbers.

The fact that $\hat{L}^2$ and $\hat{S}^2$ no longer commute with the Hamiltonian allows for mixing between states with different L and S, as long as the states share the same J. This mixing of different L and S states leads to the degradation of L and S as good quantum numbers. The degree of this degradation depends on the strength of spin–orbit coupling. At the weak coupling limit, systems tend to mostly retain L and S as good quantum numbers. For example, the ground state of the neutral carbon atom is $J = 0$, but still consists of 98% ^3P character.[62,63] In these cases, it is fair to describe the state with a term symbol that includes all three quantum numbers, $^{2S+1}L^p_J$. A case where this description is inappropriate is the ground state of the neutral cerium atom, which is $J = 4$ but consists of 55% $^1G^o_4$ character and 29% $^3H^o_4$ character.[63,64]

Spin–orbit coupling is traditionally described using two schemes: LS-coupling and jj-coupling.[65–69] In the LS-coupling scheme, as discussed above, $^{2S+1}L^p$ states are first formed before coupling L and S to obtain $^{2S+1}L^p_J$ states. The coupling is explicitly achieved by taking linear combinations of L and S microstates. The mixing of microstates within the same $^{2S+1}L^p$ manifold under the spin–orbit Hamiltonian is the primary source of fine-structure splitting at the weak coupling limit. It is typically taught that LS-coupling is only valid when spin–orbit coupling is much weaker than electrostatic interactions. The reasoning behind this claim is that the electrostatic interaction is responsible for the emergence of the L quantum number, and its dominance preserves the L-purity of the J-state. When comparable to the electrostatic interaction, strong spin–orbit coupling can significantly alter the wave function, causing it to deviate substantially from its non-relativistic solution and lose L-purity.[64,70] This can be captured by mixing states outside of a given ${}^{2S+1}L^p$ manifold, as shown previously for the ground state of the neutral cerium atom. LS-coupling does not typically account for the mixing between different ${}^{2S+1}L^p$ manifold, making it unsuitable for strong spin–orbit coupling.

The preferred coupling scheme for strong spin–orbit coupling is jj-coupling, where l and s for individual orbitals are coupled to obtain j-orbitals before coupling individual electrons into N-electron J-states. These J-states are not guaranteed to have well-defined L and S values and can more compactly describe spin–orbit coupling than taking linear combinations of ${}^{2S+1}L^p$.

Spin–orbit coupling is not typically seen through the lens of LS and jj-coupling in *ab initio* relativistic electronic structure theory, but some methods bear strong resemblance to these coupling schemes. The fully variational treatment of spin–orbit coupling mirrors jj-coupling while state interaction mirrors LS-coupling. This is discussed in greater detail in Section 3.2.4

2.3.2 Spin–Orbit Coupling in Atoms – Double Group Theory

A wealth of information about a molecule can be deduced from its symmetry. Molecular symmetry is described by a symmetry group, a collection of operations that leave molecular geometry unchanged. These operations are called symmetry operations and collectively form a mathematical object called a group. Group theory is a branch of mathematics that studies groups. Its findings are routinely used in non-relativistic quantum chemistry to deduce molecular properties without explicit calculation.[65,66,68]

All quantum states of a molecule and canonical SCF orbitals can be described by an irreducible representation (irrep) of the symmetry group. Along with describing how a state transforms under symmetry operations, the irrep also indicates the degeneracy of the state. Moreover, operators can also be described by an irrep. Determining whether a molecular property is non-zero requires determining whether its underlying integrals are non-zero. An integral is non-zero only if the direct product of the irreps representing the operator and the states involved contain the totally symmetric irrep $\Gamma(1)$.[65,66,68] Direct products of irreps are tabulated in various texts.[68,71]

The introduction of spin–orbit coupling splits non-relativistic degeneracies, implying spin–orbit coupling breaks symmetry. Non-relativistic group theory is blindsided by spin–orbit coupling because it only considers spatial symmetry. An accurate description of relativistic symmetry must consider the spin symmetry described by the Lie group $SU(2)$ along with the spatial symmetry described by subgroups of $O(3)$.[30,31,72] Skipping through the dense mathematics, each spatial symmetry group arrives at a relativistic counterpart which we call the double symmetry group. Group theory analysis within double group theory is the same as non-relativistic group theory with a few additions. Double symmetry groups contain two sets of irreps: bosonic and fermionic. Bosonic irreps are exactly the same as the non-relativistic irreps. Direct products of irreps in double group theory are expanded to include bosonic-fermionic and fermionic-fermionic products, which are tabulated in Altmann and Herzig.[71]

When spin is considered in non-relativistic group theory, it is an *a posteriori* descriptor on top of the spatial irrep. The non-relativistic irrep is transformed to the double group irrep by a direct product between the spatial irrep and the spin irrep.

$$^{2S+1}\Gamma \mapsto \Gamma(S) \otimes \Gamma \tag{2.49}$$

In centrosymmetric groups, spin irreps are always *gerade*.[30,31,72]

Figure 2.2 illustrates the fine-structure splitting of orbitals in terms of double group theory. Without spin–orbit coupling, the ligand field splits the d-orbitals into a six-fold degenerate t_2 manifold and a four-fold degenerate e manifold. We also include a set of non-bonding t_1 ligand p-orbitals in this example. To incorporate spin symmetry, a direct product is taken between these spatial irreps and their spin irrep.[48,73] Since orbitals are one-electron

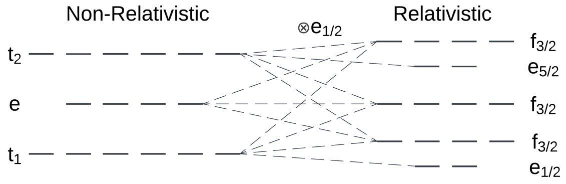

Figure 2.2: Fine-structure splitting of orbitals in a T_d ligand field.

states, the spin irrep is $e_{1/2}$ describing $s = 1/2$. The non-relativistic t_2 splits into a four-fold degenerate $f_{3/2}$ manifold and two-fold degenerate $e_{5/2}$ manifold, revealing the fine-structure splitting pattern. Spin–orbit coupling also facilitates the mixing of spatial orbitals. Because all three spatial irreps transform or split into $f_{3/2}$, the d-orbitals and ligand non-bonding p-orbitals are allowed to mix in the $f_{3/2}$ manifolds, further deviating from the non-relativistic spatial symmetry. After coupling spin and spatial irreps at the orbital level, occupied orbitals can be coupled in a manner akin to non-relativistic group theory to obtain N-electron state irreps. This coupling scheme to arrive at N-electron wave functions is the molecular analog to jj-coupling.

It is also valid to first form non-relativistic N-electron states and then couple the N-electron spatial irrep with N-electron spin irrep. This coupling scheme is the molecular analogue of LS-coupling. Nevertheless, both coupling schemes arrive at the same double double groups irreps.

Chapter 3

STATE INTERACTION

Suppose the Hamiltonian can be partitioned into two parts: a zeroth-order Hamiltonian $\mathbf{H}^0$ and a perturbing Hamiltonian $\mathbf{H}^1$,

$$\mathbf{H} = \mathbf{H}^0 + \mathbf{H}^1 \tag{3.1}$$

where solutions to the zeroth-order Hamiltonian $\mathbf{H}^0$ can be found more easily than the full Hamiltonian $\mathbf{H}$. By first solving for the eigenstates of $\mathbf{H}^0$, the eigenstates can be used as a basis to construct $\mathbf{H}^1$ and subsequently $\mathbf{H}$. The basis of zeroth-order states is called the interaction space. Diagonalizing $\mathbf{H}$ in the interaction space yields eigenstates of the full Hamiltonian as linear combinations of the zeroth-order states. This approach to solving the full eigenvalue problem is called state interaction.[74] At the limit where the interaction space encompasses all zeroth-order states, $\mathbf{H}^1$ is treated at the same level of theory as $\mathbf{H}^0$. In practice, only a subset of zeroth-order states can be feasibly computed, leading to an approximate treatment of $\mathbf{H}^1$ at a smaller basis. The interaction space must be carefully selected to sufficiently span $\mathbf{H}^1$ while maintaining reasonable cost.

The previous sections have shown that relativistic Hamiltonians can be partitioned into a scalar relativistic and a vector relativistic part.

$$\mathbf{H} = \mathbf{H}_{sr} + \mathbf{H}_{vr} \tag{3.2}$$

Even after reducing the Dirac equation to an approximate two-component form, the relativistic eigenvalue problem is still much more expensive than its non-relativistic or scalar relativistic counterpart. The fully variational treatment of vector relativity requires the non-collinear optimization of spin orbitals.[30,31,75–82] This limits the relativistic wave function *ansatz* to contain at least two independent α and β spin components. Moreover, the wave function must be complex to thoroughly capture the $SU(2)$ symmetry inherent to total (and spin) angular momentum. Not only do the extra components double the dimension of the problem, complex arithmetic also doubles the memory requirement, increases the floating-point operation (FLOP) count by eight-fold, and slows the convergence of iterative methods. Neglecting vector relativity allows for the reduction of the relativistic Hamiltonian to a one-component form since the scalar relativistic Hamiltonian preserves spin as a good quantum number. Mathematically, this is reflected in $\mathbf{H}_{sr}$ being block-diagonal with respect to $\alpha\alpha$ and $\beta\beta$ blocks with each block being identical. The two-component Hamiltonian can be reduced to one-component by using only one spin block. Just as in non-relativistic quantum mechanics, spin is added *a posteriori*. The non-variational treatment of spin allows the scalar relativistic problem to be entirely real-valued. Scalar relativity is much stronger than vector relativity, manifesting earlier in the periodic table. Vector relativity can be neglected in modeling many properties for systems involving elements towards the middle of the periodic table, leaving a scalar relativistic problem with nearly the same cost as a non-relativistic problem.[83–86]

For systems where vector relativity cannot be neglected, state interaction is a cost-effective method for the including vector relativity without completely bearing the heavy cost of complex multi-component wave functions.[52,87–95] By assigning $\mathbf{H}_{sr}$ as the zeroth-order Hamiltonian, expensive iterative electronic structure methods can be entirely one-component and real-valued. Spin can be added *a posteriori* to the one-component zeroth-order wave functions and projected to two-component form. Complex arithmetic is only necessary when constructing and diagonalizing the full relativistic Hamiltonian in the interaction space.

3.1 State Interaction in CI Methods

The workflow of a typical CI calculation is shown in Figure 3.1. Starting from an AO basis, MOs are generated using Kohn–Sham DFT or the Hartree–Fock approximation. The

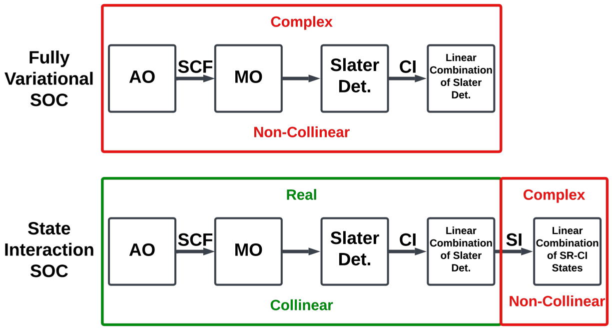

Figure 3.1: Comparison between fully variational and state interaction spin–orbit coupling.

many-body Hamiltonian is represented in a Slater determinant basis formed from these MOs. This Hamiltonian is diagonalized to yield CI wave functions as linear combinations of Slater determinants. Sufficiently capturing static correlation in a Slater determinant basis built from Kohn–Sham or Hartree–Fock MOs can require a large number of determinants. MCSCF is typically used to optimize a set of MOs so that the determinant expansion of the multi-configurational states can be more compact, reducing the dimensionality of the CI problem. Nevertheless, an MCSCF wave function is still a CI wave function.

Vector relativity and static correlation become increasingly prevalent towards the bottom of the periodic table. In addition to partially filled degeneracies frequently seen in metal complexes, f-block complexes have been notorious for possessing multi-configurational ground states.[63,64,70,96] This makes MCSCF an indispensable tool for exploring f-block and late transition metal chemistry. State interaction provides substantial cost reduction to relativistic MCSCF. Along with the advantages of a one-component real-valued wave function discussed previously, one-component scalar relativistic MCSCF requires fewer CI solutions at each iteration since it is unnecessary to resolve spin microstates to capture static correlation.

State interaction within relativistic CI uses an interaction space of scalar relativistic CI wave functions. Because the interaction space is a subset of the eigenbasis of the scalar relativistic CI Hamiltonian, $\mathbf{H}_{sr}$ is a diagonal matrix of CI energies.

$$\mathbf{H}_{sr} = \begin{pmatrix} \omega_0 & & \\ & \omega_1 & \\ & & \ddots \end{pmatrix} \tag{3.3}$$

Matrix elements of the one-electron vector relativistic Hamiltonian between states I and J can be formed by contracting the one-particle transition density matrix $\boldsymbol{\gamma}^{\mathbf{IJ}}$ with the underlying one-electron vector relativistic Hamiltonian $\mathbf{h}_{vr,1e}$.

$$H_{vr}^{IJ} = \langle I | \hat{H}_{vr} | J \rangle = \sum_{pq} \gamma_{pq}^{IJ} h_{vr,1e}^{pq} \tag{3.4}$$

Two-electron vector relativity can be included beyond the screened-nuclear spin-orbit approximation in a similar manner by flattening the two-electron operator to a one-electron operator via the mean-field approximation. Keep in mind that the underlying orbitals used in this mean-field approximation are not optimized self-consistently in the presence of two-electron vector relativity in state interaction.

There is one caveat that must be addressed if one chooses to flatten the zeroth-order problem to one-component. If the one-component CI calculation does not include spin-flip excitations,[97] only one M_S state is yielded, thus insufficiently spanning the vector relativistic operator. Previous implementations of state interaction overcome this by invoking the Wigner-Eckart theorem, which takes advantage symmetries inherent to angular momentum to deduce the density matrices involving other M_S states. In our implementation, the one-component CASSCF orbital basis was projected into a two-component spinor basis before solving one last CI problem to yield the complete M_S manifold.[95]

3.1.1 Atomic Fine-Structure Splitting

In this section, the accuracy of three methods for including both scalar relativity and spin–orbit coupling are assessed by comparing excitation energies of J-manifolds arising from the lowest term due to fine-structure splitting. The three methods being compared are the X2C-CASSCF and srX2C-CASSCF-SO methods implemented on a developmental version of Gaussian,[76,95,98] and the CASSCF-SO method available in OpenMolCAS.[99] X2C-CASSCF treats both scalar relativity and spin-orbit coupling on the same footing by using the one-electron X2C Hamiltonian with the Dirac–Coulomb–Breit-parameterized SNSO approximation in the CASSCF calculation.[55,56,76] Both srX2C-CASSCF-SO and CASSCF-SO treat spin–orbit coupling via state interaction, but differ on the choice of relativistic Hamiltonian. In srX2C-CASSCF-SO, the zeroth-order Hamiltonian is the scalar relativistic one-electron X2C Hamiltonian and the perturbing Hamiltonian is the vector relativistic one-electron X2C Hamiltonian with the Dirac–Coulomb–Breit-parameterized SNSO approximation.[55,56,95] In CASSCF-SO, the scalar relativistic DKH2 Hamiltonian is the zeroth-order Hamiltonian.[74,87,99] The perturbing Hamiltonian is the one-electron DKH spin–orbit Hamiltonian along with the atomic-mean-field two-electron Breit–Pauli spin–orbit Hamiltonian.[54,100]

All systems used in the benchmark have a partially-filled valence subshell configuration. For each term, the active space comprised of all valence orbitals. For example, Pr is in the $4f$-block and has a partially-filled valence subshell configuration of $4f^3$. The active space for Pr comprises of 14 orbitals (7 α-orbitals and 7 β-orbitals) and 3 electrons where all 14 orbitals were $4f$ orbitals. All CASSCF states arising from the active space were included in the interaction space. Experimental results were obtained from the NIST Atomic Spectra Database.[63,64]

Table 3.1 shows the mean and maximum absolute errors of each method with respect to blocks of the periodic table. The error for each method increases along with atomic number. The difference in accuracy between the two state interaction methods is small, in the range of 1-27 meV, with CASSCF-SO being more accurate. Calculations without the consideration of two-electron spin–orbit coupling show that the difference is mainly due to different two-electron spin–orbit approximations. For atomic fine-structure splitting, the benchmark shows that the atomic-mean-field approximation is more accurate than the SNSO approximation.

Table 3.1: Mean and maximum absolute error of atomic excitation energies (in eV) for CASSCF-SO, srX2C-CASSCF-SO, and X2C-CASSCF. The table is divided into blocks of the periodic table (4*d*, 5*d*, 5*p*, etc.). Errors for the 5*d* block with Os and Ir omitted are place in parentheses. The average experimental splitting is defined as the average energy difference between adjacent *J*-states. All calculations were performed using the ANO-RCC basis set.[2,3] Absolute error (AE) is defined as the unsigned difference between the computed value and the experimental value.

	Mean AE	**Max AE**	**Average Exp Splitting**
4d (Y, Zr, Nb, Ru, Rh)			0.083
CASSCF-SO[a]	0.008	0.034	
srX2C-CASSCF-SO[b]	0.012	0.041	
X2C-CASSCF[b]	0.011	0.030	
5d (Hf, Ta, W, Os, Ir)			0.223
CASSCF-SO	0.144 (0.042)	0.778 (0.114)	
srX2C-CASSCF-SO	0.149 (0.053)	0.790 (0.095)	
X2C-CASSCF	0.141 (0.066)	0.711 (0.094)	
5p (In, Sn, Te, I)			0.372
CASSCF-SO	0.047	0.080	
srX2C-CASSCF-SO	0.048	0.083	
X2C-CASSCF	0.034	0.053	
6p (Tl, Pb, Po)			0.875
CASSCF-SO	0.195	0.309	
srX2C-CASSCF-SO	0.212	0.346	
X2C-CASSCF	0.187	0.340	
4f (Pr, Nd, Pm, Sm, Dy, Ho, Tm)			0.233
CASSCF-SO	0.034	0.110	
srX2C-CASSCF-SO	0.043	0.126	
X2C-CASSCF	0.014	0.076	
5f (U^{3+}, Np^{3+}, Pu^{3+})			0.215
CASSCF-SO	0.219	0.666	
srX2C-CASSCF-SO	0.246	0.644	
X2C-CASSCF[c]	0.208	0.614	

[a] Atomic-mean-field two-electron integrals are used.

[b] Dirac–Coulomb–Breit-parameterized row-dependent screened-nuclear spin-orbit scaling is used.

[c] State-averaged over the first *J*-manifold.

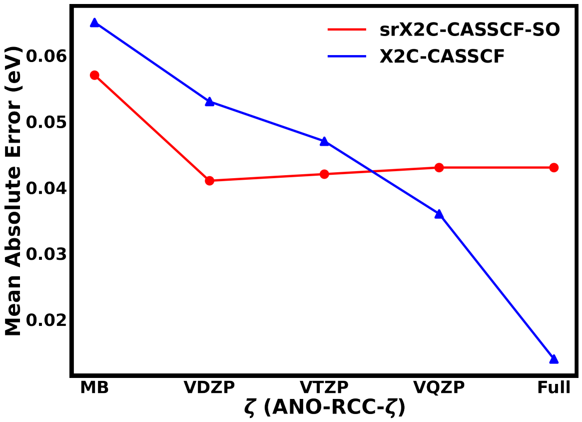

Figure 3.2: Mean absolute error (eV) of the ground state fine structure splitting for the $4f$-block using srX2C-CASSCF-SO and X2C-CASSCF was plotted as a function of basis set ζ.

X2C-CASSCF outperformed the state interaction methods in mean absolute error in all blocks besides the $4d$-block. The errors between X2C-CASSCF and srX2C-CASSCF-SO differ on the range of 1-38 meV. Errors are significantly higher for the $5d$, $6p$, and $5f$-blocks for all three methods. These errors have been previously observed in both fully variational and state interaction methods and have been shown to improve with more dynamic correlation. Omitting highly correlated cases in the $5d$ block where the breaking of Hund's rule is observed (Ir and Os) significantly reduced the mean and max absolute errors.

Figure 3.2 shows the mean absolute error of ground state fine-structure splitting for the $4f$-block computed using srX2C-CASSCF-SO and X2C-CASSCF as these methods approach the basis set limit. Basis set convergence behavior has been studied in the previous work for state interaction spin–orbit coupling but has not been compared to a fully variational spin–orbit approach.[101] Improvement was seen in both srX2C-CASSCF-SO and X2C-CASSCF when improving the basis past VDZP-quality from the minimal basis (MB) to double-zeta (VDZP). Improving the basis had negligible effect on srX2C-CASSCF-SO results whereas X2C-CASSCF showed systematic improvement. In the fully variational treatment of spin–orbit coupling, the spin–orbit operator is represented in the entire orbital basis. In state interaction, the spin–orbit operator is represented in the interaction space which is limited by the active space. The initial improvement in both methods was due to the improved description of the $4f$ orbitals. However, increasing the basis set size past VDZP-quality did not significantly improve the description of the $4f$ orbitals. Because the spin–orbit operator is only represented within the active space of only $4f$ orbital in state interaction, without improvement of the $4f$ orbitals, increasing basis size minimally affected the state interaction results. Conversely, the fully variational result continues to improve since the spin–orbit operator is not restricted by the active space.

3.1.2 Dependence of Fine-Structure Splitting of NdO$^+$ on Interaction Space

At the full CI limit, when the interaction space encompasses all zeroth-order states, the fully variational and state interaction methods should be identical. Within the CASSCF level of theory, the best representation of the spin–orbit Hamiltonian for a given active space is constructed from an interaction space that encompasses all zeroth-order CASSCF states. The results of the atomic benchmark was somewhat misleading in the sense that we only show the ideal cases where we can afford to utilize the maximum interaction space. In this section, we explore the behavior of state interaction spin–orbit coupling as a function of interaction space.

At the CASSCF level of theory, low-lying excited states of NdO$^+$ exist in a dense manifold of 52 states.[102] A spin-free treatment of these states yield a set of multiplets spanning ~0.17 eV. With spin–orbit coupling in consideration, these multiplets split into degenerate Kramers pairs spanning ~1.00 eV. The bond length of NdO$^+$ was set to 1.742 Å, which was optimized at the CASSCF level of theory in previous work.[102] The active space was chosen to be 3 electrons and 14 spin orbitals for srX2C-CASSCF-SO and X2C-CASSCF. Orbitals with majority $4f$ character were chosen to be in the active space. Calculations were state averaged over the lowest 52 states, which were all included in the interaction space. The ANO-RCC-VQZP basis set was used in these calculations.[2,3]

Table 3.2 shows excitation energies for low-lying states of NdO$^+$ calculated using srX2C-

Table 3.2: Excitation energies (in eV) for low-lying excited states of NdO^+ for various interaction spaces of size N. Absolute error (AE) in this table is defined as the unsigned difference between the perturbative srX2C-CASSCF-SO result and X2C-CASSCF. The ground state error was omitted from the mean AE.

J_a	Ω	srX2C-CASSCF-SO						X2C-CASSCF	Exp.
		$N = 22$	$N = 36$	$N = 52$	$N = 68$	$N = 86$	$N = 364$		
4.5	4.5	0.000	0.000	0.000	0.000	0.000	0.000	0.000	0.000
4.5	3.5	0.174	0.144	0.118	0.161	0.115	0.115	0.115	0.159
4.5	2.5	0.281	0.219	0.156	0.199	0.152	0.151	0.151	0.191
4.5	1.5	0.368	0.243	0.159	0.201	0.154	0.154	0.154	0.201
4.5	0.5	0.453	0.341	0.161	0.203	0.156	0.156	0.155	0.213
5.5	5.5	0.530	0.367	0.224	0.250	0.252	0.252	0.251	0.228
5.5	4.5	0.608	0.378	0.322	0.365	0.348	0.349	0.348	0.366
5.5	3.5	0.690	0.517	0.359	0.401	0.385	0.385	0.384	0.401
5.5	2.5	0.701	0.563	0.373	0.416	0.399	0.400	0.399	
5.5	1.5	0.749	0.596	0.376	0.419	0.402	0.403	0.403	
5.5	0.5	0.793	0.609	0.377	0.419	0.403	0.403	0.403	
Mean AE		0.235	0.110	0.016	0.025	0.000	0.000		
Max AE		0.390	0.206	0.027	0.048	0.001	0.001		

CASSCF-SO and X2C-CASSCF as well as their experimental excitation energies. States are denoted as (J_a, Ω) where J_a is the total electronic angular momentum of the atomic ion and Ω labels the unsigned projection of J_a on the internuclear axis. We define the absolute error (AE) to be the unsigned difference between the srX2C-CASSCF-SO and X2C-CASSCF results for each computed state. Mean and maximum AEs are also recorded in Table 3.2. The lowest few experimentally observed states were included as a reference. Results with interaction spaces of sizes $86 < N < 364$ can be found in the Supporting Information of the original work.[95]

We begin with the minimum interaction space required to recover the first two J_a manifolds, $N = 22$. We increase the interaction space by adding states in energetic order. The maximum interaction space size is $N = 364$ states. To recover excitation energies that rival the accuracy of X2C-CASSCF, the interaction space must encompass at least the 86 lowest spin-free states.

In Table 3.2, only interaction spaces that preserve the Kramers degeneracy of (J_a, Ω)

Table 3.3: Excitation energies (in eV) for low-lying excited states of NdO^+ for various inadequate interaction spaces that lead to unphysical degeneracy breaking. Kramers pairs with degeneracy breaking greater than 1 meV are in bold.

J_a	Ω	$N = 24$	$N = 34$	$N = 51$
4.5	4.5	0.000	0.000	0.000
		0.000	0.000	0.000
4.5	3.5	0.179	0.141	**0.118**
		0.179	0.141	**0.119**
4.5	2.5	0.291	**0.214**	0.156
		0.291	**0.224**	0.156
4.5	1.5	0.382	**0.224**	**0.159**
		0.382	**0.307**	**0.160**
4.5	0.5	0.470	0.326	**0.161**
		0.470	0.326	**0.196**
5.5	5.5	**0.559**	0.346	0.224
		0.561	0.346	0.224
5.5	4.5	**0.564**	**0.361**	0.322
		0.567	**0.364**	0.322
5.5	3.5	0.654	0.475	**0.359**
		0.654	0.475	**0.363**
5.5	2.5	0.740	**0.531**	0.373
		0.740	**0.559**	0.373
5.5	1.5	0.762	**0.559**	0.376
		0.762	**0.568**	0.376
5.5	0.5	0.804	**0.568**	**0.377**
		0.804	**0.633**	**0.475**

manifolds were shown. Table 3.3 shows state interaction results resulting from inadequate interaction spaces. Interaction spaces where degenerate manifolds are partially included yield solutions with unphysical degeneracy breaking.

The low-lying J_a manifolds of NdO^+ are $J_a = 4.5$, 5.5, 6.5, 7.5 where each J_a manifold has 10, 12, 14, and 16 microstates respectively. An interaction space of 34 omits two states from the $J_a = 6.5$ manifold as well as two states from an eight-fold spin-free degeneracy. This caused degeneracy breaking between Kramers pairs in the $J_a = 4.5$ manifold on the order of 10 meV. Kramers degeneracy breaking was observed on the order of 1 meV in the $J_a = 6.5$ manifold when using an interaction sapce of $N = 24$, which includes only two states from the $J_a = 6.5$ manifold without the partial inclusion of spin-free degeneracies. Kramers degeneracy breaking was not observed for the $N = 22$ interaction space, where no states were excluded from J_a manifolds and two states were excluded from an eight-fold spin-free degeneracy. Furthermore, excluding a single complement to a Kramers pair also yields degeneracy breaking up to 98 meV, as demonstrated by the interaction space $N = 51$.

Our analysis shows that an appropriate interaction space is imperative for sound results. Not only does an incomplete interaction space yield erroneous energies, it can misrepresent the physics of the systems. One must be cautious when employing state interaction and ensure the interaction space have reached convergence, or at the very least, cover the symmetry of the system.

3.1.3 Four-Component State Interaction

Traditionally, state interaction has only been applied to decoupled electronic relativistic Hamiltonians which have been spin-separated into a scalar relativistic term and a spin–orbit term.[33] Two-electron spin–orbit coupling has typically been treated in state interaction using the two-electron Breit–Pauli spin–orbit Hamiltonian or the Dirac–Coulomb(–Gaunt/Breit) operator under a mean-field approximation.[54,82,100] It is possible to include spin–spin and orbit–orbit coupling via state interaction, given that the Breit–Pauli Hamiltonian contains theses terms are explicitly, but this has yet to be done. With the advent of scalar Coulomb and Breit operators, we move towards efficiently incorporating all aspects of the Dirac-Coulomb-Breit Hamiltonian via state interaction.[35]

Note that spin-separation of the term involving the nuclear-electronic potential via the Dirac relation gives rise to the scalar-vector partitioning where spin–orbit coupling is the only vector relativistic effect. The scalar Hamiltonian from this partitioning does not include the spin operator, hence, the scalar and vector relativistic terms are often referred to as the spin-free and spin-dependent terms. We must be careful by acknowledging that the scalar relativistic Breit operator consists of the spin operator. Thus, the partitioning of the Breit operator cannot be referred to as spin-separation nor can the scalar relativistic Breit operator be called spin-free despite also arising from the Dirac relation.

Presently, reduction of the scalar Breit operator to one or two-component form has yet to be achieved, requiring a four-spinor wave function. Nevertheless, the scalar Dirac-Coulomb-Breit Hamiltonian is entirely real-valued and requires significantly fewer integral evaluations and contractions than the full Hamiltonian. Benchmarks have shown that the scalar Hamiltonian captures 99.99% of the ground state Hartree-Fock energy with only 10% of the cost of the full Hamiltonian, making it a suitable zeroth-order Hamiltonian for state interaction.[35,103] Unlike the traditional state interaction approach, the zeroth-order Hamiltonian does not necessarily have to be entirely scalar. The nuclear-electronic potential, Coulomb, Gaunt, and Gauge terms are all partitioned into scalar and vector relativistic parts. A choice can be made to include any of these vector relativistic terms in the zeroth-order Hamiltonian.[94]

Given a choice of a zeroth-order Hamiltonian, the perturbing Hamiltonian is written as

$$H^1 = H_{DCB} - H^0 \tag{3.5}$$

Defining the perturbing Hamiltonian in this manner allows for an easier and more general implementation due to the different possibilities of zeroth-order Hamiltonians. Matrix elements

Table 3.4: Zeroth-Order Hamiltonian $\mathbf{H}^0$ studied in this work.

srDC(B)-	variational scalar-relativistic (sr) Dirac–Coulomb(–Breit)
srD*C(B)-	variational scalar-relativistic (sr) Dirac–Coulomb(–Breit) augmented with one-electron vector-relativistic contributions
srD*C*B-	variational scalar-relativistic (sr) Dirac–Coulomb–Breit augmented with one-electron and two-electron Coulomb vector-relativistic contributions

Table 3.5: Perturbations $\mathbf{H}^1$ studied in this work.

-vrDC(B)	perturbative vector-relativistic (vr) Dirac–Coulomb(–Breit)
-vrC(B)	perturbative vector-relativistic (vr) Coulomb(–Breit)
-vrB	perturbative vector-relativistic (vr) Breit

of the perturbing Hamiltonian in the interaction space is written as

$$H_{IJ}^1 = \sum_{pq} \gamma_{pq}^{IJ}(h_{pq} - h_{pq}^0) + \frac{1}{2}\sum_{pq} \Gamma_{pqrs}^{IJ}(g_{pqrs} - g_{pqrs}^0) \tag{3.6}$$

where h_{pq} and g_{pqrs} are the underlying one and two-electron matrix elements of the Dirac–Coulomb–Breit Hamiltonian, h_{pq} and g_{pqrs} are the underlying one and two-electron matrix elements of the zeroth-order Hamiltonian, and $\mathbf{\Gamma}$ is the two-particle transition density matrix.

Herein, we assess the accuracy of Dirac–Coulomb–Breit state interaction CASSCF starting from various zeroth-order Hamiltonians. We focus on ground state fine-structure splitting of late-row atoms. The no-pair approximation in the four-component CASSCF calculations is applied by ignoring positive-negative-energy orbital rotations.[81] A minimal active space encompassing only the valence subshell was used for atomic species. The calculation was state-averaged over the lowest non-relativistic term symbol. The maximum interaction space was used in each state interaction calculation.

The accuracy of the perturbative method is heavily dependent on the quality of the zeroth-order wave function. In this section, we explore various choices for zeroth-order

Table 3.6: Fine-structure splitting (in eV) for variational relativistic formalisms with CASSCF wave functions with corresponding mean unsigned error (MUE) and percent error (shown in parentheses) relative to experiment. See Tab. 3.4 for definition of Hamiltonians.

	srD*C	DC	srD*CB	srD*C*B	DCB	Expt.[63]
$\mathrm{Pd}^{+}\ {}^2\mathrm{D}_{5/2} \rightarrow {}^2\mathrm{D}_{3/2}$	0.588(33.4)	0.434(1.0)	0.588(33.4)	0.435(0.9)	0.419(4.6)	0.439
$\mathrm{Cd}^{3+}\ {}^2\mathrm{D}_{5/2} \rightarrow {}^2\mathrm{D}_{3/2}$	0.952(32.1)	0.722(0.2)	0.952(32.1)	0.722(0.2)	0.698(3.2)	0.721
$\mathrm{I}\ {}^2\mathrm{P}_{3/2} \rightarrow {}^2\mathrm{P}_{1/2}$	1.015(7.7)	0.963(2.2)	1.012(7.4)	0.960(1.9)	0.951(0.9)	0.943
$\mathrm{Xe}^{+}\ {}^2\mathrm{P}_{3/2} \rightarrow {}^2\mathrm{P}_{1/2}$	1.407(7.7)	1.336(2.3)	1.403(7.4)	1.332(2.0)	1.319(1.0)	1.306
$\mathrm{Tm}\ {}^2\mathrm{F}_{7/2} \rightarrow {}^2\mathrm{F}_{5/2}$	2.002(84.1)	1.117(2.7)	2.004(84.3)	1.118(2.8)	1.062(2.4)	1.087
$\mathrm{Yb}^{3+}\ {}^2\mathrm{F}_{7/2} \rightarrow {}^2\mathrm{F}_{5/2}$	2.296(81.3)	1.299(2.6)	2.298(81.4)	1.301(2.7)	1.238(2.2)	1.266
$\mathrm{Lu}^{4+}\ {}^2\mathrm{F}_{7/2} \rightarrow {}^2\mathrm{F}_{5/2}$	2.615(78.9)	1.501(2.6)	2.617(79.0)	1.503(2.8)	1.433(2.0)	1.462
$\mathrm{Pt}^{+}\ {}^2\mathrm{D}_{5/2} \rightarrow {}^2\mathrm{D}_{3/2}$	1.476(41.4)	1.218(16.7)	1.477(41.4)	1.219(16.8)	1.196(14.5)	1.044
$\mathrm{Hg}^{3+}\ {}^2\mathrm{D}_{5/2} \rightarrow {}^2\mathrm{D}_{3/2}$	2.283(17.4)	1.908(1.9)	2.284(17.5)	1.910(1.8)	1.875(3.6)	1.945
$\mathrm{Rn}^{+}\ {}^2\mathrm{P}_{3/2} \rightarrow {}^2\mathrm{P}_{1/2}$	4.108(7.3)	3.976(3.8)	4.086(6.7)	3.953(3.2)	3.938(2.8)	3.831
MUE	0.470	0.051	0.468	0.049	0.048	

Hamiltonians, as listed in Tab. 3.4, and perturbations, as listed in Table 3.5. To align with the original motivation of spin-separation, we develop an all scalar-relativistic zeroth-order Dirac–Coulomb–(Breit) Hamiltonian, srDC(B), which incorporates scalar-relativistic terms from both one and two-electron contributions. Additionally, we propose two new classes of zeroth-order Hamiltonians by augmenting the scalar-relativistic Hamiltonian with vector-relativistic contributions from one-electron and two-electron operators. Note that within the augmentation naming scheme srD*C*(B*) and DC(B) would be the same Hamiltonians. To evaluate the quality of these zeroth-order Hamiltonians, we compare the computed atomic ground-state fine-structure splitting with the variational formalisms they approximate, as shown in Tab. 3.6. Experimental atomic fine-structure data was obtained from the NIST Atomic Spectra Database.[63]

As expected, the most accurate calculation, meaning the calculation with the lowest MUE, in Table 3.6 is the DCB Hamiltonian. Omitting the Breit interaction only increases the MUE by 0.003 eV as shown by the DC results. When the zeroth-order Hamiltonian only contains one-electron vector relativity, namely the srD*C and srD*CB Hamiltonians, the fine-structure splitting shows an overestimation of 0.47 eV. This overestimation arises from

Table 3.7: Atomic fine-structure splitting (in eV) for perturbative Dirac–Coulomb-based relativistic formalisms with CASSCF$^{\pm}$ wave functions with the mean unsigned error (MUE) and percent error (shown in parentheses) relative to experiment. See Tabs. 3.4 and 3.5 for definition of Hamiltonians.

	srDC-CASSCF$^{\pm}$-vrDC	srD*C-CASSCF$^{\pm}$-vrC	DC-CASSCF$^{\pm}$	Expt.[63]
Pd^{+} ^{2}D$_{5/2} \rightarrow {}^{2}D_{3/2}$	0.447(1.9)	0.431(1.9)	0.434(1.0)	0.439
Cd^{3+} ^{2}D$_{5/2} \rightarrow {}^{2}D_{3/2}$	0.725(0.6)	0.715(0.7)	0.722(0.2)	0.721
I ^{2}P$_{3/2} \rightarrow {}^{2}P_{1/2}$	0.880(6.6)	0.962(2.0)	0.963(2.2)	0.943
Xe^{+} ^{2}P$_{3/2} \rightarrow {}^{2}P_{1/2}$	1.224(6.3)	1.335(2.2)	1.336(2.3)	1.306
Tm ^{2}F$_{7/2} \rightarrow {}^{2}F_{5/2}$	1.097(0.9)	1.041(4.3)	1.117(2.7)	1.087
Yb^{3+} ^{2}F$_{7/2} \rightarrow {}^{2}F_{5/2}$	1.281(1.1)	1.212(4.3)	1.299(2.6)	1.266
Lu^{4+} ^{2}F$_{7/2} \rightarrow {}^{2}F_{5/2}$	1.477(1.0)	1.402(4.1)	1.501(2.6)	1.462
Pt^{+} ^{2}D$_{5/2} \rightarrow {}^{2}D_{3/2}$	1.349(29.3)	1.197(14.6)	1.218(16.7)	1.044
Hg^{3+} ^{2}D$_{5/2} \rightarrow {}^{2}D_{3/2}$	2.038(4.8)	1.884(3.1)	1.908(1.9)	1.945
Rn^{+} ^{2}P$_{3/2} \rightarrow {}^{2}P_{1/2}$	3.424(10.6)	3.968(3.6)	3.976(3.8)	3.831
MUE	0.100	0.057	0.051	

the absence of two-electron spin–orbit coupling which counteracts one-electron spin–orbit coupling. Significant improvement to the zeroth-order energies can be achieved by including both one-electron spin–orbit coupling and two-electron vector relativity. The resulting srD*C*B Hamiltonian yields an error of only 0.001 eV compared to the full DCB Hamiltonian. Based on percentage errors, atoms and ions within a same block exhibit similar behavior. The one exception is in the $5d$-block where Pt^{+} shows a significantly larger percent error for DCB-CASSCF. This discrepancy is likely due to electron correlation as there exists close-lying s-orbitals omitted from the active space. While including vector relativity in the zeroth-order wave function enhances the quality of the zeroth-order wave function, it also significantly increases the computational cost. Now that the quality of the zeroth-order Hamiltonians are established, we investigate the efficacy of state interaction in recovering the remainder of the DC or DCB Hamiltonians starting at various zeroth-order Hamiltonians.

Table 3.7 shows the performance of state interaction in recovering DC results starting at srDC and srD*C. We find that srDC-CASSCF-vrDC has a significantly larger MUE compared to the fully variational DC-CASSCF. However, when one–electron vector relativity

Table 3.8: Fine-structure splitting (in eV) for perturbative Dirac–Coulomb–Breit-based relativistic formalisms with CASSCF wave functions with corresponding mean unsigned error (MUE) and percent error (shown in parentheses) relative to experiment. The top row denotes the zeroth-order Hamiltonian and the row below denotes the remaining vector-relativistic terms that are included perturbatively. See Tabs. 3.4 and 3.5 for definition of Hamiltonians.

	srDCB	srD*CB	srD*C*B	DCB-CASSCF$^{\pm}$	Expt.[63]
	vrDCB	vrCB	vrB		
Pd^{+} $^2\mathrm{D}_{5/2} \rightarrow {}^2\mathrm{D}_{3/2}$	0.432(1.5)	0.416(5.2)	0.420(4.3)	0.419(4.6)	0.439
Cd^{3+} $^2\mathrm{D}_{5/2} \rightarrow {}^2\mathrm{D}_{3/2}$	0.703(2.5)	0.693(3.8)	0.700(2.9)	0.698(3.2)	0.721
I $^2\mathrm{P}_{3/2} \rightarrow {}^2\mathrm{P}_{1/2}$	0.869(7.8)	0.950(0.7)	0.951(0.9)	0.951(0.9)	0.943
Xe^{+} $^2\mathrm{P}_{3/2} \rightarrow {}^2\mathrm{P}_{1/2}$	1.209(7.5)	1.319(1.0)	1.320(1.1)	1.319(1.0)	1.306
Tm $^2\mathrm{F}_{7/2} \rightarrow {}^2\mathrm{F}_{5/2}$	1.053(3.2)	0.995(8.5)	1.071(1.5)	1.062(2.4)	1.087
Yb^{3+} $^2\mathrm{F}_{7/2} \rightarrow {}^2\mathrm{F}_{5/2}$	1.230(2.9)	1.161(8.3)	1.250(1.3)	1.238(2.2)	1.266
Lu^{4+} $^2\mathrm{F}_{7/2} \rightarrow {}^2\mathrm{F}_{5/2}$	1.421(2.8)	1.346(7.9)	1.446(1.1)	1.433(2.0)	1.462
Pt^{+} $^2\mathrm{D}_{5/2} \rightarrow {}^2\mathrm{D}_{3/2}$	1.323(26.8)	1.174(12.5)	1.196(14.5)	1.196(14.5)	1.044
Hg^{3+} $^2\mathrm{D}_{5/2} \rightarrow {}^2\mathrm{D}_{3/2}$	1.999(2.8)	1.850(4.9)	1.876(3.6)	1.875(3.6)	1.945
Rn^{+} $^2\mathrm{P}_{3/2} \rightarrow {}^2\mathrm{P}_{1/2}$	3.385(11.6)	3.930(2.6)	3.938(2.8)	3.938(2.8)	3.831
MUE	0.109	0.071	0.044	0.048	

is included in the zeroth-order Hamiltonian, the error notably reduced to levels akin to DC-CASSCF.

Table 3.8 shows the performance of state interaction in recovering DC results starting at srDCB, srD*CB, and srD*C*B. State interaction calculations using srDCB yields the largest error. By including one-electron spin–orbit coupling in the zeroth-order Hamiltonian, the MUE reduces from 0.109 to 0.071 eV. After moving to srD*C*B, the MUE only differs from the fully variational srDCB MUE by 0.004 eV. The large errors starting from the all-scalar-relativistic zeroth-order Hamiltonian suggests that it may not be the best starting point for state interaction.

3.2 State Interaction in Linear Response TDDFT

LR-TDDFT has been the modern day workhorse for computational photochemistry, thanks to the balance between its predictive power and low computational scaling with respect to system size. Although very efficient, a fully variational relativistic treatment of large molecules remains immensely expensive. State interaction can be applied to LR-TDDFT to attain the same cost-saving advantages as in configuration interaction.[89,90] State interaction is naturally suitable for wave function based methods since the zeroth-order Hamiltonian eigenstates are explicitly solved, providing an orthonormal basis to construct the full Hamiltonian. LR-TDDFT does not solve for Hamiltonian eigenstates, but instead finds excitation energies by solving for eigenvalues of the orbital Hessian. Because the orbital Hessian is not Hermitian, the eigenvectors are not necessarily orthogonal. Moreover, the eigenvectors are not wave function, but are excitation and de-excitation amplitudes. However, under the Tamm-Dancoff approximation, the orbital Hessian reduces to the CIS Hamiltonian, where the excitation amplitudes correspond to coefficients of a CIS wave function. Without the Tamm-Dancoff approximation, CIS-like wave function can be approximated using the Casida *ansatz*.

3.2.1 Derivation of TDDFT-SO

Herein, state interaction is adapted for closed-shell LR-TDDFT, which we call TDDFT-SO, using the scalar relativistic DKH2 Hamiltonian as the zeroth-order Hamiltonian. The interaction space comprises of approximate CIS wave functions adapted from excitation and de-excitation amplitudes,

$$|I_{S,M_S}\rangle = \frac{1}{|\mathbf{Z}_I|}\sum_{ia} Z_{ia,I}|\Phi_i^a\rangle_{S,M_S} \tag{3.7}$$

$$\mathbf{Z} = \mathbf{X} + \mathbf{Y} \tag{3.8}$$

where I is the index of the excited state, i indexes over occupied orbitals, a indexes over virtual orbitals, and $|\Phi_i^a\rangle_{S,M_S}$ is a configuration state function (CSF) where an electron from orbital i is excited to orbital a. Closed-shell LR-TDDFT is only able to capture singlet and triplet excited states with $M_S = 0$. Excitation amplitudes for triplet $M_S = \pm 1$ states are assumed to be equal to the triplet $M_S = 0$ state. Excited CSFs can be written in terms of creation and annihilation operators acting on the ground state determinant.

$$\text{Singlet}, S = 0, M_S = 0 : |\Phi_i^a\rangle_{0,0} = \frac{1}{\sqrt{2}}(a^\dagger_{a\alpha} a_{i\alpha} + a^\dagger_{a\beta} a_{i\beta})|0\rangle \tag{3.9}$$

$$\text{Triplet}, S = 1, M_S = -1 : |\Phi_i^a\rangle_{1,-1} = a^\dagger_{a\beta} a_{i\alpha}|0\rangle \tag{3.10}$$

$$\text{Triplet}, S = 1, M_S = 0 : |\Phi_i^a\rangle_{1,0} = \frac{1}{\sqrt{2}}(a^\dagger_{a\alpha} a_{i\alpha} - a^\dagger_{a\beta} a_{i\beta})|0\rangle \tag{3.11}$$

$$\text{Triplet}, S = 1, M_S = +1 : |\Phi_i^a\rangle_{1,+1} = -a^\dagger_{a\alpha} a_{i\beta}|0\rangle \tag{3.12}$$

The screened nuclear spin–orbit Breit-Pauli Hamiltonian is used as the perturbing Hamiltonian. The one-electron Breit–Pauli Hamiltonian can be decomposed into its Cartesian components and written in second quantized form.

$$\hat{H}_{BP} = \hat{H}^x_{BP} + \hat{H}^y_{BP} + \hat{H}^z_{BP} \tag{3.13}$$

$$\hat{H}^x_{BP} = \frac{1}{2}\sum_{pq} h^x_{pq}(a^\dagger_{p\alpha} a_{q\beta} + a^\dagger_{p\beta} a_{q\alpha}) \tag{3.14}$$

$$\hat{H}^y_{BP} = -\frac{i}{2}\sum_{pq} h^y_{pq}(a^\dagger_{p\alpha} a_{q\beta} - a^\dagger_{p\beta} a_{q\alpha}) \tag{3.15}$$

$$\hat{H}^z_{BP} = \frac{1}{2}\sum_{pq} h^z_{pq}(a^\dagger_{p\alpha} a_{q\alpha} - a^\dagger_{p\beta} a_{q\beta}) \tag{3.16}$$

$$h^k_{pq} = \langle p|\sum_{A} \frac{Z_A}{2c^2 r^3_{iA}} \hat{l}_k |q\rangle, k \in \{x, y, z\} \tag{3.17}$$

The screened nuclear spin–orbit approximation is applied by scaling $h^k_{\mu\nu}$ in the AO basis by an empirical factor,

$$h^k_{\mu\nu} \rightarrow \left(1 - \sqrt{\frac{Q(l_\mu)Q(l_\nu)}{Z_\mu Z_\nu}}\right) h^k_{\mu\nu} \tag{3.18}$$

where l_μ is the orbital angular momentum quantum number of AO μ. Analytical expressions for spin–orbit matrix elements in the interaction space can be derived using Wick's theorem.[7] These expressions are also written as tensor traces, allowing for efficient parallel computation.

$$\langle 0|\hat{H}_{BP}|J_{1,\pm1}\rangle = \mp\frac{1}{2|\mathbf{Z}_J|}\sum_{ia} Z_{ia,J}(h^x_{ia} \pm ih^y_{ia}) \tag{3.19}$$

$$\langle 0|\hat{H}_{BP}|J_{1,0}\rangle = \frac{1}{|\mathbf{Z}_J|\sqrt{2}}\sum_{ia} Z_{ia,J}h^z_{ia} \tag{3.20}$$

$$\langle 0|\hat{H}_{BP}|J_{0,0}\rangle = 0 \tag{3.21}$$

$$\langle I_{0,0}|\hat{H}_{BP}|J_{1,\pm1}\rangle = \frac{1}{2|\mathbf{Z}_I||\mathbf{Z}_J|\sqrt{2}}\left(\sum_{ija} Z_{ia,I}Z_{ja,J}(h^x_{ji} \pm ih^y_{ji}) - \sum_{iab} Z_{ia,I}Z_{ib,J}(h^x_{ab} \pm ih^y_{ab})\right) \tag{3.22}$$

$$\langle I_{0,0}|\hat{H}_{BP}|J_{1,0}\rangle = -\frac{1}{2|\mathbf{Z}_I||\mathbf{Z}_J|}\left(\sum_{ija} Z_{ia,I}Z_{ja,J}h^z_{ji} + \sum_{iab} Z_{ia,I}Z_{ib,J}h^z_{ab}\right) \tag{3.23}$$

$$\langle I_{1,0}|\hat{H}_{BP}|J_{1,\pm1}\rangle = \frac{1}{2|\mathbf{Z}_I||\mathbf{Z}_J|\sqrt{2}}\left(\sum_{ija} Z_{ia,I}Z_{ja,J}(h^x_{ji} \pm ih^y_{ji}) + \sum_{iab} Z_{ia,I}Z_{ib,J}(h^x_{ab} \pm ih^y_{ab})\right) \tag{3.24}$$

$$\langle I_{1,-1}|\hat{H}_{BP}|J_{1,1}\rangle = 0 \tag{3.25}$$

$$\langle I_{1,0}|\hat{H}_{BP}|J_{1,0}\rangle = 0 \tag{3.26}$$

$$\langle I_{1,\pm1}|\hat{H}_{BP}|J_{1,\pm1}\rangle = \pm\left(\frac{1}{2}\sum_{ija} Z_{ia,I}Z_{ja,J}h^z_{ji} + \frac{1}{2}\sum_{iab} Z_{ia,I}Z_{ib,J}h^z_{ab}\right) \tag{3.27}$$

The above expressions can also be used with the DKH or X2C spin–orbit operator as the perturbing Hamiltonian since these operators differ from the one-electron Breit–Pauli operator by a transformation.

$$\hat{h}^{X2C,k}_{\mu\nu} = \frac{i}{2c^2}\left(1 - \sqrt{\frac{Q(l_\mu)Q(l_\nu)}{Z_\mu Z_\nu}}\right)\langle\mu|\hat{R}\hat{X}^\dagger(\hat{p}V_{Ne}\times\hat{p})_k\hat{X}\hat{R}^\dagger|\nu\rangle \tag{3.28}$$

$$\hat{h}^{DKH,k}_{\mu\nu} = 2ic^2\left(1 - \sqrt{\frac{Q(l_\mu)Q(l_\nu)}{Z_\mu Z_\nu}}\right)\langle\mu|\hat{A}\hat{D}(\hat{p}V_{Ne}\times\hat{p})_k\hat{D}\hat{A}|\nu\rangle \tag{3.29}$$

3.2.2 Atomic Fine-Structure Splitting

The performance of TDDFT-SO was assessed for atomic cases. Fine structure splitting in the ^{3}P and ^{3}D excited state manifolds were calculated using TDDFT-SO[52] and plotted against variational X2C-TDDFT results.[104] Experimental atomic fine-structure data was obtained from the NIST Atomic Spectra Database.[63] The interaction space included the entire manifold of interest, including both singlet and triplet states. Additional states beyond the manifold of interest had negligible effect on atomic fine-structure splitting. For ^{1}S→ ^{3}P excitations, two types of electronic transitions are considered: $s^2 \rightarrow s^1p^1$ and $p^6 \rightarrow p^5s^1$, plotted in Figures 3.3 and 3.4. For the ^{1}S→ ^{3}D excitations, we also plot $s^2 \rightarrow s^1d^1$ and $d^{10} \rightarrow d^9s^1$ transitions in Figures 3.3 and 3.4.

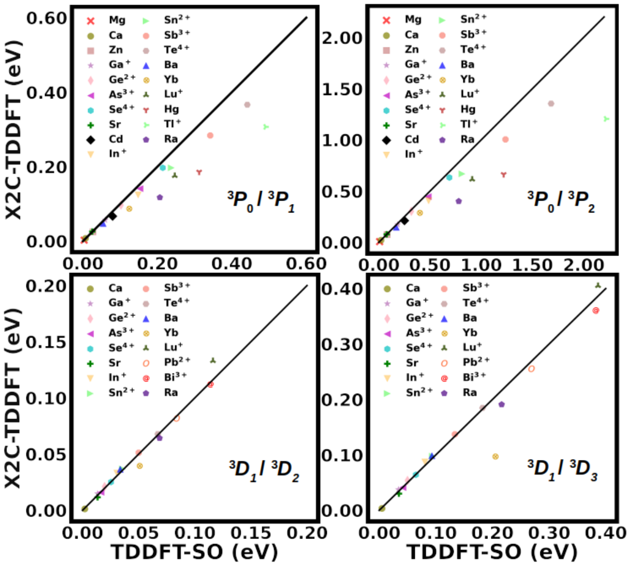

Figure 3.3: Comparison of excited state fine structure splitting calculated using TDDFT-SO and X2C-TDDFT for various atomic cases. ^{1}S → ^{3}P and ^{1}S → ^{3}D excitations arising from $s^2 \rightarrow s^1p^1$ and $s^2 \rightarrow s^1d^1$ transitions, respectively, are considered. Calculations were done using the ANO-RCC-VTZP basis set and the PBE0 functional.

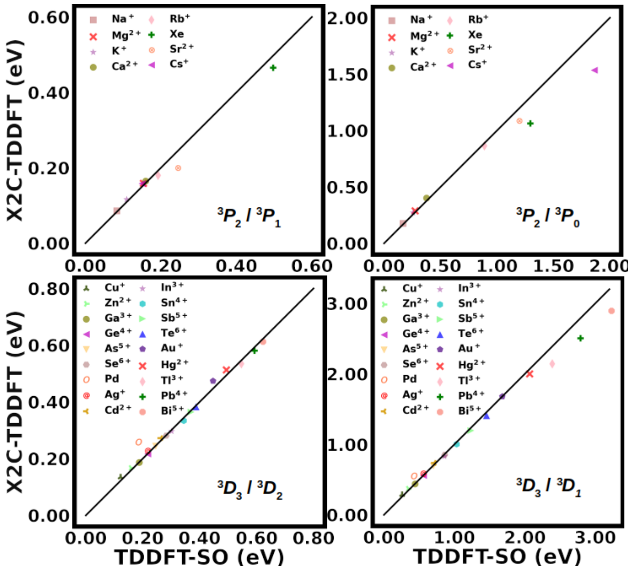

Figure 3.4: Comparison of excited state fine structure splitting calculated using TDDFT-SO and X2C-TDDFT for various atomic cases. ^{1}S $\rightarrow$ ^{3}P and ^{1}S $\rightarrow$ ^{3}D excitations arising from $p^6 \rightarrow p^5 s^1$ and $d^{10} \rightarrow d^9 s^1$ transitions, respectively, are considered. Calculations were done using the ANO-RCC-VDZ basis set and the PBE0 functional.

TDDFT-SO is in excellent agreement with X2C-TDDFT for light elements, but tends to overestimate fine-structure spitting as the atomic number increases. At $Z > 56$, the number of cases with an unsigned error greater than 0.10 eV drastically increased whereas for $Z \leq 56$, such errors are only seen for highly charged species close to $Z = 56$ (Sb^{3+},Te^{4+}). TDDFT-SO more accurately predicts ^{3}D fine-structure splitting than ^3P. The errors for ^{3}D stayed below 0.10 eV up to $Z > 80$. Exorbitant errors were observed for excitations involving 6p orbitals, with Tl$^+$ ^{3}P$_0$/^{3}P$_1$ and ^{3}P$_0$/^{3}P$_1$ splittings exhibiting errors of 60% and 84%, respectively. Large errors in fine-structure splitting involving the 6p shell have been observed in previous state interaction methods using the Breit–Pauli Hamiltonian.[67,89,105] One source for this error is the overestimation of the spin–orbit interaction close to the nucleus. This is reflected in the fact that the points mostly lie below the line of equality in Figures 3.3 and 3.4. It has been shown in previous work that applying the DKH transformation dampens this interaction and improves agreement with experiment.[54,105] Similar behavior is expected for the X2C transformation since it is equivalent to the infinite-order one-electron DKH transformation.

Even with DKH kinematic factors applied to the one-electron Briet–Pauli operator and a mean-field treatment of the two-electron Breit–Pauli operator, state interaction underestimates the Tl $6p$ fine-structure splitting by over 0.12 eV compared to experiment.[105] This arises from the different response of $p_{1/2}$ and $p_{3/2}$ orbitals to relativistic effects. With only scalar relativity, all six p orbitals expand. With both scalar and vector relativity, $p_{1/2}$ and $p_{3/2}$ exhibit very different radial distributions. Similar to $s_{1/2}$, $p_{1/2}$ exhibits a spherical density and a singularity at the nucleus, whereas $p_{3/2}$ more closely resembles non-relativistic p orbitals.[30,31] If not accounted for at the orbital level, a large interaction space is necessary to describe the stark difference between the fully relativistic p orbitals, contributing to the large errors seen for Tl and Tl^+.

3.2.3 Limitations of TDDFT-SO

In the presence of strong spin–orbit coupling, TDDFT-SO may not recover X2C-TDDFT results. TDDFT excitation amplitudes only map onto CIS wave functions, inherently limiting the interaction space. Higher-order excited determinants that may be necessary to describe strong spin–orbit effects are left out of the interaction space. This limitation is seen in the excited state splitting of PtCl_6^{2-}.

Figure 3.5 shows the MO and state energy diagrams of PtCl_6^{2-}. The energy difference between the non-relativistic t_{2g} and t_{1g} is 0.09 eV whereas the spin–orbit splitting of t_{2g} is 0.39 eV. This indicates that the strength of spin–orbit coupling is comparable to ligand field effects, sufficient to alter the orbital landscape of the system. Moreover, t_{1g} splits into a doubly-degenerate $e_{5/2,g}$ and quadruply-degenerate $f_{3/2,g}$, t_{2g} splits into a doubly-degenerate $e_{1/2,g}$ and quadruply-degenerate $f_{3/2,g}$, and e_g becomes $f_{3/2,g}$. In the absence of spin–orbit coupling, the Cl p (t_{1g}), Pt d (t_{2g}), and Pt d (e_g) transform as different irreps and therefore do not mix. Under spin–orbit coupling, both Cl p and Pt d orbitals spawn sets of $f_{3/2,g}$, allowing mixing between these orbitals. Moreover, there exists sets of lower-lying Cl p t_{1g}, t_{2g}, and e_g orbitals that spawn sets of $f_{3/2,g}$, introducing further mixing.

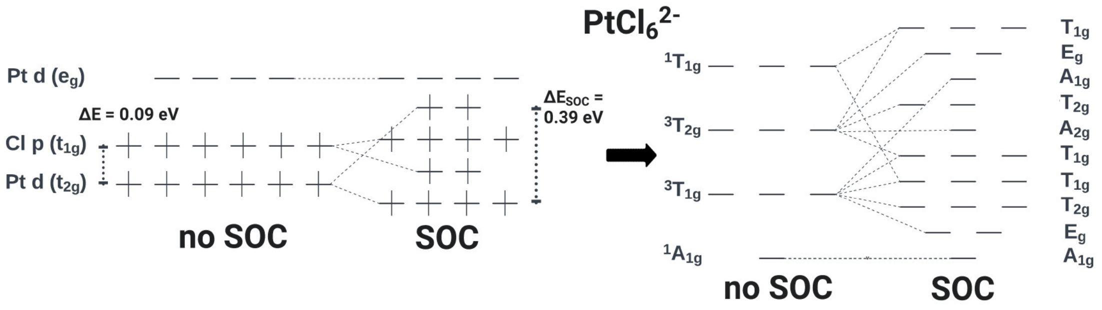

Figure 3.5: Left: Molecular orbital (MO) diagram of $\mathrm{PtCl_6^{2-}}$. Each level is a single spin–orbital, with electrons represented by vertical bars. The MO diagram without SOC was obtained from the restricted Kohn–Sham reference used in TDDFT-SO. The MO diagram with SOC was obtained from the X2C Kohn–Sham reference used in X2C-TDDFT. Right: X2C-TDDFT state diagram of $\mathrm{PtCl_6^{2-}}$. Each state is described by its irreducible representation in G × SU(2), where G is the spatial symmetry group of the molecule.

Table 3.9: Comparison between excitation energies of $\mathrm{PtCl_6^{2-}}$ calculated using X2C-TDDFT and TDDFT-SO with an interaction space of N singlet and N triplet spin-free states. Each state is described by its irreducible representation in $G \times SU(2)$, where G is the spatial symmetry group of the molecule. States with large singlet-triplet mixing is written as a direct sum of the singlet and triplet irreducible representations. Notation was adopted from Altmann and Herzig. The ordering of highlighted states are incorrectly predicted by TDDFT-SO.

State	**TDDFT-SO**							**X2C-TDDFT**
	$N = 6$	$N = 10$	$N = 15$	$N = 20$	$N = 60$	$N = 100$	$N = 200$	
E$_g$	1.8010	1.7851	1.7835	1.7835	1.7624	1.7624	1.7617	1.8648
T$_{2g}$	1.8697	1.8584	1.8573	1.8574	1.8334	1.8334	1.8329	1.9492
T$_{1g}$	1.9167	1.9015	1.9006	1.9006	1.8780	1.8780	1.8775	1.9691
T$_{1g}$	2.3104	2.3096	2.3082	2.3082	2.2640	2.2640	2.2634	2.3607
A$_{2g}$	2.3867	2.3542	2.3590	2.3590	2.3358	2.3358	2.3351	2.3646
T$_{2g}$	2.3727	2.3565	2.3572	2.3573	2.3261	2.3261	2.3255	2.4046
A$_{1g}$	2.5220	2.5131	2.4966	2.4966	2.4630	2.4427	2.4404	2.4051
E$_g$	2.3552	2.3578	2.3513	2.3513	2.3180	2.3180	2.3173	2.4121
T$_{1g}$	2.5832	2.5630	2.5627	2.5627	2.5232	2.5232	2.5224	2.5824

As discussed in the case of Tl, spin–orbit coupling that results in large changes to the orbital landscape is difficult to capture at the state interaction level. Capturing these effects within the restricted interaction space provided by TDDFT may be impossible as higher-order excited determinants may be needed. For state interaction to capture the spin–orbit splitting of the $d-d$ excited states, the interaction space must include excitations involving Cl p to capture the mixing between Cl p and Pt d introduced by spin–orbit coupling. The excitation energies of the spin–orbit states computed using X2C-TDDFT and TDDFT-SO at various interaction spaces are shown in Table 3.9. The N-sized interaction space contains the ground state, the lowest N singlet states, and the lowest N triplet manifolds, resulting in an interaction space of $4N+1$ states. At $N = 60$, the interaction space have covered most of the valence excitations involving Cl p, which are expected to strongly couple to the $d-d$ excited states. Beyond $N = 60$, the $d-d$ excitation energies have more-or-less converged, with small changes from weakly-coupled high-lying excited states. Even at $N = 200$, TDDFT-SO did not reproduce the excited state ordering computed by X2C-TDDFT. Reproducing X2C-TDDFT results may require an unmanageably large interaction space or higher-order excited determinants that are not offered by TDDFT.

3.2.4 Relation to LS and jj-Coupling

The fully variational treatment of spin–orbit coupling is equivalent to jj-coupling. Optimizing MOs in the presence of spin–orbit coupling implicitly couples spin and orbital angular momenta into total angular momentum at the MO level. Performing CI with Slater determinants constructed from these MOs yields N-electron wave functions with the total angular momentum of individual electrons coupled. In this Thesis, the fully variational approach to spin–orbit coupling will be referred to as jj-coupling.

Assuming that the zeroth-order Hamiltonian does not include spin–orbit coupling, spin and orbital angular momenta are not coupled at the MO level in state interaction. Solving for N-electron wave functions using Slater determinants constructed from these orbitals yields spin-diabatic states with spin and orbital angular momenta coupled across individual electrons independently. After obtaining a basis of spin-diabatic N-electron states, spin–orbit coupling is added to the Hamiltonian and reconstructed in this basis. The presence of spin–orbit coupling couples spin and orbital angular momenta of the spin-diabatic states to yield spin–orbit adiabatic states. State interaction strongly parallels LS-coupling. However, diagonalization of the spin–orbit-included Hamiltonian mixes zeroth-order states of different spins and non-relativistic irreps as long as the states share the same double group irrep. This takes state interaction beyond the LS-coupling scheme, making state interaction equivalent to jj-coupling scheme at the full CI and interaction space limit.

Whether or not the MOs are optimized with spin–orbit coupling, as long as the underlying AOs are the same, the orbital and N-electron basis spans the same Hilbert space. Because the Hamiltonian at the state interaction step is the same as the Hamiltonian in the fully variational approach, both approaches should yield the same results at the full CI and interaction space limit. The introduction of an active space will likely lead to mismatching Hilbert subspaces between the two approaches, yielding different results. Furthermore, the selection of an interaction space further differentiates the Hilbert subspaces. For weak spin–orbit coupling, especially at the LS-coupling limit where coupling within degenerate spin manifolds dominate, state interaction is extremely efficient. In the limit of strong spin–orbit coupling, the fully relativistic wave function may drastically deviate from the non-relativistic or scalar relativistic wave function. Although state interaction is able to handle these systems, it may be best to approach these systems via jj-coupling. Such systems may require a large active space and interaction space, encompassing various spin manifolds and symmetries, to capture the large changes to the wave function due to spin–orbit coupling.

Chapter 4

SPIN–ORBIT COUPLING IN CHEMISTRY

It is no exaggeration to say that spin–orbit coupling is a cornerstone of modern chemistry and is the most prominent vector relativistic effect. Spin–orbit coupling is commonly associated with one-electron spin–orbit coupling as it is the strongest vector relativistic effect. The much weaker two-electron spin–orbit coupling is essential to accurately describe spin–orbit effects. Spin–orbit effects are overestimated in the absence of two-electron contributions, reaching errors of up to ~ 1 eV for $4f$ fine-structure splitting in late lanthanides.[95] Though spin–orbit coupling grows with atomic number, some of its effects have dire consequences throughout the periodic table and have been exploited in applications throughout the chemical sciences.[48,51,106–109] Spin–spin and orbit–orbit couplings are nearly inconsequential for most chemical applications, mainly playing a role in nuclear magnetic resonance,[110] electron paramagnetic resonance,[111] and chemistry involving actinides and superheavy elements.[112]

4.1 Fine-Structure Splitting of Superatomic Orbitals

The $Au_{25}(SR)_{18}$ nanocluster is the flagship of atomically precise nanochemistry.[113] Over one thousand papers have been published about it and its derivatives since its identification in 2005[114] and structure determination in 2008.[113,115–119] However, the influence of spin–orbit coupling over different oxidation states has not been fully understood, despite being the most studied cluster in the field and recent attempts.[120–123]

Figure 4.1 shows the experimental UV-vis absorption spectra of $Au_{25}(SR)_{18}$ nanoclusters (abbreviated Au_{25}) at three different oxidation states. The differences among them can clearly be seen. The low energy region from 1.2 eV to 2.0 eV, known as the fingerprint band, correspond mainly to transitions between frontier orbitals. Upon oxidations, the

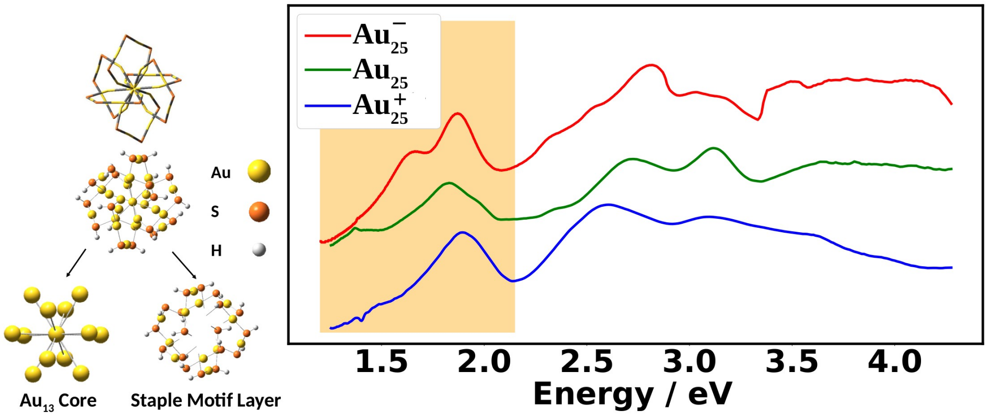

Figure 4.1: On the left, ball-and-stick and wire frame models of $Au_{25}(SR)_{18}$ are shown. The nanocluster can be separated into two regions: the Au_{13} core and the staple motif layer. In our computational model, we use R = H to reduce computational cost. On the right, the experimental UV-vis absorption spectra of $Au_{25}(SPET)_{18}$ (SPET = 2-phenylethanethiolate: SCH_2CH_2Ph) at the −1, 0, and +1 charge states recorded at 78 K is shown. The shaded region is the "fingerprint" band, which is the focus of this work.

double peak in the anion changes to an asymmetric band in the neutral species with further blue-shifts in the cation.[124–127] The frontier orbitals are well-understood in the absence of spin–orbit coupling by the superatomic complex model: Au_{25}^{-} being an 8-electron system with a superatomic electron configuration of $(1S)^2(1P)^6$, with the $1D$ orbitals being the LUMO.[128] Although the double peaks of Au_{25}^{-} were explained by the fine-structure splitting of the $1P$ orbital, the role of SOC in the neutral and cationic spectra remains unexplored.[120]

Another consideration is the interplay between geometry and electronic structure as a result of spin–orbit coupling. Jahn-Teller distortion plays a crucial role in the electronic structure of metal nanoclusters.[127,129,130] It is well-known that filling degeneratre or near-degenerate orbitals with unpaired electrons is met by geometric distortion that lower the nanocluster symmetry and break orbital degeneracies. Metal nanoclusters tend to not follow Hund's rule since the energy lowered by Jahn-Teller distortion can be greater than that by avoiding Coulombic repulsion from electrons in the same spatial orbital. This perspective is paramount to understanding the UV-vis fingerprint band with respect to charge. As the

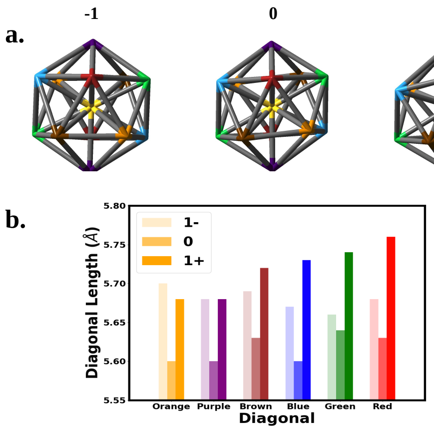

Figure 4.2: The structure of the Au_{13} core at the -1, 0, and $+1$ oxidation states are shown above. The vertices represent Au atoms. Atoms of the same color share a diagonal that runs through the center. The diagonal lengths are plotted for each oxidation state in the bottom chart.

nanocluster oxidizes from anionic (-1), neutral (0), and cationic ($+1$) states, the superatomic orbital electron configuration changes from $1P^6$ to $1P^5$ and $1P^4$, respectively, presenting a clear opportunity for Jahn–Teller distortion to act. Indeed, the Jahn–Teller effects have been shown to be present in Au_{25} which can be further manipulated to tune its redox properties.[127,131]

$Au_{25}(SH)_{18}$ was used as a model to reduce computational cost since it has been shown that optical properties in this energy region are insensitive to ligand choice.[124,132,133] All calculations were performed using a developmental version of the Gaussian electronic structure software package.[134] Two-component TDDFT calculations were performed using the PBE0 functional[135,136] with the relativistic CRENBL effective core potential with spin–orbit coupling and its complementary basis set for Au and S atoms.[3,137–140] For computational detail, see the Supporting Information in the original work.

4.1.1 Geometry of Au_{25}

We next correlate the change in the optical absorption spectra to the change in the geometry of the Au_{25} nanocluster as the charge is varied, with a focus on the electronic structure under spin–orbit coupling. We note that Jahn-Teller distortion in the Au_{25} nanoclusters has been correlated to experimental optical absorption and voltammograms.[127,130,141] Figure 4.2 shows the change in the nanocluster Au_{13} core geometry and diagonal lengths for each oxidation state. The anion core was nearly a perfect iscodahedron. The slight imperfections left the core with a T_h symmetry rather than the I_h symmetry expected of a perfect icosahedron. Oxidation of the anion to the neutral nanocluster resulted in a distortion of the core, lowering its symmetry to C_i. The distortion appeared as a tilting of the 10 equatorial triangular faces of the icosahedron caused by the increase in bond angles between the purple, blue, and orange diagonals. In addition, every diagonal decreased in length, leading to an overall shrinking of the core. Much greater distortion was observed when oxidized to the cation. The symmetry of the cation core remained C_i but the geometry further deviated from an icosahedron. The equatorial tilting of the icosahedron became much more pronounced as the bond angles between the purple, blue, and orange diagonals further increased. The length of each diagonal also increased with most diagonals surpassing their anionic lengths.

4.1.2 Superatomic Orbitals of Au_{25}

One of the most widely used models in studying the electronic structure of metal clusters treats the valence electrons as a jellium under a spherical potential.[142–144] Similar to the spherical nuclear–electronic potential of an atom, the spherical jellium model also gives rise to one-particle spherical harmonic solutions described by a principal quantum number (n), an orbital angular momentum quantum number (l), and an azimuthal quantum number (m_l).[128,143,145] These one-particle states share the same quantum numbers as atomic orbitals, earning the name superatomic orbitals and designating these clusters as superatoms. One difference is that the superatomic orbitals do not restrict the orbital angular momentum

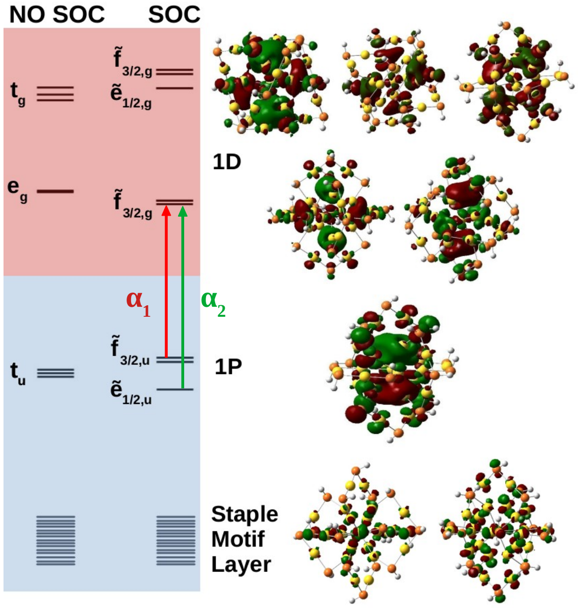

Figure 4.3: MO diagram of $Au_{25}(SH)_{18}^{-}$ with and without spin–orbit coupling, where each line is a Kramers pair. Blue and red shaded orbitals denote occupied and unoccupied orbitals, respectively. Below the superorbitals exists a high density of states region where electron density delocalized onto the staple motif layer. Images of the orbitals are shown on the right.

based on the principal quantum number ($l < n$). The fact that superatomic orbitals possess orbital angular momentum indicate that spin–orbit coupling may affect superatomic orbitals.

Recent advances in computing capabilities allow for more accurate approaches to study superatoms. *Ab initio* LCAO approaches align with the jellium model, agreeing that superatomic orbitals emerge from delocalized valence electrons.[108,120,146,147] One aspect that LCAO provides, that the jellium model does not, is the splitting of superatomic orbitals based on the symmetry of the superatom, similar to the ligand field splitting of atomic orbitals. Moreover, the LCAO approach explicitly treats every atom in the superatom, enabling interactions between superatomic orbitals with core electrons and the ligands.

Figure 4.3 shows the anionic MO diagram calculated with and without spin–orbit coupling along with visualization of the superatomic orbitals. The HOMO and LUMO are the $1P$ and $1D$, respectively. The $1P$ orbitals generally have the same appearance but lie on different

Superorbital	s	p	d
$1P_1$	25.64%	39.86%	34.50%
$1P_2$	24.17%	39.28%	36.55%
$1P_3$	22.92%	38.55%	38.55%
$1D_1$	41.50%	37.92%	20.56%
$1D_2$	40.87%	37.87%	21.25%
$1D_3$	40.22%	34.48%	25.30%
$1D_4$	39.44%	33.14%	27.42%
$1D_5$	40.36%	32.26%	27.38%

Table 4.1: Atomic orbital character of $Au_{25}(SC_6H_{13})_{18}^-$ superorbitals from calculation with SOC. Orbitals are arranged down the table with increasing energy.

axes. The $1D$ superatomic orbitals were more diverse in appearance including having a d_{z^2} or "four-leaf clover" center. The anion superatomic orbitals split in the same manner as atomic orbitals in a T_h ligand field as shown in Figure 4.3. Without spin–orbit coupling, the $1D$ splits into t_g and e_g while the $1P$ remains degenerate as t_{1u}.

Mulliken analysis of the superatomic orbitals in Table 4.1 shows that their atomic orbital composition is diverse in orbital angular momentum. Because the superatomic orbitals consist of p and d atomic orbitals, it is reasonable to expect that superatomic orbitals experience the influence of spin–orbit coupling from the atomic orbital level. With spin–orbit coupling, the t_g manifold splits into a doubly-degenerate $\tilde{e}_{1/2,g}$ and a quadruply-degenerate $\tilde{f}_{3/2,g}$ while the e_g manifold remains as a four-fold degeneracy, re-designating to the double group irrep $\tilde{f}_{3/2,g}$. The t_{1u} manifold splits into a quadruply-degenerate $\tilde{f}_{3/2,u}$ and a doubly-degenerate $\tilde{e}_{1/2,u}$. The relativistic field splitting was consistent with the predictions of double group theory, similar to atomic orbitals in a T_h ligand field under spin–orbit coupling. Below the $1P$ is a dense region with orbital delocalized across the staple motif layer. It was observed that these orbitals do play a key role in the neutral and cationic fingerprint band.

The MO diagram of the neutral and cationic clusters with spin–orbit coupling are shown in Figure 4.4. The orbital landscape marginally changed under spin–orbit coupling. Under

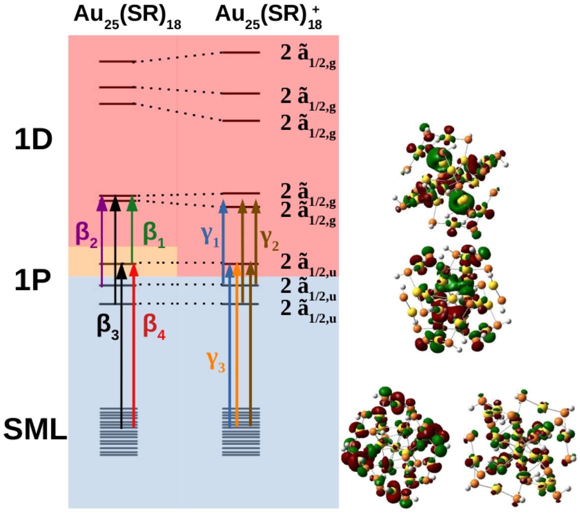

Figure 4.4: MO diagram depicting the Jahn-Teller distortion from the neutral $\mathrm{Au}_{25}(\mathrm{SR})_{18}$ to $\mathrm{Au}_{25}(\mathrm{SR})_{18}^{+}$ where each line is a Kramers pair. Orbital transitions responsible for features β_1, β_2, β_3, and β_4 on the neutral spectrum; and γ_1, γ_2, and γ_3 on the cationic spectrum, are shown. Blue, orange, and red shaded orbitals are doubly-occupied, singly-occupied, and unoccupied respectively. The double group irrep of the orbitals are shown on the right and are the same for both oxidation states. The “2” in front of the irrep indicates that the Kramers pair is a pair of spin-orbitals that transform as the given irrep (*e.g.*, $2\tilde{a}_{1/2,u}$ indicates that two spin-orbitals that transform as $\tilde{a}_{1/2,u}$ make up the Kramers pair).

the abelian C_i point group, orbital degeneracies only exist as Kramers pairs, leaving no manifolds for spin–orbit coupling to split. However, spin–orbit coupling did changes relative orbital energies slightly. The driver of Jahn-Teller distortion was the removal of electrons from the former $1P$ $\tilde{f}_{3/2,u}$ manifold that breaks the spherical symmetry of the $1P$ shell. The nanocluster symmetry for both oxidation states lowered to C_i to break the partially filled $\tilde{f}_{3/2,u}$ degeneracy. The neutral cluster experienced minor distortion since the destabilized $1P$ was still singly occupied. This is reflected in the reminiscence of the large energy gap between the former $1D$ $\tilde{f}_{3/2,g}$ and $\tilde{e}_{1/2,g}$ manifolds, resembling T_h orbital splitting. The distortion was much greater for the cation since the depopulated $1P$ can further destabilize without raising overall energy. The $1D$ further separate closing the large energy gap. In both oxidation states, the $1P$ degeneracy was broken.

4.1.3 Characterization of the Fingerprint Band

Figure 4.5 compares the simulated spectra with the experimental spectra for the three different oxidation states of Au_{25}. The low energy satellite peak at 1.64 eV was labeled as α_1 and the main peak at 1.91 eV was labeled as α_2 in Figure 4.5a for the anionic cluster. Upon oxidation of the anion to the neutral nanocluster, the satellite peak lowered in intensity and was red-shifted by 1.43 eV labeled as β_1 in Figure 4.5b. Broadening of the main peak was observed along with a slight red-shift to 1.82 eV, labeled as β_3 in Figure 4.5b. β_3 exhibited a low energy tail with significant intensity at 1.58 eV that connects β_1 and β_3, labeled as β_2 in Figure 4.5b. β_3 also exhibited a high energy shoulder, labeled at β_4. Further oxidation to the cationic state resulted in the disappearance of the low energy satellite peak along with a blue-shift of the main peak to 1.89 eV, labled as γ_2 in Figure 4.5c. The low-energy tail remains at 1.70 eV and is label γ_1 in Figure 4.5c. The high energy shoulder of the main peak is no longer present in the experimental spectrum but remains in the simulated spectrum. Overall, one can see and excellent agreement between the simulated and experimental spectra for the three different charge states.

Since the simulated spectra were computed using 2c-TDDFT with a spin–orbit-optimized

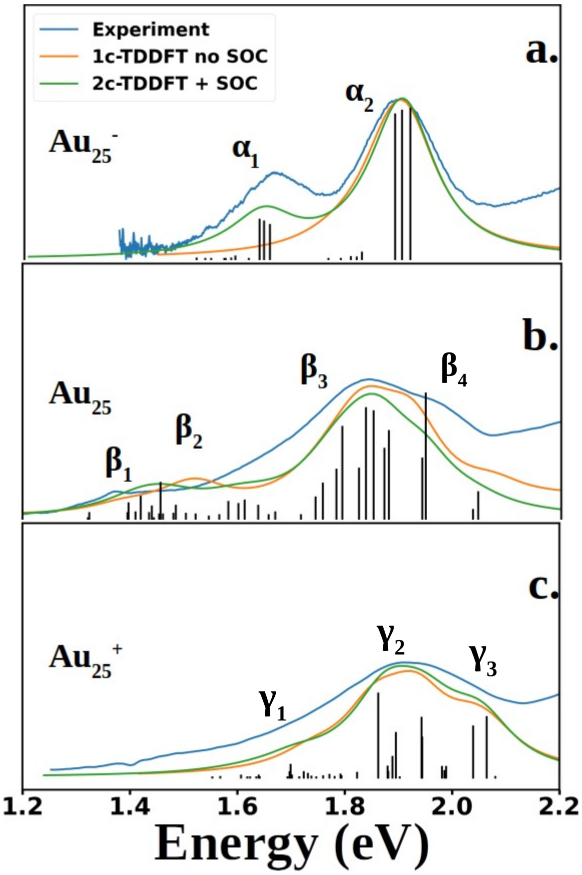

Figure 4.5: Experimental and computed spectra of $Au_{25}(SR)_{18}$. The excited states obtained from 2C-TDDFT are plotted as black lines. Spectra were generated by applying Lorentzian broadening to the excited states with a half-width at half max of 0.07 eV. The anion spectrum **(a)** is compared to the experimental spectrum of $Au_{25}(SCH_6H_{13})^-_{18}$ (SCH_6H_{13}: 1-hexanethiolate), reproduced from data obtained from Ramakrishna *et. al.*[1] The neutral **(b)** and cation **(c)** spectra are compared to experimental spectra of $Au_{25}(SR)_{18}$ and $Au_{25}(SR)^+_{18}$ respectively. All spectra were recorded at 78 K. The computed neutral spectrum was red-shifted by 0.11 eV to align with the experimental spectrum.

MO reference, spin–orbit coupling is viewed from the jj-coupling perspective. The most straightforward spectrum is the anion spectrum shown in Figure 4.5a. The anion spectrum consisted of two peaks, α_1 and α_2. The orbital excitations responsible for α_1 and α_2 are $1P$ $\tilde{\mathrm{e}}_{1/2,u} \rightarrow 1D$ $\tilde{\mathrm{f}}_{3/2,g}$ and $1P$ $\tilde{\mathrm{f}}_{3/2,u} \rightarrow 1D$ $\tilde{\mathrm{f}}_{3/2,g}$, respectively, as depicted in Figure 4.3.

Many more excited states were responsible for the neutral and cation spectrum than for the anion spectrum. Figure 4.4 shows which orbitals excitations are responsible for the spectral features labeled in Figure 4.5. The features β_1 and β_2 were direct consequences of Jahn-Teller distortion. Recall that Jahn-Teller distortion breaks the $\tilde{f}_{3/2,u}$ degeneracy into a stabilized doubly-occupied $1P$ and a destabilized singly-occupied $1P$. Orbital excitations from the destabilized singly-occupied $1P$ to the lowest two $1D$ gave rise to β_1. Orbital excitations from the stabilized doubly-occupied $1P$ to the lowest $1D$ gave rise to β_2. Along with excitations between superatomic orbitals, the vacancy in $1P$ opened opportunities for the low-energy orbitals delocalized onto the staple motif layer (SML) to excite into the core-localized $1P$, suggesting possible ligand-metal charge transfer (LMCT) in the fingerprint region. Mixing of these orbital excitations were pervasive in the excited states throughout the spectrum. Along with orbital excitations from the lowest $1P$ to the lowest $1D$, $SML \rightarrow 1P$ LMCT excitations also contribute to the excited states that form β_3. The rise of $SML \rightarrow 1P$ LMCT excitations with considerable oscillator strength also led to the broadening of β_3 and the rise of β_4. Because ligands in the theoretical model differ from experiment (R = SH as opposed to SPET), it is reasonable for the simulated spectrum to disagree with experiment at β_4.

With the depletion of the highest $1P$, β_1 was not present in the cation spectrum, resulting in a single broad peak labeled γ_2, and a low-energy tail, labeled γ_1. Excitations between the middle $1P$ and the two lowest $1D$ along with $SML \rightarrow 1P$ LMCT excitations were observed in γ_1. The high-intensity excited state at 1.82 eV that constitutes γ_2 also consists mainly of excitations between the middle $1P$ and the two lowest $1D$. The rest of the excited states that constitute γ_2 were from orbital excitations between the lowest $1P$ and the two lowest $1D$ along with $SML \rightarrow 1P$ LMCT excitations. The blue-shift of the main peak compared to

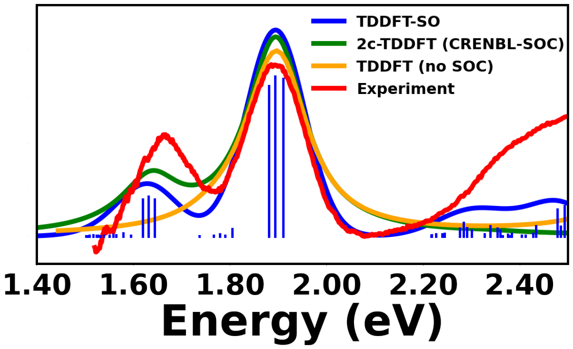

Figure 4.6: UV-Vis spectrum of $Au_{25}(SR)_{18}^{-}$. Computed spectra are shifted, broadened, and normalized to align with the large peak at 1.90 eV. Excited states from TDDFT-SO are indicated by blue sticks, where the height is scaled by the oscillator strength. The full-width half-max was set to 0.07 eV.

the neutral spectrum arose from the destabilization of the depleted $1P$. Such destabilization increased the energy of the excited states involving $SML \rightarrow 1P$ LMCT. The lack of high-intensity excited states at γ_3 due to a minimal ligand model caused the theoretical spectrum to exhibit a high-energy shoulder instead of a single broad peak encompassing both γ_2 and γ_3 as seen in experiment.

Consistent with the differences between orbitals with and without spin–orbit coupling, it is unsurprising that significant changes to the fingerprint band only occurs for the anion. The changes in relative orbital energies in the neutral and cation nanoclusters under spin–orbit coupling is reflecting by the small energy shifts of spectral features.

4.1.4 Fingerprint Band from the LS-Coupling Perspective

In the jj-coupling perspective, it is difficult to explain the difference between α_1 and α_2 intensities. From a density of states argument, α_2, coming from a four-fold degeneracy $\tilde{f}_{3/2,u}$, should have a higher intensity than α_1, which arises from a two-fold degeneracy $\tilde{e}_{1/2,u}$. However, this is not the case in experiment nor our calculations. The reason for this discrepancy can be easily seen from the LS-coupling picture.

To view the problem from the LS-coupling, the fingerprint band was computed using

TDDFT-SO. The TDDFT-SO calculation was performed using the scalar relativistic DKH2 and the Breit–Pauli spin–orbit Hamiltonian under the SNSO approximation. Figure 4.6 presents the TDDFT-SO-computed anion fingerprint band alongside the experimental spectrum and the simulated spectrum from Figure 4.5, demonstrating excellent agreement among all three spectra. In TDDFT-SO, the spin–orbit states are linear combinations of spin-pure states

$$|I'\rangle = \sum C_{I'K}|K\rangle \tag{4.1}$$

where I' is a spin–orbit state and K is a spin-pure state. The oscillator strength between two spin–orbit state can be computed as

$$f_{I'J'} = \frac{2}{3}\Delta\omega_{I'J'}|\langle I'|\mathbf{r}|J'\rangle|^2 \tag{4.2}$$

where $\omega_{I'J'}$ is the energy difference between spin–orbit state I' and J'. The oscillator strength is dependent on the transition dipole moment can be computed from transition dipole moments of spin-free states.

$$\langle I'|\mathbf{r}|J'\rangle = \sum_{KL} C^*_{I'K}C_{J'L}\langle K|\mathbf{r}|L\rangle \tag{4.3}$$

Transition dipole moments between spin-pure states are non-zero only if the states share the same spin. Ignoring the spatial wave function, oscillator strengths are stronger between states that share more spin character.

Both α_1 and α_2 excited states arise from the same orbital excitations in the non-relativistic picture. Table 4.2 shows that α_1 excited states had mostly triplet character and α_2 excited states had mostly singlet character. Given that the ground state is a singlet state, α_2 is more intense than α_1.

4.1.5 Conclusion

The relativistic LCAO approach provides much more insight than the spherical jellium model. The LCAO approach allows a more flexible and thorough description of superatoms. The

Peak	Excited State	% Triplet	% Singlet
α_1	1	74.91%	25.09%
	2	67.22%	32.78%
	3	76.65%	23.35%
α_2	1	34.03%	65.97%
	2	26.37%	73.63%
	3	37.74%	72.26%

Table 4.2: Percentage of triplet and singlet pure state contribution to excited states responsible for α_1 and α_2 in the anion spectrum. Excited states are labeled by increasing energy within a given peak.

explicit treatment of every atom elucidates the effects of molecular geometry on the superatom, showing that superatomic orbitals experience symmetry-driven splitting similar to ligand field splitting. Moreover, the explicit treatment of every atom shows that the superatomic structure of Au_{25} mostly lies on the Au_{13} core and revealed the presence of charge transfer excited states between the Au_{13} core and the staple motif layer in the neutral and cationic clusters. Without this, the neutral and cation fingerprint band could not be properly modeled as many features arise from excitations out of the staple motif layer to a superatomic orbital.

The relativistic aspect of this approach reveals that spin–orbit coupling affects superatomic orbitals similar to atomic orbitals. Superatomic orbitals arise from a linear combination of atomic orbitals with different angular momenta. Even though each orbital angular momentum experiences spin–orbit coupling differently on the atomic level, spin–orbit coupling splits superatomic orbitals based solely on the collective superorbital angular momentum and the superatomic symmetry. From the jj-coupling perspective, the presence of two peak in the anion fingerprint band can be seen as fine-structure splitting of the superatomic $1P$. However, only from the LS-coupling perspective can the intensity differences between α_1 and α_2 be explained. This perspective shows that the α_1 excited states are mostly triplet in character with optical activity granted from singlet mixing due to spin–orbit coupling, whereas the more intense α_2 excited states are mostly singlet in character.

4.2 Symmetry-Inhibited Intersystem Crossing in Organic Photosensitizers

Intersystem crossing is the non-radiative transition between electronic states with different spins. It is has been leveraged to facilitate a variety of chemical processes, including catalysis and photo-induced bond formation,[109,148–150] and also plays a key role in excited state relaxation processes.[65,151–155] One process involving intersystem crossing that has attracted significant attention is photo upconversion.[106,156–163] Photo upconversion is the process where a system absorbs two low-energy photons and emits a high-energy photon. A popular mechanism to achieve this is the triplet–triplet annihilation mechanism, which features a two-component system involving a photosensitizer and an emitter. This process begins with the photosensitizer absorbing a photon, exciting from a ground state singlet to an excited state singlet. The photosensitizer undergoes intersystem crossing to a triplet state, followed by a non-radiative energy and angular momentum transfer to a ground state emitter, exciting the emitter to an excited triplet state. Two excited triplet emitters undergo a triplet–triplet annihilation resulting in the relaxation of one emitter to a lower energy singlet and the excitation of the other emitter to a higher energy singlet. Finally, the high-energy singlet fluoresces at an energy greater than the absorbed photons.[106,156,157,161–163]

A particularly useful application of photo upconversion is the development of solar cells with the potential to exceed the Shockley–Queisser efficiency limit, or at the very least, move towards meeting this limit.[158,160,161,164] The shift towards preovskite-based solar cells have also made photon upconversion a more attractive approach to enhance efficiency. Many perovskite-based solar cells outperform silicon-based solar cells by more efficiently absorbing high energy near-UV–visible photons at the cost of being transparent in the near-infrared.[165] Much interest have been directed at developing systems that can upconvert near-infrared photons into the visible region for harvest.

Triplet–triplet annihilation photon upconversion relies on the ability of the photosensitizer to undergo fast and efficient intersystem crossing. Because spin–orbit coupling is stronger as

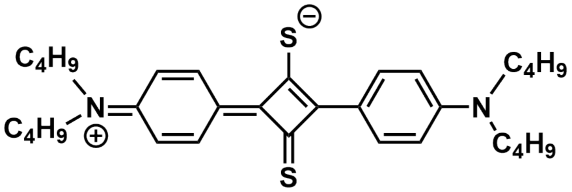

Figure 4.7: Structure of DBA-TSQ.

atomic number increases, the most efficient photosensitizers tend to be expensive late-row metal complexes.[106,166–169] The cost of using these metal complexes would be economically intractable if applied to large-area solar installations. Thus, chemists are beginning to seek low-cost organic alternatives. Attempts at harnessing the heavy-atom effect through halogenated organic dyes have been successful, but applications of these dyes have been limited due to poor photostability.[157,170] There has been some success in pushing organic molecules towards femtosecond intersystem crossing through thionation.[171–173] Recently, red-to-yellow photon upconversion has been achieved using dibutylaniline thiosquarine (DBA-TSQ) as the photosensitizer.[161]

DBA-TSQ functioned as an effective photosensitizer because it undergoes fast intersystem crossing with unity quantum yield.[161,171] Despite its seemingly rapid intersystem crossing, DBA-TSQ is relatively slow, undergoing picosecond intersystem crossing whereas molecules with a similar chemical composition can achieve it on the femtosecond timescale.[172–177] For instance, mono-deprotonated 2,4-dithiopurine has been reported to achieve femtosecond intersystem crossing with unity quantum yield.[173] Though sufficient for this application, studying its intersystem crossing mechanism could provide valuable insight in photosensitizers design.

4.2.1 Static Approximation of Intersystem Crossing

The inclusion of spin–orbit coupling presents a spin–orbit adiabatic picture where the N-electron wave function is no longer an eigenstate of the $\hat{S}^2$ operator. Because spin–orbit coupling is always present, electronic states are rarely spin-pure. When spin–orbit coupling is weak, electronic states remain nearly spin-pure and are often described as if they were. This is particularly true for light elements. In these situations, most chemical properties and processes can be captured without spin–orbit coupling. Regardless of how weak spin–orbit coupling may be, it cannot be neglected when studying intersystem crossings.[48,49,51,178] Without spin–orbit coupling, intersystem crossings are forbidden due to the orthogonality of the spin wave functions. The mixing of spin states introduced by spin–orbit coupling allows for intersystem crossings to occur.

In the spin-pure picture, the intersystem crossing rate constant between states I and J can be statically approximated by Fermi's golden rule with the spin–orbit operator as the perturbation.[49,51,178]

$$k_{ISC} = 2\pi|\langle I|\hat{H}_{SO}|J\rangle|^2\delta(E_J - E_I) \tag{4.4}$$

Since molecular states are discrete and non-radiative transitions must be isoenergetic, the density-of-states becomes a Dirac delta function. This description of intersystem crossing is widely used for organic molecules as they typically lack late-row elements to induce strong spin–orbit coupling. In the context of triplet–triplet annihilation photon upconversion, the photosensitizers typically undergo an intersystem crossing from a singlet state to a triplet state. Equation (4.4) can be rewritten to take into account the triply-degenerate triplet manifold,

$$k_{ISC} = 2\pi\delta(E_J - E_I)\sum_{M_S=-1}^{1}|\langle I, S=0|\hat{H}_{SO}|J, S=1, M_S\rangle|^2 = 2\pi|H_{SO}^{IJ}|^2\delta(E_J - E_I) \tag{4.5}$$

where the spin–orbit matrix elements between singlet and triplet microstates are condensed into $|H_{SO}^{IJ}|$. This quantity is typically referred to as the spin–orbit coupling matrix element, spin–orbit coupling constant, or simply the "spin–orbit coupling".

$$|H_{SO}^{IJ}| = \sqrt{\sum_{M_S=-1}^{1}|\langle I, S=0|\hat{H}_{SO}|J, S=1, M_S\rangle|^2} \tag{4.6}$$

The static approximation of the intersystem crossing rate evaluates Equation (4.6) at the equilibrium geometry of the outgoing state. The spin–orbit coupling at the equilibrium geometry is also referred to as direct spin–orbit coupling.

While the spin–orbit coupling matrix element provides a quantitative measure for predicting intersystem crossing rates, El-Sayed's rule serves as a qualitative tool for assessing whether the transition is allowed. El-Sayed's rule states that an intersystem crossing must be accompanied by a change in orbital character.[51,152,179,180] The change in spin angular momentum induces a torque onto the electron orbit ensuring the conservation of total angular momentum. The induced orbital torque results in an orbital transition via a spatial rotation.[181,182] An El-Sayed forbidden transition results in a zero or very small spin–orbit coupling matrix element.[183] However, even if an intersystem crossing is El-Sayed allowed, it may still be symmetry forbidden, or *vice versa*. In other words, although the intersystem crossing may conserve angular momentum, the orbital transition may not be possible under a spatial rotation.

According to previous work, DBA-TSQ exhibits no direct spin–orbit coupling between El-Sayed allowed singlet-triplet pairs.[171] As other molecules with similar chemical compositions exhibit direct spin–orbit couplings on the order of $10-100$ cm^{-1}, this absence may explain the slow intersystem crossing rate relative to similar molecules.[50,174,176] Yet, despite the absence of direct spin–orbit coupling, DBA-TSQ undergoes a highly efficient and somewhat rapid intersystem crossing. This raises the question: what is the underlying driving force behind the DBA-TSQ intersystem crossing?

To address this question, inspiration was drawn from porphine, where the $S_1 \rightarrow T_1$ intersystem crossing also occurs with no direct spin–orbit coupling.[51,183] In this case, the intersystem crossing was driven by spin–vibronic coupling. At the S_1 equilibrium geometry, $S_1 \rightarrow T_1$ is El-Sayed forbidden as both states have a $\pi\pi^*$ configuration. The intersystem crossing becomes El-Sayed allowed through a mixing of σ character into π orbitals driven by out-of-plane vibrations. Previous work has shown that applying out-of-plane distortions to DBA-TSQ increases the $S(n\pi^*) \rightarrow T(\pi\pi^*)$ spin–orbit coupling.[51,183,184] Distortion along an out-of-plane mode by $k_B T$ increases the spin–orbit coupling to merely 2.03 cm^{-1}, much lower than spin–orbit couplings for compounds of similar composition.[171] Though spin–vibronic coupling seems to promote intersystem crossing in DBA-TSQ, it undergoes a different mechanism than porphine as the DBA-TSQ singlet-triplet pair is already El-Sayed allowed. These discrepancies warrant further investigation into the spin–vibronic mechanism of DBA-TSQ.

Spin–vibronic contributions to spin–orbit coupling appear when the integral is Taylor expanded around the equilibrium geometry with respect to normal modes q_a.[51]

$$\begin{aligned}|\mathrm{H}_{SO}^{IJ}(\mathbf{q})| = \Bigg|\sum_{M_S}\Bigg(&\langle I_{0,0}|\hat{H}_{\mathrm{SO}}|J_{1,M_S}\rangle\Big|_{\mathbf{q}=0}\\ &+\sum_a \frac{\partial}{\partial q_a}\langle I_{0,0}|\hat{H}_{\mathrm{SO}}|J_{1,M_S}\rangle\Big|_{\mathbf{q}=0} q_a\\ &+\frac{1}{2}\sum_{ab}\frac{\partial^2}{\partial q_a \partial q_b}\langle I_{0,0}|\hat{H}_{\mathrm{SO}}|J_{1,M_S}\rangle\Big|_{\mathbf{q}=0} q_a q_b + \dots\Bigg)^2\Bigg|^{1/2}\end{aligned} \tag{4.7}$$

Notice that the zeroth-order term in Equation (4.7) is direct spin–orbit coupling.

4.2.2 Computational Details

All DFT calculations were performed using a developmental version of the Gaussian electronic structure software package.[185] The TPSSH functional[186,187] was used with the 6-311+G** basis set.[188–192] Dispersion correction was included using the Petersson-Frisch dispersion model.[193] A toluene solvation environment was simulated using a polarizable continuum model.[194] Ground state geometries were optimized using Kohn-Sham DFT. Excited state energies were computed using TDDFT. TDDFT was also used in optimizing excited state geometries. Spin–orbit coupling matrix elements were computed in the same manner as in TDDFT-SO.[52] Normal modes were computed at the same level of theory as above. The harmonic approximation was used to obtain ground state vibrational wave functions. Irreps are assigned with the x-axis defined as the horizontal axis, y-axis defined as the vertical axis, and the z-axis defined as the in-page axis, with respect to the orientation shown in

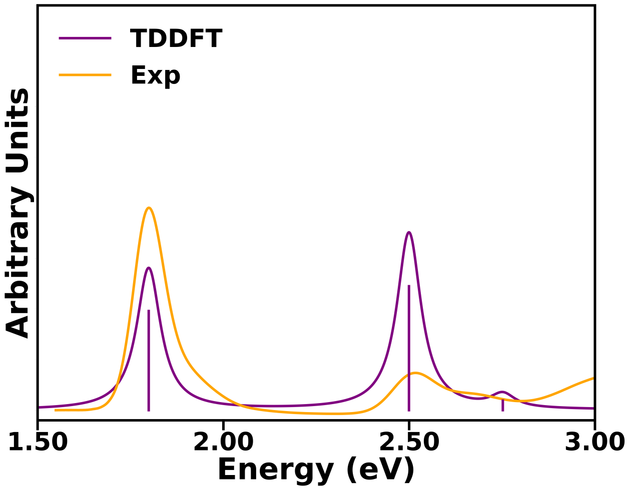

Figure 4.8: Simulated (purple) and experimental (orange) UV-vis spectrum of DBA-TSQ.

Figure 4.7.

4.2.3 Experimental Characterization of DBA-TSQ Intersystem Crossing

Figure 4.8 shows the experimental and TDDFT-simulated UV-vis spectrum of DBA-TSQ. The simulated spectrum was red-shifted by 0.17 eV to align spectral peaks. Despite this slight overestimation, the experimental and simulated spectra show excellent agreement. Photo-excitation to the lowest bright state is the gateway to upconversion. For DBA-TSQ, this is a singlet $\pi\pi^*$ excited state. Analogous to Kasha's rule, the molecule is expected to relax to the lowest singlet excited state before undergoing intersystem crossing. Though $S(\pi\pi^*)$ is the lowest bright singlet, TDDFT revealed a $S(n\pi^*)$ state lower in energy but dipole-forbidden from the $S(\pi^2)$ ground state. Depictions of these excited states as orbital excitations are shown in Figure 4.9. Although the Kohn-Sham orbitals show that the π-orbital is higher in energy than the non-bonding orbital, $S(n\pi^*)$ remains lower in energy due to reduced electron repulsion. TDDFT also revealed that triplet analogs of the $\pi\pi^*$ and $n\pi^*$ excited states are both energetically lower than $S(n\pi^*)$. This leaves two possible intersystem crossing processes to investigate: $S(n\pi^*) \rightarrow T(n\pi^*)$ and $S(n\pi^*) \rightarrow T(\pi\pi^*)$.

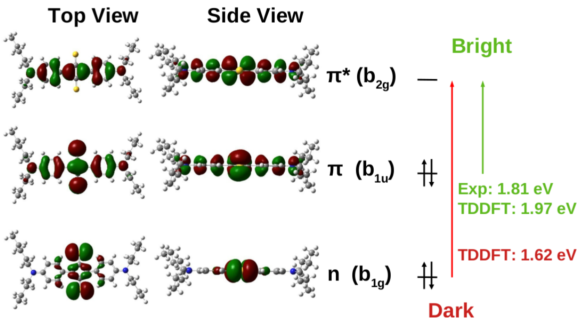

Figure 4.9: Frontier orbitals of DBA-TSQ. Orbitals excitations corresponding to the $\pi\pi^*$ and $n\pi*$ states are shown with green and red arrows, respectively. The $\pi\pi^*$ is bright while the $n\pi^*$ is dark. The TDDFT-computed excitation energy is 1.97 eV whereas the experimental excitation energy is 1.81 eV.

The intersystem crossing time constant was measured using femtosecond transient absorption (TA) spectroscopy pumped at 700 nm, near the $S(\pi\pi^*)$ excitation energy. Because previous reports noted near unity triplet yield,[171] the singlet lifetime can be approximated to be the intersystem crossing time constant, found through global analysis of the evolution of the TA spectrum shown in Figure 4.10a. The change in singlet and triplet populations is represented by the normalized ΔA of their respective spectral fingerprints. The raw kinetic trace associated with the singlet decay and triplet absorption are shown in Figure 4.10b. Notably, the kinetic trace associated with the singlet decay (blue) does not decay completely, and similarly the triplet (red) begins its frowth at a non-zero point. This is due to significant spectral overlap of the singlet and triplet excited state absorption signals. Kinetically resolving the evolution associated in Figure 4.10c using global analysis allows us to more clearly observe this overlap and recover the time constants associated with the intersystem crossing process. Briefly, global analysis deconvolutes the superposition of excited state absorption spectra as they evolve in time, yielding kinetically resolved TA features. The kinetic trace recovered via global analysis are shown in Figure 4.10d, revealing a singlet lifetime of 4.48 ps. This singlet decay rate is commensurate with the intersystem crossing time constant estimated from the triplet EAS growth time of 4.40 ps.

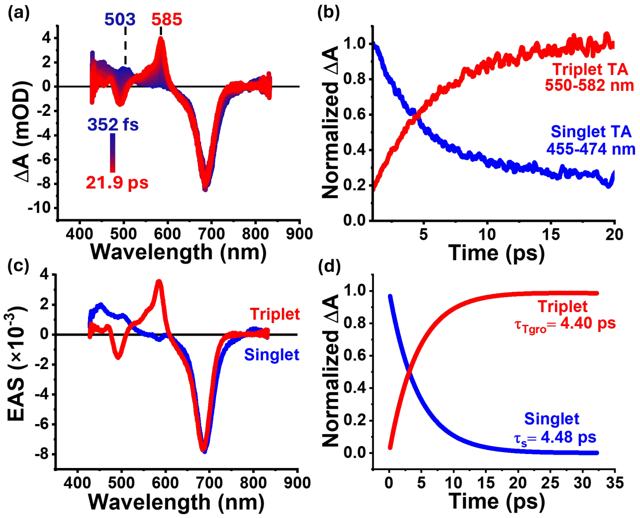

Figure 4.10: (a) Transient absorption (TA) spectra for DBA-TSQ in dearated toluene over 21.9 ps showing the singlet TA peak at 503 nm and the triplet TA peak at 585 nm. (b) Kinetic traces corresponding to the singlet decay (blue) and triplet growth (red) for DBA-TSQ. The singlet decay and triplet growth traces correspond to spectral values averaged over 455-474 nm and 550-582 nm, respectively, as indicated by the corresponding trace labels. Spectra were collected while exciting at 700 nm. (c) Evolution Associated Spectra (EAS) corresponding to the singlet ESA (blue) and triplet TA (right). (d) Kinetic traces fit via global analysis for the ESA singlet decay (blue) and triplet growth (red). The singlet lifetime was calculated to be 4.48 ps. The triplet generation time constant was calculated to be 4.40 ps.

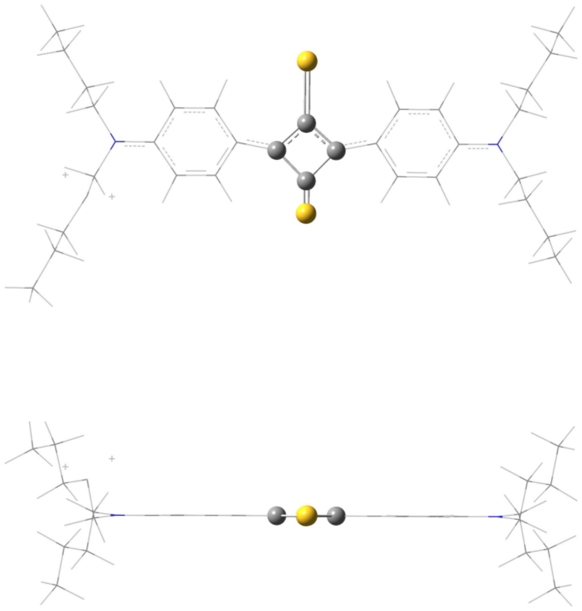

Figure 4.11: Antisymmetric b_{2u} C-S (q_{76}) stretching normal mode.

4.2.4 Theoretical Studying of DBA-TSQ Intersystem Crossing

Within the range of the zero-point vibration, the antisymmetric b_{2u} C-S stretching mode (q_{76}, Figure 4.11) has a strong effect on the magnitude of the spin–orbit coupling for $S(n\pi^*) \rightarrow T(\pi\pi^*)$, leading to a significant increase of the SOC matrix element from zero to 20.41 cm^{-1} at the classical turning point. We identify this as a spin–vibronic mechanism that arises from symmetry-perturbation. This mechanism contrasts with the spin–vibronic-enabled El-Sayed's rule previously observed in porphine.

Shown in Figure 4.12 is the computed spin–orbit coupling matrix element for $S(n\pi^*) \rightarrow T(\pi\pi^*)$ along the antisymmetric b_{2u} C-S stretching mode (q_{76}) with the zero-point energy and harmonic ground state vibrational wavefunction of $S(n\pi^*)$. Figure 4.12 shows that the spin–orbit coupling is linear along q_{76} near the equilibrium geometry, indicating that the linear spin–vibronic terms in Equation (4.7) dominate at small distortions. Figure 4.13 shows potential energy surfaces of low-lying excited states of DBA-TSQ along q_{76}. Using Equation (4.7), we show the effects of spin–vibronic coupling by calculating the intersystem

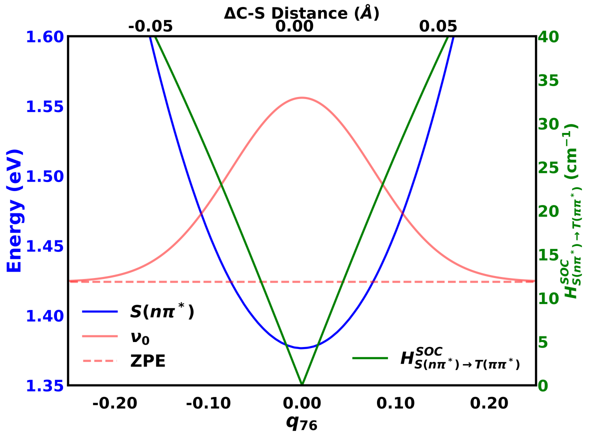

Figure 4.12: Plots of the spin–orbit coupling matrix element (green), the $S(n\pi^*)$ potential energy surface (blue), and the $S(n\pi^*)$ ground state vibrational wave function (red) along the antisymmetric b_{2u} C-S stretching mode q_{76}. The red dotted line is the zero point energy. The C-S displacement is shown on the top axis. The bottom plot corresponds to the spin–orbit coupling matrix element between singlet $n\pi^*$ and triplet $\pi\pi^*$.

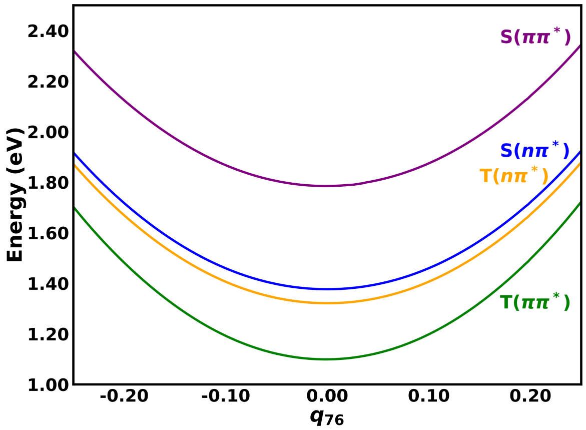

Figure 4.13: Potential energy surfaces of low-lying excited states of DBA-TSQ along the antisymmetric b_{2u} C-S stretching mode q_{76} starting at the $S(n\pi^*)$ equilibrium geometry.

time crossing time constant at some representative distortions along the normal mode. At the $S(n\pi^*)$ vibrational ground state root-mean-square distortion for each normal mode, the spin–orbit matrix element is 108.93 cm^{-1}, corresponding to an intersystem crossing time constant of 15.63 ps. Further from the origin at the classical turning point, the spin–orbit coupling matrix element is 154.06 cm^{-1}, corresponding to a time constant of 7.81 ps. This analysis is in close agreement to the experimental time constant of 4.48 ps.

An accurate approximation of the intersystem crossing time constant would evaluate the spin–orbit coupling at the singlet-triplet minimum energy crossing point (MECP).[195] However, the mode shown in Figure 4.12, along with all other normal modes, do not lead to a singlet–triplet crossing, nor to any significant decrease in the singlet-triplet energy gap up to $q_a = \pm 0.1$ Å. A minimum energy crossing point may be found further along low frequency modes or a linear combination of modes, however, such exploration of the potential energy surface is unfeasible for a molecule of this size. Moreover, an accurate calculation of the time constant would account for vibrational wave function overlap, which requires anharmonic considerations.

The calculations thus far indicate that spin–vibronic coupling can lead to a significant increase in spin–orbit coupling. To rigorously show whether the normal modes modulate spin–orbit coupling through the change in orbital angular momentum or through symmetry-perturbation, we conduct a symmetry analysis.

In the presence of spin–orbit coupling, it is appropriate to approach the problem from double group symmetry, where spin and spatial degrees of freedom are treated on equal footing.[30,48,68,73] As shown in Figure 4.9, the orbitals involved in ISC lie mostly on the planar region of DBA-TSQ. The butyl chains are neglected in the symmetry analysis since they do not participate in this intersystem crossing, leaving a local symmetry of D_{2h}. Based on Equation (4.6), a non-zero direct spin–orbit coupling requires that the direct product of the singlet state irrep, triplet state irrep, and the spin–orbit Hamiltonian irrep to consist of the totally symmetric irrep.

The spin–orbit Hamiltonian used in this study is the Breit–Pauli Hamiltonian under the screened-nuclear spin–orbit approximation. Because the screened-nuclear spin–orbit approximation scales the one-electron Breit–Pauli AO integrals based on orbital angular momentum, the symmetry of the Breit–Pauli Hamiltonian is preserved. Moreover, the Breit–Pauli Hamiltonian is totally symmetric.[48,196] Under D_{2h} symmetry, the spatial symmetry of $\pi\pi^*$ and $n\pi^*$ transforms as B_{3u} and B_{3g}, respectively. The spin symmetry of singlets and triplets transform as A_g and $B_{1g} \oplus B_{2g} \oplus B_{3g}$, respectively.[71] Note that spin symmetry is always *gerade*.[30,31,72] Whether direct spin–orbit coupling can be non-zero due to symmetry is determined by the following direct product:

$$\begin{aligned} & D_{2h} : \Gamma[S(n\pi^*) \rightarrow T(\pi\pi^*)] \\ & = B_{3g} \otimes A_g \otimes A_g \otimes B_{3u} \otimes (B_{1g} \oplus B_{2g} \oplus B_{3g}) \\ & = B_{1u} \oplus B_{2u} \oplus B_{3u} \end{aligned} \tag{4.8}$$

The one *ungerade* irrep causes the direct product to be entirely *ungerade*, corresponding to a zero direct spin–orbit coupling.

The first-order spin–vibronic term contains an extra differential operator with respect to q_a, which transforms as the same irrep as its corresponding normal mode $\Gamma(q_a)$. Including this irrep in the direct product leads to the totally symmetric irrep A_g only if $\Gamma(q_a) = b_{1u}, b_{2u}, b_{3u}$. The following direct product demonstrates that the antisymmetric C-S stretch, $\Gamma(q_{76}) = b_{2u}$, is spin-vibronically active.

$$\begin{aligned} & D_{2h} : \Gamma[S(n\pi^*) \rightarrow T(\pi\pi^*)] \otimes \Gamma(q_{76}) \\ & = (B_{1u} \oplus B_{2u} \oplus B_{3u}) \otimes B_{2u} \\ & = B_{3g} \oplus A_g \oplus B_{1g} \end{aligned} \tag{4.9}$$

The symmetry analysis of spin–vibronic coupling can be approached from another perspective. The b_{2u} C-S stretching mode lowers the molecular symmetry to C_{2v}. The spatial symmetry of $\pi\pi^*$ and $n\pi^*$ now transforms as B_2 and B_1, respectively. Under the C_{2v} symmetry, the spin symmetry of singlets and triplets transform as A_1 and $A_2 \oplus B_1 \oplus B_2$, respectively.

At this lower symmetry, the direct product contains the totally symmetric irrep A_1, allowing for non-zero spin–orbit coupling. Notice that from this perspective, spin–vibronic contributions to spin–orbit coupling are included in the direct spin–orbit coupling at the distorted geometry.

$$\begin{aligned} &C_{2v} : \Gamma[S(n\pi^*) \rightarrow T(\pi\pi^*)] \\ &= B_1 \otimes A_1 \otimes A_1 \otimes B_2 \otimes (A_2 \oplus B_1 \oplus B_2) \\ &= A_1 \oplus B_2 \oplus B_1 \end{aligned} \tag{4.10}$$

To further understand the spin–vibronic mechanism, we dissect the spin–orbit integral into spin and spatial terms for further examination. Since both excited states are described mostly by a single orbital excitation, the spin–orbit coupling between the singlet and triplet states given by Equations (3.22) and (3.23) can be written as[52]

$$\langle S(n\pi^*)|\hat{H}_{SO}|T(\pi\pi^*), M_S = \pm 1\rangle = \frac{1}{2\sqrt{2}}(h^x_{\pi n} \pm i h^i_{\pi n}) \propto \langle \pi|\hat{l}_x \pm i\hat{l}_y|n\rangle \tag{4.11}$$

$$\langle S(n\pi^*)|\hat{H}_{SO}|T(\pi\pi^*), M_S = 0\rangle = \frac{1}{2}h^z_{\pi n} \propto \langle \pi|\hat{l}_z|n\rangle \tag{4.12}$$

The spin degrees of freedom are eliminated during the derivation of Equations (3.22) and (3.23), requiring only non-relativistic group theory. The fact that Equations (4.11) and (4.12) depends on spatial orbital symmetry and are not definitively equal to zero indicate that the spin–orbit coupling is not quenched by spin symmetry. Whether Equations (4.11) and (4.12) is non-zero is dictated by the following direct products:

$$\begin{aligned} &D_{2h} : \Gamma[\langle \pi|\hat{l}_x \pm i\hat{l}_y|n\rangle] \\ &= b_{1u} \otimes (b_{2g} \oplus b_{3g}) \otimes b_{1g} \\ &= b_{2u} \oplus b_{3u} \end{aligned} \tag{4.13}$$

$$\begin{aligned} &D_{2h} : \Gamma[\langle \pi | \hat{l}_z | n \rangle] \\ &= b_{1u} \otimes b_{1g} \otimes b_{1g} \\ &= b_{1u} \end{aligned} \tag{4.14}$$

This suggests that the symmetry quenching of direct spin–orbit coupling is solely due to spatial symmetry. Although the intersystem crossing is El-Sayed allowed, as the change in spin angular momentum is accompanied by an $n \rightarrow \pi$ orbital transition, the process remains forbidden because the orbital transition is symmetry forbidden via a spatial rotation due to rotational symmetry mismatch as well as parity conservation. To overcome these restraints, an *ungerade* rotation-odd distortion is required to enable this transition.

The above analysis suggests that any b_{1u}, b_{2u}, and b_{3u} distortion can potentially enhance spin–orbit coupling between $S(n\pi^*)$ and $T(\pi\pi^*)$. We turn to aniline thiosquarine (A-TSQ), an analog of DBA-TSQ where the butyl groups are replaced by hydrogens, as a simplified and more centrosymmetric model to investigate the effects of other normal modes. Spin–orbit coupling between $S(n\pi^*)$ and $T(\pi\pi^*)$ was calculated at $q_a = 0.2$ Åalong each normal mode independently. In Figure 4.14, the spin–orbit coupling was plotted against the squarine motif contribution to each normal mode. As predicted by group theory, the plot shows that only b_{1u}, b_{2u}, and b_{3u} normal modes are spin–vibronically active. Spin–vibronic activity of these modes increases with the amount of squarine contribution to the normal mode, eventually plateauing at large contributions. No correlation with sulfur, aniline, or hydrogen was observed. This shows that the spin–vibronic coupling is mainly driven by symmetry-perturbation of the squarine motif. Moreover, the b_{2u} mode, which corresponds to in-plane distortions along the y-axis, are the most spin–vibronically active.

Equation (4.7) shows that higher-order (the third term and beyond) spin–vibronic coupling can occur through coupling between different modes or along one mode. Whether symmetry allows for higher-order spin–vibronic coupling can be determined by including irreps of the modes involved in the direct product. Symmetry mandates that second-order spin–vibronic coupling only occurs via coupling between *gerade* and *ungerade* modes. For

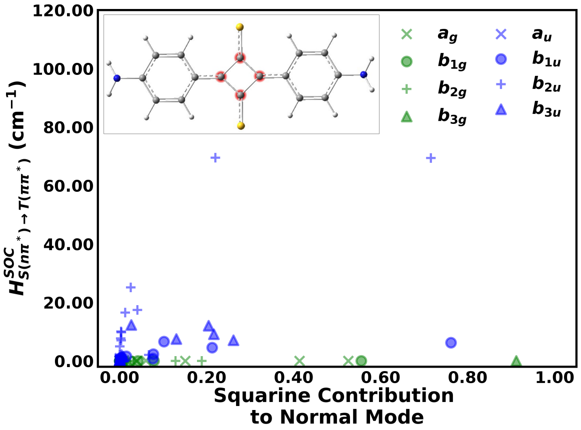

Figure 4.14: Plot of spin–orbit coupling between $S(n\pi^*) \rightarrow T(\pi\pi^*)$ vs. "squarine" motif (atoms highlighted in red) contribution to the normal mode, for each normal mode of A-TSQ. Each normal mode is marked based on their irrep. Green markers are *gerade* normal mode. Blue markers are *ungerade* normal modes.

example, second-order spin–vibronic coupling involving a b_{2u} mode and an a_g mode is allowed since A_g appears in the direct product of these irreps and the irreps in Equation (4.8). Additionally, third-order spin–vibronic coupling may occur along a single mode, however the modulus sigmoid shape of the spin–orbit coupling curve in Figure 4.12 suggests that it is a counteracting correction to first-order spin–vibronic coupling.

In contrast to the $S(n\pi^*) \rightarrow T(\pi\pi^*)$ pathway, which has El-Sayed-allowed but symmetry-forbidden direct spin–orbit coupling, the $S(n\pi^*) \rightarrow T(n\pi^*)$ pathway is both El-Sayed- and symmetry-forbidden, as shown in Equation (4.15). The symmetry-perturbation mechanism outlined above could also give rise to non-zero spin–orbit coupling through spin–vibronic interactions in this case.

$$
\begin{aligned}
&D_{2h} : \Gamma[S(n\pi^*) \rightarrow T(\pi\pi^*)] \\
&= B_{3g} \otimes A_g \otimes A_g \otimes B_{3u} \otimes (B_{1g} \oplus B_{2g} \oplus B_{3g}) \\
&= B_{1u} \oplus B_{2u} \oplus B_{3u}
\end{aligned}
\tag{4.15}
$$

Symmetry analysis within the local D_{2h} symmetry indicates that only the b_{1g}, b_{2g}, and b_{3g} vibrational modes are capable of lifting the relevant symmetry restrictions. However, computational results reveal that these modes are not spin–vibronically active; that is, spin–orbit coupling remains negligible along these vibrational modes. This is because, although the b_{1g}, b_{2g}, and b_{3g} modes can relax symmetry restrictions, they do not promote orbital mixing and therefore fail to satisfy the El-Sayed criterion. As a result, intersystem crossing is unlikely to occur via the $S(n\pi^*) \rightarrow T(n\pi^*)$ pathway.

4.2.5 Conclusion

As intersystem crossing (ISC) continues to drive advancements in photochemical innovations, there is increasing interest in enhancing, suppressing, or dynamically modulating ISC processes. Though DBA-TSQ $S(n\pi^*) \rightarrow T(\pi\pi^*)$ conserves total angular momentum and satisfies El-Sayed's rule, the transition is symmetry-forbidden at the $S(n\pi^*)$ equilibrium geometry. Despite these symmetry restrictions, it achieves picosecond ISC through spin–vibronic coupling facilitated by a symmetry-perturbing mechanism. This work highlights the importance of considering spin–vibronic-driven symmetry-perturbations alongside atomic number and electronic structure modulation when designing systems with a propensity for ISC. Symmetry arguments have been made to rationalize slow ISC rates in past work, but it is often overshadowed by El-Sayed's rule. Additionally, we would like to emphasize that symmetry restrictions can be somewhat exacerbated in centrosymmetric systems as the introduction of parity creates further restrictions. To further explore these findings, future work will focus on the synthesis and ISC measurements of asymmetric DBA-TSQ derivatives.

Our work alone suggests that El-Sayed's rule must be used in conjunction with symmetry selection rules to determine whether zeroth- SOC is non-zero and to identify spin–vibronically-active vibrational modes. More work is needed in investigating the converse where the transition is symmetry allowed but El-Sayed forbidden to fully understand the relationship between these two selection rules.

Bibliography

[1] Devadas, M. S.; Bairu, S.; Qian, H.; Sinn, E.; Jinn, R.; Ramakrishna, G. Temperature-Dependent Optical Absorption Properties of Monolayer-Protected Au_{25} and Au_{38} Clusters. *J. Phys. Chem. Lett.* **2011**, *2*, 2752–2758.

[2] Roos, B. O.; Lindh, R.; Malmqvist, P.-A.; Veryazov, V.; Widmark, P.-O. Main Group Atoms and Dimers Studied with a New Relativistic ANO Basis Set. *J. Phys. Chem. A* **2004**, *108*, 2851–2858.

[3] Pritchard, B. P.; Altarawy, D.; Didier, B.; Gibson, T. D.; Windus, T. L. New Basis Set Exchange: An Open, Up-to-Date Resource for the Molecular Sciences Community. *J. Chem. Inf. Model.* **2019**, *59*, 4814–4820.

[4] Szabo, A.; Ostlund, N. S. *Modern Quantum Chemistry: Introduction to Advanced Electronic Structure Theory*; Dover Publications, INC., 1996.

[5] Helgaker, T.; Jørgensen, P. *Molecular Electronic-Structure Theory*; John Wiley & Sons Ltd., 1996.

[6] Koch, W.; Holthausen, M. C. *A Chemist's Guide to Density Functional Theory*; Wiley-VCH, 2001.

[7] Shavitt, I.; Bartlett, R. J. *Many-Body Methods in Chemistry and Physics: MBPT and Coupled-Cluster Theory*; Cambrdige University Press, 2009.

[8] Olsen, J.; Roos, B. O.; Jørgensen, P.; Jensen, H. J. A. Determinant Based Configuration Interaction Algorithms for Complete and Restricted Configuration Interaction Spaces. *J. Chem. Phys.* **1988**, *89*, 2185–2192.

[9] Fleig, T.; Olsen, J.; Marian, C. M. The Generalized Active Space Concept for the Relativistic Treatment of Electron Correlation. I. Kramers-Restricted Two-Component Configuration Interaction. *J. Chem. Phys.* **2001**, *114*, 4775–4790.

[10] Hu, H.; Upadhyay, S.; Lu, L.; Jenkins, A. J.; Zhang, T.; Shayit, A.; Knecht, S.; Li, X. Small Tensor Product Distributed Active Space (STP-DAS) Framework for Relativistic and Non-Relativistic Multiconfiguration Calculations: Scaling from 10^9 on a Laptop to 10^{12} Determinants on a Supercomputer. *Comput. Phys. Rep.* **2024**, *5*, 041404.

[11] Roos, B. O.; Taylor, P. R.; Sigbahn, P. E. M. A Complete Active Space SCF Method (CASSCF) using a Density Matrix Formulated Super-CI Approach. *Chem. Phys.* **1980**, *48*, 157–173.

[12] Malmqvist, P.-Å.; Roos, B. O. The Restricted Active Space Self-Consistent-Field Method, Implemented with a Split Graph Unitary Group Approach. *J. Phys. Chem.* **1990**, *94*, 5477–5482.

[13] Stein, C. J.; Reiher, M. Automated Selection of Active Orbital Spaces. *J. Chem. Theory Comput.* **2016**, *12*, 1760–1771.

[14] Sayfutyarova, E. R.; Sun, Q.; Chan, G. K.-L.; Knizia, G. Automated Construction of Molecular Active Spaces from Atomic Valence Orbitals. *J. Chem. Theory Comput.* **2017**, *13*, 4063–4078.

[15] Jeong, W.; Stoneburner, S. J.; King, D.; Li, R.; Walker, A.; Lindh, R.; Gagliardi, L. Automation of Active Space Selection for Multireference Methods via Machine Learning on Chemical Bond Dissociation. *J. Chem. Theory Comput.* **2020**, *16*, 2389–2399.

[16] Kaufold, B. W.; Chintala, N.; Pandeya, P.; Dong, S. S. Automated Active Space Selectrion with Dipole Moments. *J. Chem. Theory Comput.* **2023**, *19*, 2469–2483.

[17] Marian, C. M.; Hell, A.; Kleinschmidt, M. The DFT/MRCI Method. *WIREs Comput. Mol. Sci.* **2019**, *9*, e1394.

[18] Casida, M. E. *Recent Advances in Density Functional Methods*; 1995; pp 155–192.

[19] Larsen, H.; Jørgensen, P.; Olsen, J.; Helgaker, T. Hartree-Fock and Kohn-Sham Atomic-Orbital Based Time-Dependent Response Theory. *J. Chem. Phys.* **2000**, *113*, 8908–8916.

[20] Coriani, S.; Høst, S.; Jansík, B.; Thøgersen, L.; Olsen, J.; Jørgensen, P.; Reine, S.; Pawłowski, F.; Helgaker, T.; Sałek, P. Linear-Scaling Implementation of Molecular Response Theory in Self-Consistent Field Electronic-Structure Theory. *J. Chem. Phys.* **2007**, *126*, 154108.

[21] Dreuw, A.; Head-Gordon, M. Single-Reference Ab Initio Methods for the Calculation of Excited States of Large Molecules. *Chem. Rev.* **2007**, *126*, 154108.

[22] Chantzis, A.; Laurent, A. D.; Adamo, C.; Jacquemin, D. Is the Tamm-Dancoff Approximation Reliable for the Calculation of Absorption and Fluorescence Band Shapes? *J. Chem. Theory Comput.* **2013**, *9*, 4517–4525.

[23] Fransson, T.; Pettersson, L. G. M. Evaluating the Impact of the Tamm-Dancoff Approximation on X-ray Spectrum Calculations. *J. Chem. Theory Comput.* **2024**, *20*, 2182–2191.

[24] Hirata, S.; Head-Gordon, M. Time-Dependent Density Functional Theory within the Tamm-Dancoff Approximation. *Chem. Phys. Lett.* **1999**, *314*, 219–299.

[25] González, L. *Quantum Chemistry and Dynamics of Excited States*; John Wiley & Sons Ltd., 2021.

[26] Norrby, L. J. Why is Mercury Liquid? Or, Why Do Relativistic Effects Not Get into Chemistry Textbooks? *J. Chem. Educ.* **1991**, *68*, 110–113.

[27] Pyykkö, P. Relativistic Effects in Structural Chemistry. *Chem. Rev.* **1988**, *88*, 563–594.

[28] Thayer, J. S. Relativistic Effects and the Chemistry of the Heaviest Main-Group Element. *J. Chem. Educ.* **2005**, *82*, 1721–1727.

[29] Pyykkö, P. Relativistic Effects in Chemistry: More Common Than You Think. *Annu. Rev. Phys. Chem.* **2012**, *63*, 45–64.

[30] Dyall, K. G.; Fægri, Jr., K. *Introduction to Relativistic Quantum Chemistry*; Oxford University Press, 2007.

[31] Reiher, M.; Wolf, A. *Relativistic Quantum Chemistry*, 2nd ed.; Wiley-VCH, 2015.

[32] Saue, T. Relativistic Hamiltonians for Chemistry: A Primer. *J. Chem. Phys.* **1994**, *100*, 2118–2127.

[33] Dyall, K. G. An Exact Separation of the Spin-Free and Spin-Dependent Terms of the Dirac–Coulomb–Breit Hamiltonian. *J. Chem. Phys.* **1994**, *100*, 2118–2127.

[34] Sun, S.; Stetina, T.; Zhang, T.; Hu, H.; Valeev, E.; Sun, Q.; Li, X. Efficient Four-Component Dirac-Coulomb-GauntHartree–Fock in Pauli Spinor Representation. *J. Chem. Theory Comput.* **2021**, *17*, 3388–3402.

[35] Sun, S.; Ehrman, J.; Zhang, T.; Sun, Q.; Dyall, K. G.; Li, X. Scalar Breit Interaction for Molecular Calculations. *J. Chem. Phys.* **2023**, *158*, 171101.

[36] Douglas, M.; Kroll, N. M. Quantum Electrodynamical Corrections to the Fine Structure of Helium. *Ann. Phys.* **1974**, *82*, 89–155.

[37] van Lenthe, E.; Baerends, E. J.; Snijders, J. G. Relativistic Regular Two-Component Hamiltonians. *J. Chem. Phys.* **1993**, *99*, 4597–4610.

[38] van Lenthe, E.; Baerends, E. J.; Snijders, J. G. Relativistic Total Energy Using Regular Approximations. *J. Chem. Phys.* **1994**, *101*, 9783–9792.

[39] Barysz, M.; Sadlej, A. J.; Snijders, J. G. Nonsingular Two/One-Component Relativistic Hamiltonians Accurate Through Arbitrary High Order in α^2. *Int. J. Quant. Chem.* **1997**, *65*, 225–239.

[40] Nakajima, T.; Hirao, K. The Higher-Order Douglas–Kroll Transformation. *J. Chem. Phys.* **2000**, *113*, 7786–7789.

[41] Barysz, M.; Sadlej, A. J. Two-Component Methods of Relativistic Quantum Chemistry: From the Douglas-Kroll Approximation to the Exact Two-Component Formalism. **2001**, *573*, 181–200.

[42] Barysz, M.; Sadlej, A. J. Infinite-Order Two-Component Theory for Relativistic Quantum Chemistry. *J. Chem. Phys.* **2002**, *116*, 2696–2704.

[43] Wolf, A.; Reiher, M.; Hess, B. A. The Generalized Douglas–Kroll Transformation. *J. Chem. Phys.* **2002**, *117*, 9215–9226.

[44] Reiher, M.; Wolf, A. Exact Decoupling of the DIrac Hamiltonian. II. The Generalized Douglas-Kroll-Hess Transformation Up to Arbitrary Order. *J. Chem. Phys.* **2004**, *121*, 10945.

[45] Kędziera, D.; Barysz, M. Non-Iterative Approach to the Infinite-Order Two-Component (IOTC) Relativistic Theory and the Non-Symmetric Algebraic Riccati Equation. *Chem. Phys. Lett.* **2007**, *446*, 176–181.

[46] Liu, W.; Peng, D. Exact Two-component Hamiltonians Revisited. *J. Chem. Phys.* **2009**, *131*, 031104.

[47] Peng, D.; Middendorf, N.; Weigend, F.; Reiher, M. An Efficient Implementation of Two-Component Relativistic Exact-Decoupling Methods for Large Molecules. *J. Chem. Phys.* **2013**, *138*, 184105.

[48] Marian, C. M. *Reviews in Computational Chemistry*; John Wiley & Sons, Ltd, 2001; Chapter 3, pp 99–204.

[49] Marian, C. M. Spin-Orbit Coupling and Intersystem Crossing in Molecules. *WIREs Comput. Mol. Sci.* **2012**, *2*, 187–203.

[50] Gao, X.; Bai, S.; Fazzi, D.; Niehaus, T.; Barbatti, M.; Thiel, W. Evaluation of Spin-Orbit Couplings with Linear-Response Time-Dependent Density Functional Methods. *J. Chem. Theory Comput.* **2017**, *13*, 515–524.

[51] Penfold, T. J.; Gindensperger, E.; Daniel, C.; Marian, C. M. Spin-Vibroinc Mechanism for Intersystem Crossing. *Chem. Rev.* **2018**, *118*, 6975–7025.

[52] Liao, C.; Kasper, J. M.; Jenkins, A. J.; Yang, P.; Batista, E. R.; Frisch, M. J.; Li, X. State Interaction Linear Response Time-Dependent Density Functional Theory with Perturbative Spin–Orbit Coupling: Benchmark and Perspectives. *JACS Au* **2023**, *3*, 358–367.

[53] Nakajima, T.; Hirao, K. The Douglas–Kroll–Hess Approach. *Chem. Rev.* **2012**, *112*, 385–402.

[54] Sjøvoll, M.; Fagerli, H.; Gropen, O.; Almöf, J.; Schimmelpfennig, B.; Wahlgren, U. An Efficient Treatment of Kinematic Factors in Pseudo-Relativistic Calculations of Electronic Structure. *Theor. Chem. Acc.* **1998**, *99*, 1–7.

[55] Boettger, J. C. Approximate Two-Electron Spin-Orbit Coupling Term For Density-Functional-Theory DFT Calculations Using The Douglas-Kroll-Hess Transformation. *Phys. Rev. B* **2000**, *62*, 7809–7815.

[56] Ehrman, J.; Martinez-Baez, E.; Jenkins, A. J.; Li, X. Improving One-Electron Exact-Two-Component Relativistic Methods with the Dirac–Coulomb–Breit-Parameterized Effective Spin–Orbit Coupling. *J. Chem. Theory Comput.* **2023**, *19*, 5785–5790.

[57] Kahn, L. R.; Baybutt, P.; Truhlar, D. G. Ab Initio Effective Core Potentials: Reduction of All-Electron Molecular Structure Calculations to Calculations Involving Only Valence Electrons. *J. Chem. Phys.* **1976**, *65*, 3826–3853.

[58] Ermler, W. C.; Lee, Y. S.; Christiansen, P. A.; Pitzer, K. S. Ab Initio Effective Core Potentials Including Relativistic Effects. A Procedure for the Inclusion of Spin–Orbit Coupling in Molecular Wavefunctions. *Chem. Phys. Lett.* **1981**, *81*, 70–74.

[59] Pitzer, R. M.; Winter, N. W. Electronic-Structure Methods for Heavy-Atom Molecules. *J. Phys. Chem.* **1988**, *92*, 3061–3063.

[60] Christiansen, P. A.; Pacios, L. F. Ab Initio Relativistic Effective Potentials with Spin–Orbit Operators. I. Li Through Ar. *J. Chem. Phys.* **1985**, *82*, 2664–2671.

[61] Andrae, D.; Häußermann, U.; Dolg, M.; Stoll, H.; Preuß, H. Energy-Adjusted Ab Initio Pseudopotentials for the Second and Third Row Transition Elements. *Theor. Chem. Acc.* **1990**, *77*, 123–141.

[62] Haris, K.; Kramida, A. Critically Evaluated Spectral Data for Neutral Carbon (C I). *Astrophys. J. Suppl. S.* **2017**, *233*.

[63] Kramida, A.; Ralchenko, Y.; Reader, J.; and NIST ASD Team NIST Atomic Spectra Database (ver. 5.12), [Online]. Available: `https://physics.nist.gov/asd` [2016, January 31]. National Institute of Standards and Technology, Gaithersburg, MD., 2024.

[64] Martin, W. C.; Zalubas, R.; Hagan, L. *National Standard Reference Data Series, NSRDS-NBS 60*; National Bureau of Standards: U.S., 1978.

[65] Harris, D. C.; Bertolucci, M. D. *Symmetry and Spectroscopy: An Introduction to Vibrarional and Electronic Spectroscopy*; Dover Publications, INC., 1989.

[66] Drago, R. S. *Physical Methods for Chemists*; Surfside Scientific Publishers, 1992.

[67] Rakowitz, F.; Marian, C. M. The Fine-Structure Splitting of the Thallium Atomic Ground State: LS- versus jj-Coupling. *Chem. Phys. Lett.* **1996**, *257*, 105–110.

[68] Cotton, F. A. *Chemical Applications of Group Theory*; John Wiley & Sons, 2003.

[69] Atkins, P.; Friedman, R. *Molecular Quantum Mechanics*; Oxford University Press, 2011.

[70] Jung, J.; Atanasov, M.; Neese, F. Ab Initio Ligand-Field Theory Analysis and Covalency Trends in Actinide and Lanthanide Free Ions and Octahedral Complexes. *Inorganic Chemistry* **2017**, *56*, 8802–8816.

[71] Altmann, S. L.; Herzig, P. *Point-Group Theory Tables*; Clarendon Press, 2011.

[72] Altmann, S. L. *Rotations, Quaternions, and Double Groups*; Dover Publications, INC., 2005.

[73] Zimmermann, P.; Hunault, M. O. J. Y.; de Groot, F. M. F. 1s2p RIXS Calculations for 3d Transition Metal Ions in Octahedral Symmetry. *J. Spectrosc.* **2018**, *2018*, 3618463.

[74] Malmqvist, P. A.; Roos, B. The CASSCF State Interaction Method. *Chem. Phys. Lett.* **1989**, *155*, 189–194.

[75] Egidi, F.; Goings, J. J.; Frisch, M. J.; Li, X. Direct Atomic-Orbital-Based Relativistic Two-Component Linear Response Method for Calculating Excited-State Fine Structures. *J. Chem. Theory Comput.* **2016**, *12*, 3711–3718.

[76] Jenkins, A. J.; Liu, H.; Kasper, J. M.; Frisch, M. J.; Li, X. Variational Relativistic Two-Component Complete-Active-Space Self-Consistent Field Method. *J. Chem. Theory Comput.* **2019**, *15*, 2976–2982.

[77] Asthana, A.; Liu, J.; Cheng, L. Exact Two-Component Equation-of-Motion Coupled-Cluster Singles and Doubles Method using Atomic Mean-Field Spin-Orbit Integrals. *J. Chem. Phys.* **2019**, *150*, 074102.

[78] Hu, H.; Jenkins, A. J.; Liu, H.; Kasper, J. M.; Frisch, M. J.; Li, X. Relativistic Two-Component Multireference Configuration Interaction Method with Tunable Correlation Space. *J. Chem. Theory Comput.* **2020**, *16*, 2975–2984.

[79] Liu, J.; Cheng, L. Relativistic Coupled-Cluster and Equation-of-Motion Coupled-Cluster Methods. *WIREs Comput. Mol. Sci.* **2021**, *11*, 1536.

[80] Lu, L.; Hu, H.; Jenkins, A. J.; Li, X. Exact-Two-Component Relativistic Multireference Second-Order Perturbation Theory. *J. Chem. Theory Comput.* **2022**, *18*, 2983–2992.

[81] Hoyer, C. E.; Lu, L.; Hu, H.; Shumilov, K. D.; Sun, S.; Knecht, S.; Li, X. Correlated Dirac–Coulomb–Breit Multiconfigurational Self-Consistent-Field Methods. *J. Chem. Phys.* **2023**, *158*, 044101.

[82] Zhang, T.; Banerjee, S.; Koulias, L. N.; Valeev, E. J.; DePrince, A. E. I.; Li, X. Dirac–Coulomb–Breit Molecular Mean-Field Exact-Two-Component Relativistic Equation-of-Motion Coupled-Cluster Theory. *J. Phys. Chem. A* **2024**, *128*, 3408–3418.

[83] Fieser, M. E. et al. Evaluating the Electronic Structure of Formal Ln^{II} Ions in $\mathrm{Ln}^{II}(\mathrm{C_5H_4SiMe_3})_3^{1-}$ using XANES Spectroscopy and DFT Calculations. *Chem. Sci.* **2017**, *58*, 6076–6091.

[84] Rice, N. T.; Su, J.; Gompa, T. P.; Russo, D. R.; Telser, J.; Palatinus, L.; Basca, J.; Yang, P.; Batista, E. R.; La Pierre, H. S. Homoleptic Imidophosphorane Stabilization of Tetravalent Cerium. *Inorg. Chem.* **2019**, *58*, 5289–5304.

[85] Kim, Y.; Ma, R.; Lee, J.; Harich, J.; Nam, D.; Kim, S.; Kim, M.; Ochmann, M.; Eom, I.; Huse, N.; Lee, J. H.; Kim, T. K. Ligand-Field Effects in a Ruthenium(II) Polypyridyl Complex Probed by Femtosecond X-ray Absorption Spectroscopy. *JPCL* **2021**, *12*, 12165–12172.

[86] Tateyama, H.; Boggiano, A. C.; Liao, C.; Otte, K. S.; Li, X.; La Pierre, H. S. Tetravalent Cerium Alkyl and Benzyl Complexes. *JACS* **2024**, *146*, 10268–10273.

[87] Malmqvist, P. A.; Roos, B.; Schimmelpfennig, B. The Restricted Active Space (RAS) State Interaction Approach with Spin–Orbit Coupling. *Chem. Phys. Lett.* **2002**, *357*, 230–240.

[88] Roos, B.; Malmqvist, P. A. Relativistic Quantum Chemistry: The Multiconfigurational Approach. *Phys. Chem. Chem. Phys.* **2004**, *6*, 2919–2927.

[89] Wang, F.; Ziegler, T. A Simplified Relativistic Time-Dependent Density-Functional Theory Formalism for the Calculations of Excitation Energies Including Spin-Orbit Coupling Effect. *J. Chem. Phys.* **2005**, *123*, 154102.

[90] Li, Z.; Suo, B.; Zhang, Y.; Xiao, Y.; Liu, W. Combining State-Adapted Open-Shell TD-DFT with Spin–Orbit Coupling. *Mol. Phys.* **2013**, *111*, 3741–3755.

[91] Wang, Z.; Wang, F. Spin–orbit Coupling and Electron Correlation at Various Coupled-cluster Levels for Closed-shell Diatomic Molecules. *Phys. Chem. Chem. Phys.* **2013**, *15*, 17922–17928.

[92] Sayfutyarova, E. R.; Chan, G. K.-L. A State Interaction Spin–Orbit Coupling Density Matrix Renormalization Group Method. *J. Chem. Phys.* **2016**, *144*, 234301.

[93] Zhou, Q.; Suo, B. New Implementation of Spin–Orbit Coupling Calculatioin on Multi-Configuration Electron Correlation Theory. *Int. J. Quant. Chem.* **2021**, *121*, e26772.

[94] Hoyer, C. E.; Liao, C.; Shumilov, K. D.; Zhang, T.; Li, X. State Interaction for Relativistic Four-Component Methods: Choose the Right Zeroth-Order Hamiltonian for Late-Row Elements. *J. Chem. Theory Comput.* **2024**, *20*, 7969–7978.

[95] Liao, C.; Hoyer, C. E.; Ghosh, R. B.; Jenkins, A. J.; Knecht, S.; Frisch, M. J.; Li, X. Comparison of Variational and Perturbative Spin–Orbit Coupling within Two-Component CASSCF. *J. Phys. Chem. A* **2024**, *128*, 2498–2506.

[96] Mooßen, O.; Dolg, M. Two Interpretations of the Cerocene Electronic Ground State. *Chemical Physics Letters* **2014**, *594*, 47–50.

[97] Mato, J.; Gordon, M. S. A General Spin-Complete Spin-Flip Configuration Interaction Method. *PCCP* **2018**, *20*, 2615–2626.

[98] Frisch, M. J. et al. *Gaussian Development Version*, Revision J.26+; Gaussian, Inc.: Wallingford, CT, 2023.

[99] Li Manni, G. et al. The OpenMolcas Web: A Community-Driven Approach to Advancing Computational Chemistry. *J. Chem. Theory Comput.* **2023**, *19*, 6933–6991.

[100] Heß, B. A.; Marian, C. M.; Wahlgren, U.; Gropen, O. A Mean-Field Spin–Orbit Method Applicable to Correlated Wavefunctions. *Chem. Phys. Lett.* **1986**, *251*, 356–371.

[101] Nicklass, A.; Peterson, K. A.; Berning, A.; Werner, H.-J.; Knowles, P. J. Convergence of Breit-Pauli Spin-Orbit Matrix Elements with Basis Set Size and Configuration Interaction Space: The Halogen Atoms F, Cl, Br. *J. Chem. Phys.* **2000**, *112*, 5624–5632.

[102] VanGundy, R. A.; Persinger, T. D.; Heaven, M. C. Low Energy States of NdO^+ Probed by Photoelectron Spectroscopy. *J. Chem. Phys.* **2019**, *150*, 114302.

[103] Liao, C.; Lambros, E.; Sun, Q.; Dyall, K. G.; Li, X. Exploring Locality in Molecular Dirac–Coulomb–Breit Calculations: A Perspective. *J. Chem. Theory Comput.* **2023**, *19*, 9009–9017.

[104] Egidi, F.; Sun, S.; Goings, J. J.; Scalmani, G.; Frisch, M. J.; Li, X. Two-Component Nonlinear Time-Dependent Spin Density Functional Theory for Excited State Calculations. *J. Chem. Theory Comput.* **2017**, *13*, 2591–2603.

[105] Wahlgren, U.; Sjøvoll, M.; Fagerli, H.; Gropen, O.; Schimmelpfennig, B. Ab initio Calculations of the $^2P_{1/2}$-$^2P_{3/2}$ Splitting in the Thallium Atom. *Theor. Chem. Acc.* **1997**, *97*, 324–330.

[106] Singh-Rachford, T. N.; Castellano, F. N. Photo Upconversion Based on Sensitized Triplet-Triplet Annihilation. *Coordin. Chem. Rev.* **2010**, *254*, 2560–2573.

[107] Kasper, J. M.; Stetina, T. F.; Jenkins, A. J.; Li, X. Ab Initio Methods for L-Edge X-Ray Absorption Spectroscopy. *Comput. Phys. Rep.* **2020**, *1*, 011304.

[108] Liao, C.; Zhu, M.; Jiang, D.-e.; Li, X. Manifestation of the Interplay Between Spin–Orbit and Jahn–Teller Effects in Au_{25} Superatom UV-Vis Fingerprint Spectra. *Chem. Sci.* **2023**, *14*, 4666–4671.

[109] Liu, Y.; Ončák, M.; Meyer, J.; Ard, S. G.; Shuman, N. S.; Viggiano, A. A.; Guo, H. Intersystem Crossing Control of the $Nb^+ + CO_2 \rightarrow NbO^+ + CO$ Reaction. *J. Phys. Chem. A* **2024**, *128*, 6943–6953.

[110] Aucar, I. A.; Gómez, S. S.; Giribet, C. G.; Ruiz de Azúa, M. C. Breit Interaction Effects in Relativistic Theory of the Nuclear Spin-Rotation Tensor. *JCP* **2013**, *139*, 094112.

[111] Gilka, N.; Taylor, P. R.; Marian, C. M. Electron Spin-Spin Coupling from Multireference Configuration Interaction Wave Functions. *JCP* **2008**, *129*, 044102.

[112] Sato, T. K. et al. Measurement of the First Ionization Potential of Lawrencium, Element 103. *Nature* **2015**, *520*, 209–211.

[113] Kang, X.; Chong, H.; Zhu, M. $Au_{25}(SR)_{18}$: The Captain of the Great Nanocluster Ship. *Nanoscale* **2018**, *10*, 10758–10834.

[114] Negishi, Y.; Nobusada, K.; Tsukuda, T. Glutathione-Protected Gold Clusters Revisited: Bridging the Gap between Gold(I)-Thiolate Complexes and Thiolate-Protected Gold Nanocrystals. *J. Am. Chem. Soc.* **2005**, *127*, 5261–5270.

[115] Heaven, M. W.; Dass, A.; White, P. S.; Holt, K. M.; Murray, R. W. Crystal Structure

of the Gold Nanoparticle $[N(C_8H_{17})_4][Au_{25}(SCH_2CH_2Ph)_{18}]$. *J. Am. Chem. Soc.* **2008**, *130*, 3754–3755.

[116] Akola, J.; Walter, M.; Whetten, R. L.; Häkkinen, H.; Grönbeck, H. On the Structure of Thiolate-Protected Au_25. *J. Am. Chem. Soc.* **2008**, *130*, 3756–3757.

[117] Zhu, M.; Aikens, C. M.; Hollander, F. J.; Schatz, G. C.; Jin, R. Correlating the Crystal Structure of A Thiol-Protected Au_{25} Cluster and Optical Properties. *J. Am. Chem. Soc.* **2008**, *130*, 5883–5885.

[118] Parker, J. F.; Fields-Zinna, C. A.; Murray, R. W. The Story of a Monodisperse Gold Nanoparticle: $Au_{25}L_{18}$. *Acc. Chem. Res.* **2010**, *43*, 1289–1296.

[119] Cao, Y.; Chen, T.; Yao, Q.; Xie, J. Diversification of Metallic Molecules through Derivatization Chemistry of Au_{25} Nanoclusters. *Acc. Chem. Res.* **2021**, *54*, 4142–4153.

[120] Jiang, D.-e.; Kühn, M.; Tang, Q.; Weigand, F. Superatomic Orbitals under Spin-Orbit Coupling. *J. Phys. Chem. Lett.* **2014**, *5*, 3286–3289.

[121] Gonzalez, J. C.; Muñoz Castro, A. Doping the Superatom with p-Elements: The Role of p-Block Endohedral Atoms in Bonding and Optical Properties of $E@Au_{24}(SR)$_18 (E = Si, Ge, Sn, and Pb) from Relativistic DFT Calculations. *J. Phys. Chem. C* **2016**, *120*, 27019–27026.

[122] Alkan, F.; Muñoz Castro, A.; Aikens, C. M. Relativistic DFT Investigation of Electronic Structure Effects Arising from Doping the Au_{25} Nanocluster with Transition Metals. *Nanoscale* **2017**, *9*, 15825–15834.

[123] Gam, F.; Paez-Hernandez, D.; Arratia-Perez, R.; Liu, C.; Kahlal, S.; Saillard, J.-Y.; Muñoz Castro, A. Coinage Metal Superatomic Cores: Insights into Their Intrinsic Stability and Optical Properties from Relativistic DFT Calculations. *Chem. Eur. J.* **2017**, *23*, 11330–11337.

[124] Negishi, Y.; Chaki, N. K.; Shichibu, Y.; Whetten, R. L.; Tsukuda, T. Origin of Magic Stability of Thiolated Gold Clusters: A Case Study on $Au_{25}(SC_6H_{13})_{18}$. *J. Am. Chem. Soc.* **2007**, *129*, 11322 – 11323.

[125] Zhu, M.; Eckenhoff, W. T.; Pintauer, T.; Jin, R. Conversion of Anionic $[Au_25(SCH_2CH_2Ph)_{18}]$-Cluster to Charge Neutral Cluster via Air Oxidation. *J. Phys. Chem. C* **2008**, *112*, 14221–14224.

[126] Antonello, S.; Perera, N. V.; Ruzzi, M.; Gascón, J. A.; Maran, F. Interplay of Charge State, Lability, and Magnetism in the Molecule-like $Au_{25}(SR)_{18}$ Cluster. *J. Am. Chem. Soc.* **2013**, *135*, 15585–15594.

[127] Tofanelli, M. A.; Salorinne, K.; Ni, T. W.; Malola, S.; Newell, B.; Phillips, B.; Häkkinen, H.; Ackerson, C. J. Jahn-Teller Effects in $Au_{25}(SR)_{18}$. *Chem. Sci.* **2016**, *7*, 1882–1890.

[128] Walter, M.; Akola, J.; Lopez-Acevedo, O.; Häkkinen, H. A Unified View of Ligand-Protected Hold Clusters as Superatom Complexes. *Proc. Natl. Acad. Sci. U.S.A.* **2008**, *105*, 9157–9162.

[129] Kim, M.; Tang, Q.; Kumar, A. V. N.; Kwak, K.; Choi, W.; Jiang, D.-e.; Lee, D. Dopant-Dependent Electronic Structures Observed for $M_2Au_{36}(SC_6H_{13})_{24}$ Clusters (M = Pt, Pd). *J. Phys. Chem. Lett.* **2018**, *9*, 982–989.

[130] Kwak, K.; Lee, D. Electrochemistry of Atomically Precise Metal Nanoclusters. *Acc. Chem. Res.* **2019**, *52*, 12–22.

[131] Wang, S.; Tang, L.; Cai, G.; Yin, Z.; Li, Y.; Xiong, L.; Kang, X.; Xuan, J.; Pei, Y.; Zhu, M. Ligand Modification of Au_{25} Nanoclusters for Near-Infrared Photocatalytic Oxidative Functionalization. *J. Am. Chem. Soc.* **2022**, *144*, 3787–3792.

[132] Aikens, C. M. Geometric and Electronic Structure of $Au_{25}(SPHX)_{18}^-$ (X = H, F, Cl, Br, CH_3, and OCH_3). *J. Phys. Chem. Lett.* **2010**, *1*, 2594 – 2599.

[133] De Nardi, M.; Antonello, S.; Jiang, D.-e.; Pan, F.; Rissanen, K.; Ruzzi, M.; Venzo, A.; Zoleo, A.; Maran, F. Gold Nanowired: A Linear $(Au_{25})_n$ Polymer from Au_{25} Molecular Clusters. *ACS Nano* **2014**, *8*, 8505 – 8512.

[134] Frisch, M. J. et al. Gaussian Development Version Revision I.11+.

[135] Ernzerhof, M.; Scuseria, G. E. Assessment of the Perdew-Burke-Ernzerhof exchange-correlation functional. *J. Chem. Phys.* **1999**, *110*, 5029–5036.

[136] Adamo, C.; Barone, V. Toward reliable density functional methods without adjustable parameters: The PBE0 model. *J. Chem. Phys.* **1999**, *110*, 6158–6169.

[137] Pacios, L. F.; Christiansen, P. A. Ab Initio Relativistic Effective Potentials with Spin-orbit Operators. I. Li through Ar. *J. Chem. Phys.* **1984**, *82*, 2664–2671.

[138] Ross, R. B.; Powers, J. M.; Atashroo, T.; Ermler, W. C.; LaJohn, L. A.; Christiansen, P. A. Ab Initio Relativistic Effective Potentials with Spin-orbit Operators. IV. Cs through Rn. *J. Chem. Phys.* **1990**, *93*, 6654–6670.

[139] Feller, D. The Role of Databases in Support of Computational Chemistry Calculations. *J. Comput. Chem.* **1996**, *17*, 1571–1586.

[140] Schuchardt, K. L.; Didier, B. T.; Elsethagen, T.; Sun, L.; Gurumoorthi, V.; Chase, J.; Li, J.; Windus, T. L. Basis Set Exchange: A Community Database for Computational Sciences. *J. Chem. Inf. Model.* **2007**, *47*, 1045–1052.

[141] Kwak, K.; Tang, Q.; Kim, M.; Jiang, D.-e.; Lee, D. Interconversion between Superatomic 6-Electron and 8-Electron Configurations of $M@Au_{24}(SR)_{18}$ Clusters (M = Pd, Pt). *J. Am. Chem. Soc.* **2015**, *137*, 10833–10840.

[142] Ekardt, W. Work Function of Small Metal Particles: Self-Consistent Spherical Jellium-Background Model. *Phys. Rev. B* **1984**, *29*, 1558.

[143] Knight, W. D.; Clemenger, K.; de Heer, W. A.; Saunders, W. A.; Chou, M. Y.; Cohen, M. L. Electronic Shell Structure and Abundances of Sodium Clusters. *Phys. Rev. Lett.* **1984**, *52*, 2141–2143.

[144] de Heer, W. A. The Physics of Simple Metal Clusters: Experimental Aspects and Simple Models. *Rev. Mod. Phys.* **1993**, *65*, 611–676.

[145] Griffiths, D. J. *Introduction to Quantum Mechanics*; Prentice Hall, Inc., 1995.

[146] Cheng, L.; Yang, J. Communication: New Insight into Electronic Shells of Metal Clusters: Analogues of Simple Molecules. *Rev. Mod. Phys.* **2013**, *138*, 141101.

[147] Senanayake, R. D.; Akimov, A. V.; Aikens, C. M. Theoretical Investigation of Electron and Nuclear Dynamics in the $[\mathrm{Au}_25(\mathrm{SH})_{18}]^{-1}$ Thiolate-Protected Gold Nanocluster. *J. Phys. Chem. C* **2016**, *121*, 10653–10662.

[148] Liu, Y.; Ončák, M.; Meyer, J.; Ard, S. G.; Shuman, N. S.; Viggiano, A. A.; Guo, H. Multistate Dynamics and Kinetics of CO_2 Activation by Ta^+ in the Gas Phase: Insights into Single-Atom Catalysis. *J. Am. Chem. Soc.* **2024**, *146*, 14182–14193.

[149] Huber, M. E.; Lewis, T. W. R.; Meta, M.; Ard, S. G.; Liu, Y.; Sweeny, B. C.; Guo, H.; Ončák, M.; Shuman, N. S.; Meyer, J. Ta+ and Nb+ + CO_2: Intersystem Crossing in Ion–Molecule Reactions. *Phys. Chem. Chem. Phys.* **2024**, *26*, 8670–8680.

[150] Tang, D.; Liao, C.; Taub, M.; Schatz, G. C.; Guo, H.; Li, X. Photochemical Au(I)-Au(I) Bond Formation: A Battle Between Intersystem Crossing and Internal Conversion. *J. Phys. Chem. Lett.* **2025**, *16*, 3816–3821.

[151] Hauser, A. Intersystem crossing in the $[\mathrm{Fe(ptz)}_6](\mathrm{BF}_4)_2$ spin crossover system (ptz=1-propyltetrazole). *J. Chem. Phys.* **1991**, *94*, 2741–2748.

[152] Anslyn, E. V.; Dougherty, D. A. *Modern Physical Organic Chemistry*; University Science Books, 2006.

[153] van der Veen, R. M.; Cannizzo, A.; van Mourik, F.; Vlček, A. J.; Chergui, M. Vibrational Relaxation and Intersystem Crossing of Binuclear Metal Complexes in Solution. *JACS* **2011**, *133*, 305–315.

[154] Auböck, G.; Chergui, M. Sub-50-fs photoinduced spin crossover in $[\mathrm{Fe(bpy)_3}]^{2+}$. *Nat. Chem.* **2015**, *7*, 629–633.

[155] Zhang, K.; Ash, R.; Girolami, G. S.; Vura-Weis, J. Tracking the Metal-Centered Triplet in Photoinduced Spin Crossover of $\mathrm{Fe(phen)_3^{2+}}$ with Tabletop Femtosecond M-Edge X-ray Absorption Near-Edge Structure Spectroscopy. *J. Am. Chem. Soc.* **2019**, *141*, 17180–17188.

[156] Singh-Rachford, T. N.; Castellano, F. N. Low Power Visible-to-UV Upconversion. *J. Phys. Chem. A* **2009**, *113*, 5912–5917.

[157] Wu, W.; Guo, H.; Wu, W.; Ji, S.; Zhao, J. Organic Triplet Sensitizer Library Derived from a Single Chromophore (BODIPY) with Long-Lived Triplet Excited State for Triplet–Triplet Annihilation Based Upconversion. *J. Org. Chem.* **2011**, *76*, 7056–7064.

[158] Schulze, T. F.; Czolk, J.; Cheng, Y.-Y.; Fückel, B.; MacQueen, R. W.; Khoury, T.; Crossley, M. J.; Stannowski, B.; Lips, K.; Lemmer, U.; Colsmann, A.; Schmidt, T. W. Efficiency Enhancement of Organic and Thin-Film Silicon Solar Cells with Photochemical Upconversion. *J. Phys. Chem. C* **2012**, *116*, 22794–22801.

[159] Cheng, Y.-Y.; Nattestad, A.; Schulze, T. F.; MacQueen, R. W.; Fückel, B.; Lips, K.; Wallace, G. G.; Khoury, T.; Crossley, M. J.; Schmidt, T. J. Increased Upconversion Performance for Thin Film Solar Cells: A Trimolecular Composition. *Chem. Sci.* **2016**, *7*, 559–568.

[160] Frazer, L.; Gallaher, J. K.; Schmidt, T. W. Optimizing the Efficiency of Solar Photon Upconversion. *ACS Energy Lett.* **2017**, *2*, 1346–1354.

[161] Pristash, S. R.; Corp, K. L.; Rabe, E. J.; Schlenker, C. W. Heavy-Atom-Free Red-to-Yellow Photon Upconversion in a Thiosquaraine Composite. *ACS Appl. Energy Mater.* **2020**, *3*, 19–28.

[162] Gao, C.; Wong, W. H., Wallace; Qin, Z.; Lo, S.-C.; Namdas, E. B.; Dong, H.; Hu, W. Application of Triplet–Triplet Annihilation Upconversion in Organic Optoelectronic Devices: Advances and Perspectives. *Adv. Mater.* **2021**, *33*, 2100704.

[163] Zeng, L.; Huang, L.; Han, J.; Han, G. Enhanced Triplet-Triplet Annihilation Upconversion: From Molecular Design to Present Applications. *Acc. Chem. Res.* **2022**, *55*, 2604–2615.

[164] Shockley, W.; Queisser, H. J. Detailed Balance Limit of Efficiency of p-n Junction Solar Cells. *J. Appl. Phys.* **1961**, *32*, 510–519.

[165] Cheng, Y.; Ding, L. Perovskite/Si Tandem Solar Cells: Fundamentals, Advances, Challenges, and Novel Applications. *SusMat* **2021**, *1*, 324–344.

[166] Keivanidis, P. E.; Baluschev, S.; Miteva, T.; Nelles, G.; Scherf, U.; Yasuda, A.; Wegner, G. Up-Conversion Photoluminescence in Polyfluorene Doped with Metal(II)-Octaethyl Porphyrins. *Adv. Mater.* **2003**, *15*, 2095–2098.

[167] Singh-Rachford, T. N.; Castellano, F. N. Pd(II) Phthalocyanine-Sensitized Triplet-Triplet Annihilation from Rubrene. *J. Phys. Chem. A* **2008**, *112*, 3550–3556.

[168] Cui, X.; Zhao, J.; Yang, P.; Sun, J. Zinc(II) Tetraphenyltetrabenzoporphyrin Complex as Triplet Photosensitizer for Triplet–Triplet Annihilation Upconversion. *Chem. Commun.* **2013**, *49*, 10221–10223.

[169] Duan, P.; Yanai, N.; Kimizuka, N. A Bis-Cyclometalated Iridium Complex as a Benchmark Sensitizer for Efficient Visible-to-UV Photon Upconversion. *Chem. Commun.* **2014**, *50*, 13111–13113.

[170] Loudon, M.; Parise, J. *Organic Chemistry*; Roberts & Company Publishers, 2015.

[171] Peceli, D.; Hu, H.; Fishman, D. A.; Webster, S.; Przhonska, O. V.; Kurdyukov, V. V.; Slominsky, Y. L.; Tolmachev, A. I.; Kachkovski, A. D.; Gerasov, A. O.; Masunov, A. E.; Hagan, D. J.; van Stryland, E. W. Enhanced Intersystem Crossing Rate in Polymethine-Like Molecules: Sulfur-Containing Squaraines versus Oxygen-Containing Analogues. *J. Phys. Chem. A* **2013**, *117*, 2333–2346.

[172] Tilley, A. J.; Pensack, R. D.; Lee, T. S.; Djukic, B.; Scholes, G. D.; Seferos, D. S. Ultrafast Triplet Formation in Thionated Perylene Diimides. *J. Phys. Chem. C* **2014**, *118*, 9996–10004.

[173] Ortiz-Rodríguez, L. A.; Hoehn, S. J.; Acquah, C.; Abbass, N.; Waidmann, L.; Crespo-Hernández, C. E. Femtosecond Intersystem Crossing to the Reactive Triplet State of the 2,6-dithiopurine Skin Cancer Photosensitizer. *Phys. Chem. Chem. Phys.* **2021**, *23*, 25048.

[174] Cui, G.; Fang, W.-h. State Specific Heavy-Atom Effect on Intersystem Crossing Processes in 2-Thiothymine: A potential photodynamic Therapy Photosensitizer. *J. Chem. Phys.* **2013**, *138*, 044315.

[175] Pollum, M.; Jockusch, S.; Crespo-Hernández, C. E. 2,4-Dithiothymine as a Potent UVA Chemotherapeutic Agent. *J. Am. Chem. Soc.* **2014**, *136*, 17930–17933.

[176] Bai, S.; Barbatti, M. Why Replacing Different Oxygens of Thymine with Sulfur Causes Distinct Absorption and Intersystem Crossing. *J. Phys. Chem. A* **2016**, *120*, 6342–6350.

[177] Mai, S.; Pollum, M.; Martínez-Fernández, L.; Dunn, N.; Marquetand, P.; Corral, I.; Crespo-Hernández, C. E.; González, L. The Origin of Efficient Triplet State Population in Sulfur-Substituted Nucleobases. *Nat. Commun.* **2016**, *7*, 13077.

[178] Valentine, A. J. S.; Li, X. Intersystem Crossing in Late-Row Elements: A Perspective. *J. Phys. Chem. Lett.* **2022**, *13*, 3039–3046.

[179] El-Sayed, M. A. Spin–Orbit Coupling and the Radiationless Processes in Nitrogen Heterocyclics. *J. Chem. Phys.* **1963**, *38*, 2834–2838.

[180] Turro, N. J.; Ramamurthy, V.; Scaiano, J. C. *Principles of Molecular Photochemistry: An Introduction*; University Science Books, 2009.

[181] Baba, M. Intersystem Crossing in the $^1n\pi$ and $^3\pi\pi^*$ States. *JPCA* **2011**, *115*, 9514–9519.

[182] Pokhilko, P.; Krylov, A. I. Quantitative El-Sayed Rules for Many-Body Wave Functions from Spinless Transition Density Matrices. *J. Phys. Chem. Lett.* **2010**, *10*, 4857–4862.

[183] Perun, S.; Tatchen, J.; Marian, C. M. Singlet and Triplet Excited States and Intersystem Crossing in Free-Base Porphyrin: TDDFT and DFT/MRCI Study. *ChemPhysChem* **2008**, *9*, 282–292.

[184] Tatchen, J.; Gilka, N.; Marian, C. M. Intersystem Crossing Driven by Vibronic Spin–Orbit Coupling: A Case Study on Psoralen. *PCCP* **2007**, *9*, 5209–5221.

[185] Frisch, M. J. et al. Gaussian Development Version Revision J.14+.

[186] Tao, J.; Perdew, J. P.; Staroverov, V. N.; Scuseria, G. E. Climbing the Density Functional Ladder: Nonempirical Meta–Generalized Gradient Approximation Designed for Molecules and Solids. *Phys. Rev. Lett.* **2003**, *91*, 146401.

[187] Staroverov, V. N.; Scuseria, G. E.; Tao, J.; Perdew, J. P. Comparative Assessment of a New Nonempirical Density Functional: Molecules and Hydrogen-Bonded Complexes. *J. Chem. Phys.* **2003**, *119*, 12129–12137.

[188] Krishnan, R.; Binkley, J. S.; Seeger, R.; Pople, J. A. Self-Consistent Molecular Orbital Methods. XX. A Basis Set for Correlated Wave Functions. *J. Chem. Phys.* **1980**, *72*, 650–654.

[189] McLean, A. D.; Chandler, G. S. Contracted Gaussian Basis Sets for Molecular Calculations. I. Second Row Atom, Z=11-18. *J. Chem. Phys.* **1980**, *72*, 5639–5648.

[190] Francl, M. M.; Pietro, W. J.; Hehre, W. J.; Binkley, J. S.; Gordon, M. S.; DeFrees, D. J.; Pople, J. A. Self-Consistent Molecular Orbital Methods. XXIII. A Polarization-Type Basis Set for Second-Row Elements. *J. Chem. Phys.* **1982**, *77*, 3654–3665.

[191] Clark, T.; Chandrasekhar, J.; Spitznagel, G. W.; Schleyer, P. V. R. Efficient Diffuse Function-Augmented Basis Sets for Anion Calculations. III. The 3-21+G Basis Set for First-Row Elements, Li-F. *J. Comput. Chem.* **1983**, *4*, 294–301.

[192] Spitznagel, G. W.; Clark, T.; Schleyer, P. v. R.; Hehre, W. J. An Evaluation of the Performance of Diffuse Function-Augmented Basis Sets for Second Row Elements, Na-Cl. *J. Comput. Chem.* **1988**, *8*, 1109–1116.

[193] Austin, A.; Petersson, G. A.; Frisch, M. J.; Dobek, F. J.; Scalmani, G.; Throssell, K. A Density Functional with Spherical Atom Dispersion Terms. *J. Chem. Theory Comput.* **2012**, *8*, 4989–5007.

[194] Scalmani, G.; Frisch, M. J. Continuous Surface Charge Polarizable Continuum Models of Solvation. I. General Formalism. *J. Chem. Phys.* **2010**, *132*, 114110.

[195] Doleẑel, J.; Poryvai, A.; Slanina, T.; Filgas, J.; Slavíĉek, P. Spin-Vibronic Coupling Controls the Intersystem Crossing of Iodine-Substituted BODIPY Triplet Chromophones. *Chem. Eur. J.* **2024**, *30*, e202303154.

[196] Wang, K.; Zeng, T. Hamiltonian Formalism of Spin–Orbit Jahn–Teller and Pseudo-Jahn–Teller Problems in Trigonal and Tetragonal Symmetries. *Phys. Chem. Chem. Phys.* **2019**, *21*, 18939–18957.